Optical Property Trends in Metal/Polymer (Ag/PVDF) Nanocomposites:
A Computational Study

by

Christopher Kenneth Rowan
B.Sc., University of Bristish Columbia, 2007

A Thesis Submitted in Partial Fulfillment of the
Requirements for the Degree of

MASTER OF SCIENCE

in the Department of Chemistry

Optical Property Trends in Metal/Polymer (Ag/PVDF) Nanocomposites:
A Computational Study

by

Christopher Kenneth Rowan
B.Sc., University of Bristish Columbia, 2007

Supervisory Committee

Dr. Irina Paci, Supervisor
(Department of Chemistry)

Dr. David Steuerman, Departmental Member
(Department of Chemistry)

Supervisory Committee

Dr. Irina Paci, Supervisor
Department of Chemistry

Dr. David Steuerman, Departmental Member
Department of Chemistry

ABSTRACT

Metal-polymer nanocomposite materials were found to have highly tunable optical properties. Density functional theory-based calculations were employed to study trends in Ag/polyvinylidene fluoride nanocomposite optical properties. The frequency-dependent imaginary part of the dielectric constant was calculated from dipolar interband transitions. The metallic inclusion introduced both occupied and unoccupied states into the large polymer band gap. Thus, higher inclusion volume fractions generally led to stronger composite optical response. Spectra from monodisperse systems correlated well with nanoparticle quantum confinement models. A polydisperse system exhibited optical properties that correlated best with interparticle distances along the field direction. Nanodisk and nanorod-shaped inclusions had tunable response from field polarization, aspect ratio, crystallographic projections, and nanorod end-cap morphology.

Contents

List of Tables

List of Figures

ACKNOWLEDGEMENTS

I would like to thank Dr. Irina Paci, my supervisor, for her mentoring, support, encouragement, and patience; the University of Victoria for financial funding and their facilities; assistance from the Dr. E. and Mrs. M. Von Rudloff award; the Western Canada Research Grid for generous access to their high performance computers; as well as Bill W. and his friends.

- Let's go.
- We can't.
- Why not?
- We're waiting for Godot.
- Ah!
- S. Beckett

Chapter 1

Introduction

1.1 Goals

This thesis studies metal/polymer (Ag/PVDF) nanocomposite (NC) materials, with the aim of understanding trends in optical spectra. The large system sizes of NCs and their complex quantum interactions has prevented the development of a simple theoretical model. Here, density functional theory is applied to calculate optical properties of model NC systems from interband transitions. This approach provides a theoretical limit to the curent capabilities of simple quantum methods to calculate optical response. Modeling larger systems will need to break away from strictly quantum approaches, although with a corresponding loss of accuracy.

1.2 Metal/Polymer Nanocomposite Materials

Modern enthusiasm surrounding NCs and their multifunctional applications is a result of the unusual and intriguing material properties that are not easily predicted from the individual components. Nanoparticle (NP) inclusions are incorporated in only a few percent by volume in a host matrix, resulting in enhanced chemical properties (e.g. flammability [1]) or physical properties (e.g. acoustic, [2] mechanical, [3] electrical, [4] thermal, [5] magnetic [6] and optical [7]). Nanocomposite applications are thus widespread across many fields, such as: bio-medical, [8] bio-engineering, [9] dentistry, [10] aerospace, [11] automotive, [12] electronics [13] and optics. [14]

Nanosized particles are drastically different from the bulk material, due to quantum size effects. NPs may contain from tens to thousands of atoms, and their small dimensions imply a large surface area to volume ratio. The large number of surface atoms relative to bulk atoms implies increased surface energy, which is influential

in forming interfacial zones that are not yet well-understood. [15–17] Often, surfactant layers are added to NPs to increase their affinity for the matrix and reduce NP agglomeration. [18]

Nanocomposite applications require specific electric field response properties. Polymer-based NCs provide a medium which is highly versatile and easily processed. [19] These systems form class I, blended or inter-granular NCs, where constituents interact weakly with each other through non-covalent interactions, with no interpenetration of one constituent into the other. A wide range of NPs have been investigated, including: metals (e.g. Ni, [20] Au, [21] Ag [22] and Pd [23]); ceramics (e.g. $BaTiO_3$ [24]); clays (e.g. montmorillonite [25] and sepiolite [26]); elemental iodine [27]; carbon nanotubes [28] and various oxides (e.g. Nb_2O_5, [29] Al_2O_3, [30] SiO_2, [31] TiO_2, [32] MgO [33] and ZnO [34]).

The use of electrically insulating NCs has motivated applications for capacitors or dielectrics. [35–39] Capacitors generally use low frequency electric fields: 1Hz–1GHz, or static (zero frequency) fields. In this low frequency range, interfacial polarization dominates, where ions accumulate in trapping sites.

Where low-frequency material response is not well described with quantum theory, optical response properties are largely determined by electronic excitations and the band structure of the material, making this range of electrical response computationally accessible. The visible spectrum, as well as near-IR and near-UV, have frequencies in the THz–PHz regime, and is more often discussed in terms of wavelength or photon energy (0–5 eV). Further discussion will be limited to energy. In this spectral region, the energy of the incident field is sufficient to excite electrons into higher energy states, so that electronic excitations are the primary means of polarization. Applications for polymeric NCs containing metals (metallodielectrics, or metal-polymer NCs) abound, including: analytical sensors, [40] sensors for volatile organic compounds, [41] thermochromic sensors, [42] high refractive index materials, [43] photovoltaic cells (solar cells), [44] photo-luminescence, [45] field effect transistors, [46] bandpass filters, [47] nanophotonics, [48] waveguides, [49] antennas [50,51] and (anti-)reflective coatings. [52]

Metal-polymer (NCs) can strongly absorb electromagnetic radiation in the optical frequency range when the energy of the incident field induces electronic excitations. [53] The visible absorption spectra of polymers can be enhanced by many orders of magnitude through the incorporation of noble metal nanoparticles. [54] The enhanced signal is due to NP electrons that collectively oscillate, known as localized surface plasmon resonances (LSPR). [55] This effect is due to the wavelength of light being

much longer than the dimension of the NP (< 40 nm), known as the quasi-static limit, such that the NP uniformly experiences the field, with alternations in phase. [56]

The electronic structure of bulk material consists of a large number of degenerate molecular orbitals that form continuous bands of energy, in contrast to NPs where energy states are discrete. This implies that a bulk metal conductor (e.g. silver) can be an insulator at the nanoscale. [57] When metal NPs are dispersed in an insulating medium, electrons are confined to length scales that are shorter than the bulk mean free path of electrons, resulting in quantum confinement. [54] Small, spherical particles (quantum dots) have electrons confined in all three dimensions; rod-shaped particles (quantum wires) have electrons confined in two dimensions; and planar structures (quantum wells) have electrons confined in one dimension. The constrained electrons cause energy-level spacings to spread out. Energy spacings increase with decreasing length, as in the particle-in-a-box model.

Silver (Ag) NPs have electronic resonances in the visible range, and a variety of shapes and sizes have been fabricated to tune the absorption band. Geometries have included: spheres, [58] polyhedrals, [59] cubes, [60] hexapods, [61] prisms, [62] disks, [63] sheets, [64] rods [63] and wires. [65] Particle size distribution can be narrowed to produce near monodisperse systems through bottom-up reaction-driven approaches, [66, 67] or top-down lithographic methods. [68, 69] Monodispersity is important to produce specific absorption behaviour. Dispersion of NPs in a polymer matrix is often limited to random distributions, except in 2-D lithographic arrays, but new approaches are being developed. [70, 71]

Absorption of light by non-spherical NPs is dependent on the polarization of the incident field and orientation of the NP. Metal NPs distributed in an electrically insulating matrix experience quantum confinement, and electronic absorptions occur at lower energies when polarized fields induce electronic resonances along longer NP axes. [72] When a majority of NPs are oriented in the same direction, the material response depends on the field polarization, resulting in dichroic or birefringent materials. [73, 74] For example, it has been shown that the colour of drawn Ag rods in polyethylene is dependent on the polarization of incident light. [53, 75] The ability to control the orientation and alignment of NPs in a NC could see potential applications in sensors, [76] broadband waveguide polarizers, [77] optical antennas [50] and optical fibers that employ surface enhanced raman spectroscopy. [78,79] Aligned and oriented Ag/polymer NCs have recently been reported with nanorods [80] and wires. [71, 80]

We are further motivated by the essential role that large interfacial areas play in establishing NC properties. The interface is governed, in part, by interactions between

the NP and the polymer. The NP surface can adopt different crystallographic projections which vary in surface energy and atomic density, thereby changing physisorption sites. Ag and other face-centered-cubic crystals adopt primarily {111} facets, as these are the most energetically stable, followed by {100} and {110} facets. [81,82] Experiments have shown that Ag nanodisks often have {111} basal planes, [83–87] and have tunable optical properties. [88, 89] Nanorods and wires frequently have pentagonal cross sections, with sides consisting of 5 {100} planes connected with straight edges, and pentagonal pyramidal end-caps each with five {111} interfacing planes. [90–98] Experimental optical properties of these structures have been well-studied experimentally [65, 79, 99–105] and theoretically. [106–108]

Fine tuning of NC material properties towards specific applications could be achieved by adjusting numerous parameters. In addition to the type of polymer and NP, modifications can be made to: NP size, shape (anisotropy), dispersity, interparticle spacing, particle size distribution and volume fraction (loading). Moreover, oriented and aligned non-spherical NPs have directional-dependent excitations that can be selectively induced from polarized electric fields. Engineering materials for multifunctional applications therefore requires insight into the interplay between these parameters.

1.3 Modeling Electronic Response Properties

Prediction of frequency-dependent polarization, complex dielectric constant (ϵ_2) and other optical properties of materials has proven difficult due to the large number of atoms and the presence of nanoparticles where quantum effects dominate. Accurate modeling of these properties require a description of excited states. Many theories have described the frequency dependent dielectric constant, but none have predictive power in modeling nanocomposites.

For mixtures of compounds, effective medium approximations (EMAs) have been developed. If the system is homogeneous with a low filling fraction of randomly or well-dispersed components in a host, the effective dielectric constant of the mixture (ϵ_{eff}) can be considered as a function of ϵ of the individual constituents and their respective volume fractions. There is assumed to be no interaction between particles and therefore no interfacial effects. Briefly, the Clausius-Mossotti equation [109, 110] relates ϵ_{eff} to the dielectric constant of the host or environment (ϵ_e) and the atomic polarizability of spherical atomic inclusions. The Lorentz-Lorenz equation [111–113] is a variant, giving the effective index of refraction. Replacing the atomic polarizability

with the dielectric constant of the inclusion has seen numerous models, including: Maxwell-Garnett theory, [114] Bruggeman's symmetric mixing model, [115] Power Laws [116,117] and Lichtenecker's Logarithmic Law. [118] While experimental results can sometimes be fit to an EMA, it is often difficult to predict beforehand which model is appropriate, and the parameters are usually non-transferable. [119] The interested reader is referred to Ref. [120,121].

The polarizability (microscopic response) and polarization (macroscopic response) can be calculated from changes in the dipole moment of finite systems of atoms and molecules from theoretically applied zero frequency (static) fields. When periodic boundary conditions (PBC) are used to model infinitely extended systems, the cell is replicated in one or more dimensions, and the dipole moment is ill-defined. Charge is no longer able to accumulate at atomic or molecular boundaries, and a suitable representative volume element cannot be defined. The geometric Berry phase is one suitable circumvention, that calculates the change in polarization from electric field perturbations. This approach is based on phase changes from cyclic processes, and requires the system to be an insulator with an even number of electrons. [122,123]

When the electric field frequency is such that the material response is dominated by electronic excitations, ϵ_2 can be calculated from direct, dipolar interband transitions. [124–126] The Kramers-Kronig relations can then be used to calculate the real part of the dielectric constant (ϵ_1), and it is straightforward to calculate the conductivity (σ), complex index of refraction ($n = n_1 - in_2$), reflectance at normal incidence (R) and absorption coefficient (α).

This optical method makes a number of approximations. Foremost is the absence of local field effects, in which the external field is assumed equal to the microscopic field acting on individual electrons. Indirect transitions, which occur when the electron wave vector changes through coupling with a phonon, are ignored. Experimentally, they occur much less frequently than direct transitions. The calculated absorption spectra only includes single-particle excitations, and does not model collective oscillations. Variations in the effective mass of electrons (self-energy) and electron-hole interactions are also neglected.

An approach based on quantum mechanics is required to accurately model excited electronic states. For systems containing a thousand atoms or more, density functional theory (DFT) is a good option. It has been reasonably successful at simulating optical properties of atomic and molecular clusters, [127] periodic nanostructures [128,129] and crystalline compounds, [130] despite its well-known tendency to underestimate band gaps. [131,132] Results are also dependent on the choice of func-

tional, which is known to affect the magnitude and position of absorption peaks. [133] Nevertheless, more reliable methods are computationally intractable.

In the pages that follow, the sensitivity of the linear optical properties of a model Ag/polyvinylidene fluoride (PVDF) NC exposed to a polarized electric field is examined. This is first modeled by varying NP loading (volume fraction) for different sizes and shapes of nine geometrically-different Ag clusters. In addition, one polydisperse system is modeled, constructed with two different inclusions. Although experimental monodispersity is not yet feasible, particle size distributions are narrowing in Ag/polymer NCs. [67]

To model the effect of NP shape and structure on optical properties, simulations are performed at constant loading, using one of twenty nanodisks and nanorods. Nanostructures are varied in aspect ratio with the goal of elucidating its role on the imaginary dielectric constant from polarized electric fields. The influence of crystallographic projections in NPs is examined. Moreover, the end-cap morphology of nanorods provides an additional adjustable parameter for spectral shape. In addition to pentagonal pyramidal end-caps on nanorods, nanobars and nanorice have blunt or hemispherical-like termini, respectively. [134] These three elongated forms are modeled, along with the NCs, with the aim of understanding their properties through electronic structure. One implication of using a fixed volume fraction of 4.2%vol is the variation in interparticle separation between NP images, which is known to affect absorption peak height and energy.

In all systems, simulation cells, augmented with PBC, had a single twelve to thirty-one atom Ag NP enshrouded in 416 to 1250 atoms (69-208 monomers) of PVDF. Although the NPs we studied were limited to dimensions smaller than those typically encountered experimentally, these models should provide significant physical insight. The NPs are theoretical models that do not consider structural defects, silver oxide formation or presence of adsorbed atmospheric molecules, like H_2O.

The Ag/PVDF NC has been shown to have a large ϵ_1 at low frequencies, [135–137] and could, therefore, be used in capacitor applications. The polymer (H–$[CH_2–CF_2]_n$–H) is in widespread use, either by itself or in NCs, as a result of its range of exotic properties: polymorphism, [138] poling, [139] piezoelectricity, [140] pyroelectricity [141] and ferroelectricity. [142] Silver NPs are often incorporated in matrices without surfactant layers. Thus, their use here makes it unnecessary to introduce additional boundary atoms which would otherwise lead to more ambiguities in the unit cells.

1.4 Overview

This thesis is organized as follows. Chapter 2 explains the design of simulation cells and the levels of theory that were applied. These include force field methods and density functional theory. Chapter 3 presents and discusses the influence of NP volume fraction on optical properties of Ag/PVDF. Spectra are related back to the density of states, and a polydisperse system is also investigated. In Chapter 4, trends in the imaginary dielectric constant from NCs with nanodisks and nanorods are examined. Structures are varied in aspect ratio, nanodisk crystallographic projections, and nanorod end-cap morphology. Conclusions are given in Chapter 5. Appendix A provides additional information on running simulations. Appendix B presents additional spectra. Appendix C lists simulation cell sizes, interparticle distances and NP coordinates.

Chapter 2

Models and Methods

This chapter explains our computational approach to model optical property trends in NCs. In short, molecular systems were designed graphically, followed by compression to bulk densities using classical molecular dynamics (MD). Density functional theory (DFT) was then employed to calculate optical properties. In addition to explaining procedural details in this chapter, theoretical background is briefly reviewed in order to highlight the inherent approximations in the methods.

2.1 Construction of NC Systems

Two NC systems of PVDF with Ag inclusions were built using GaussView, both with a 13 Ag atom cuboctahedron, and one with a PVDF chain of 416 atoms and the other with 1250 atoms. Each Ag atom coordinate was input directly into the list of simulated atoms, using crystalline face-centered-cubic (fcc) packing. A single polymer chain was then designed and positioned with one tail end near the inclusion. Individual polymer dihedral angles were then selected and bent in order to twist and wrap the polymer around the Ag cluster while ensuring inter-atomic distances of at least 3 Å. Thus, the NP was completely enshrouded in the polymer, forming an almost spherical system. Large volumes of empty space throughout the polymer matrix were inevitable with such an approach. These voids were removed by forcing the system into a simulation box with periodic boundary conditions (PBC), using molecular dynamics (see Subsection 2.2).

Due to the difficulty of compressing low-density systems from GaussView with MD, additional systems with different sized inclusions and/or volume ratios were made from already MD-compressed systems. Larger Ag inclusions were incorporated into the matrix by adding additional atoms to the pre-existing inclusions in

the simulation cells, or simply replacing one NP with another, always followed by re-equilibration with MD. Different volume fractions were made by removing monomer units from the polymer chain and re-specifying terminal atoms.

A total of twenty-six silver inclusions were studied, and are presented in Figure 2.1. Their dimensions and aspect ratio are presented in Table 2.1, and their coordinates in Appendix C. The NPs considered here were built to model the effects of distinct geometrical features, rather than as target inclusions in themselves, and have therefore not been optimized geometrically as bare inclusions. NP spectra presented here are meant to be compared qualitatively with the appropriate NC spectra, rather than with literature spectra for optimized Ag clusters. For the amorphous minimum energy clusters H and I, comparisons with experimental results [143] show good agreement when a rigid 0.5 eV blue-shift (scissor operator) is applied to the NP spectra reported here. Numerous studies have examined optical properties of Ag clusters and NPs both experimentally [143–149] and theoretically with: DFT [150], time dependent-DFT [108, 143, 151–154], Mie theory [155] and the discrete dipole approximation. [59, 156–160]

Many of the crystalline NPs studied here are in the shape of disks and rods, as included in Figure 2.1. Nanodisks consist of two atomic layers (a bilayer) in either the {111} facet (NPs E, J–R) or {100} facet (NPs S–V). Nanorods consist of multiply stacked layers (up to 7,) from the {111} facet (NPs X–Z) or {100} facet (NPs F and W). Bilayer disks have recently been reported experimentally, [88] though with larger diameters. In fact, absorption spectra of small atomic clusters in the range of 12–31 atoms (the size of our model clusters) have been studied experimentally, though with (near) minimum energy geometries that differ from our NPs. [147, 161–165]

Polarized electric fields are directed along two symmetry axes of the NPs, as shown in Fig. 2.2. For nanorods, fields are directed along the principal axis (longitudinal, z-axis) and a perpendicular axis (transverse, x-axis). For nanodisks, normal mode polarization is along the normal vector of the disk, and the transverse mode is incident along the side.

In what follows, specific NC mixtures are referred as, e.g.: X/416, where the letter indicates the inclusion size and geometry as shown in Figure 2.1, and the number indicates the length of the polymer chain. The percent silver by volume (%vol) is also included, in places in the discussion where it is relevant. Inclusion axes (as explained in the figure caption) are oriented in line with the respective axes of the simulation cells.

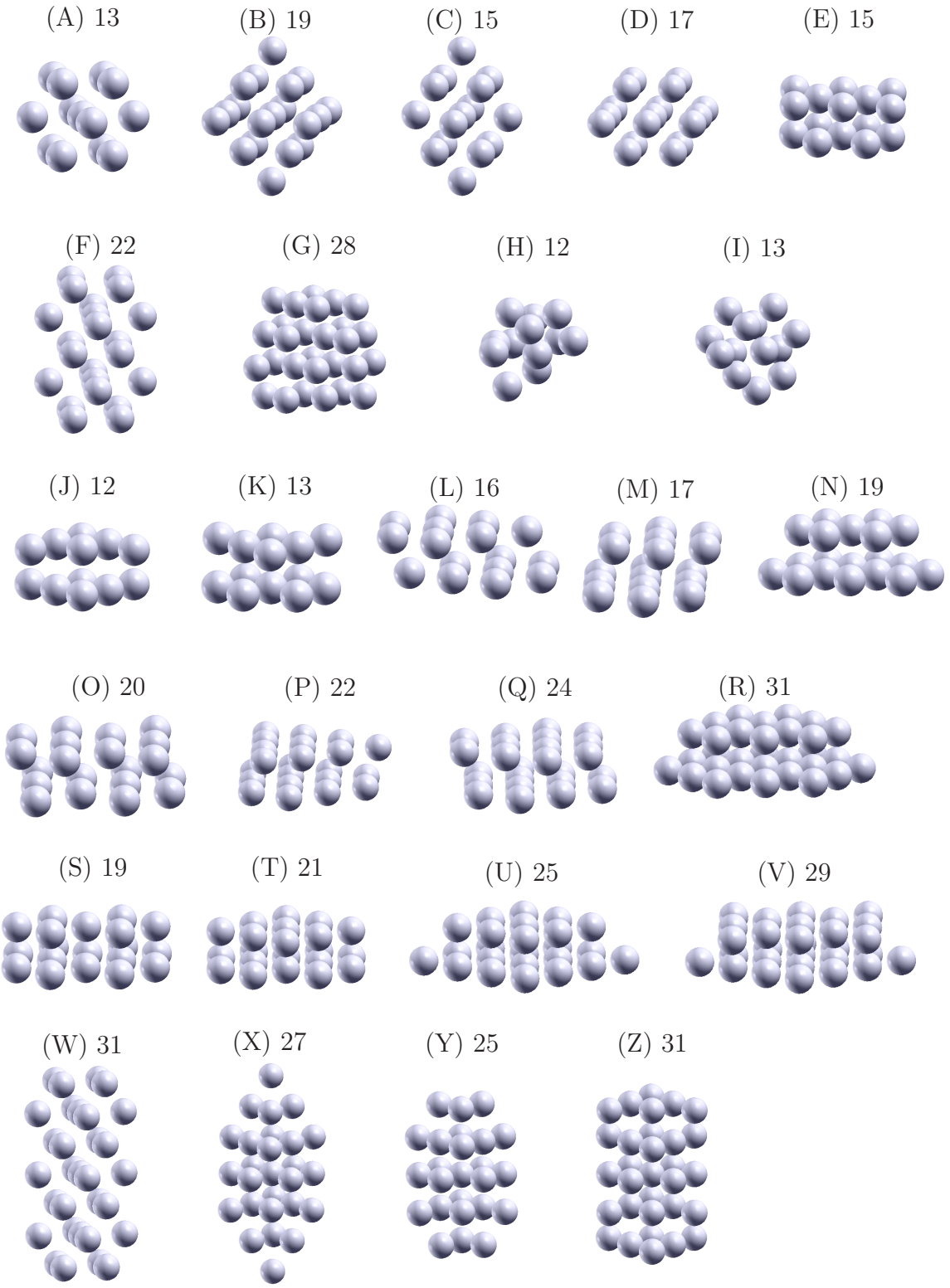

Figure 2.1: Silver NP inclusions. z-axis runs vertically from top to bottom of page; x-axis runs horizontally from left to right of page. Numbers next to the panel labels indicate the number of atoms in the NP.

Table 2.1: NP dimensions (Å) and aspect ratio (A) (z/x). Inclusion diameters have an additional 2.889Å added to the largest internuclear distances.

NP	X	Y	Z	A
A	8.670	8.670	6.980	0.81
B	8.670	8.680	11.070	1.28
C	8.670	8.670	11.070	1.28
D	8.670	8.660	6.970	0.80
E	8.670	8.730	5.250	1/1.65
F	8.670	8.670	11.060	1.28
G	9.020	9.020	9.020	1.00
H	7.470	7.280	9.835	1.32
I	8.210	8.260	9.210	1.12
J	8.670	9.570	5.250	1/1.65
K	8.670	8.730	5.250	1/1.65
L	11.230	8.670	5.250	1/2.14
M	8.720	11.550	5.250	1/1.66
N	11.560	10.390	5.250	1/2.20
O	11.050	8.540	5.200	1/2.13
P	11.230	11.550	5.250	1/2.14
Q	11.230	11.550	5.250	1/2.14
R	14.450	12.890	5.250	1/2.75
S	11.060	11.060	4.930	1/2.24
T	11.030	11.020	4.920	1/2.24
U	15.150	15.150	4.930	1/3.07
V	15.150	15.150	4.930	1/3.07
W	8.670	8.670	15.150	2.17
X	8.670	9.570	17.040	1.97
Y	8.670	9.570	12.330	1.42
Z	8.670	9.570	12.330	1.42

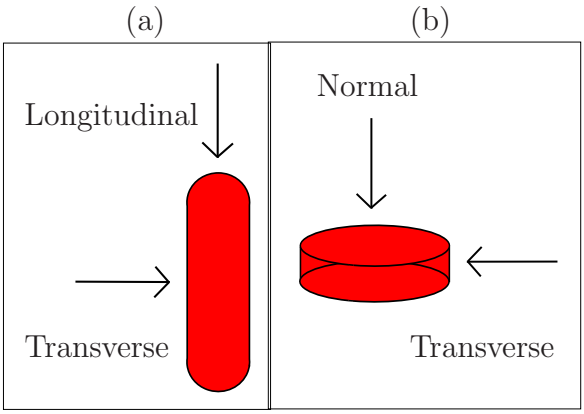

Figure 2.2: Polarized field directions in nanorods and nanodisks. Panel (a) shows longitudinal and transverse resonances in rods. Panel (b) shows normal and transverse resonances in disks.

2.2 Molecular Mechanics and Dynamics Simulations

MD with pressure coupling was used to compress low-density systems, and molecular mechanics (MM) was used to minimize the energy of the system into a local minimum. Subsection 2.2.1 explains the physics behind these approaches as applied to the current simulations, and Subsection 2.2.2 discusses the specific implementation.

2.2.1 MM/MD Theory

Classical MM and MD calculate the forces between atoms from a set of Newtonian mechanics-based equations of motion that together form a force field. MM simulations are run at zero Kelvin, and atomic movement is toward a minimum energy structure. The simulation terminates when the specified minimum energy tolerance is attained. MD simulations have temperature, with atomic velocities assigned based on the Boltzmann distribution. Atoms continue moving over the specified duration of time.

A force field consists of mathematical equations which describe both bonding and non-bonding forces (or potential energy). Force ($\boldsymbol{F}$) has direction, indicating the path to lower energy (V). Energy is related to the force as:

$$\boldsymbol{F} = -\nabla V. \tag{2.1}$$

Further physical descriptions of force fields is limited here to that implemented in the present simulations. (The interested reader is referred elsewhere, see e.g. Ref. [166].) Atomic interactions were assigned for bond-stretching, bond-bending, electrostatic van der Waals potentials and coulombic interactions between partially charged atoms. The potential energy felt by a particular atom is the sum of these interactions.

Harmonic bond stretching is represented quadratically:

$$V_s(r_{ij}) = \frac{1}{2} k^s_{ij} (r_{ij} - r^0_{ij})^2 \tag{2.2}$$

where V_s is the bond-stretching potential, k^s_{ij} is the bond-stretching constant between two bonded atoms i and j, r_{ij} is the distance between the two atoms and r^0_{ij} is the equilibrium bond length between the two atoms.

Although angle bending is also frequently modeled with a harmonic potential,

cosine functions are employerd which have increased numerical stability [167]:

$$V_b(\theta_{ijk}) = \frac{1}{2}k^b_{ijk}\left[cos(\theta_{ijk}) - cos(\theta^0_{ijk})\right]^2 \tag{2.3}$$

where V_b is the angle bending potential, θ_{ijk} is the angle formed between bonded atoms i, j and k, k^b_{ijk} is the angle-bending constant between the three atoms and θ^0_{ijk} is the equilibrium bond angle.

Electrostatics are calculated with the Lennard-Jones potential, accounting for long-range attraction from induced-dipole–induced-dipole interactions and short-range repulsion from orbital overlap:

$$V_{LJ,ij} = 4\epsilon\left[\left(\frac{\sigma_{ij}}{r_{ij}}\right)^{12} - \left(\frac{\sigma_{ij}}{r_{ij}}\right)^{6}\right] \tag{2.4}$$

where $V_{LJ,ij}$ is the Lennard-Jones potential between atoms i and j, $\epsilon = \epsilon_0\epsilon_r$ with ϵ_r as the relative dielectric constant of the medium and ϵ_0 as the permittivity of free space, σ_{ij} is the distance at which the interparticle potential is zero between two atoms and ϵ_{ij} is the depth of the potential well of attraction.

The Coulombic potential (V_C) is given by:

$$V_C = \frac{q_i q_j}{4\pi\epsilon r_{ij}} \tag{2.5}$$

where q is the partial atomic charge.

Force field methods, while adequate for simulations of large atomic systems where bond-breaking or forming does not occur, suffer from the need of parameterization: equilibrium geometries (e.g. bond lengths, angles, etc.) and force constants (e.g. k_s, k_b, etc.) must be specified. These parameters are often system dependent, and parameterized either from experimental data (semi-empirical) or high-level quantum calculations (ab initio).

2.2.2 MM/MD Implementation

Gromacs 4.0.4 and 4.0.7 [168–171] was used for force field simulations that were necessary to compress the structures to an approximate density, keeping silver atoms frozen, and preserving orthorhombic cells under PBC. These runs were also used to expand simulation cells whose density was too large – a result of incrementally increasing NP size, as explained in Section 2.1. The target density was calculated using the bulk densities of the two constituents (PVDF–1.77 g·cm^{-3}, Ag–10.49 g·cm^{-3}) and

their respective volume ratios.

Structural compression was performed under constant number of atoms (N), pressure (P) and temperature (T). The isotropic Parrinello-Rahman pressure coupling algorithm [172] was used to keep the pressure constant. Nose-Hoover temperature coupling [173,174] was used to maintain a constant temperature of 1000 K. The pressure coupling parameters had to be manually increased and modified since such an automated feature was not available. The compressibility factor was set at 0.1 bar^{-1}. Each time a run completed 50,000 steps, with step sizes of 0.001 ps, the pressure was increased initially by increments of 10^2 bar, and later by 10^3 bar, until the correct density was attained – near 30,000 bar. If the run failed, the time pressure coupling parameter was increased (usually between 25 – 100 ps) until stability was reached and the run could finish. Once the required density was attained, structures were annealed for almost 1 μs from 1000K to 25K, followed by energy minimization using the conjugate-gradient algorithm. Additional information on the use of Gromacs is provided in Appendix A.

The force field parameters used in the current simulations are presented in Table 2.2. Approximate bond lengths with very stiff harmonic stretching constants were taken from Ref. [175] Harmonic angle bending terms were those of Chen and Shew. [176] To access as many conformations as possible in the polymer, torsional motion was assigned to be barrierless. Coulombic interactions were calculated from assigned partial atomic charges for all atoms. Parameters for C, H and F were based on those in Ref. [176], but were modified slightly in order to form zero-charge groups. Silver atoms had zero charge. Non-bonding Lennard-Jones parameters were taken from the Universal Force Field (UFF), [177] and were combined geometrically. Long-range electrostatics were calculated with the Particle Mesh Ewald (PME) method, [178] and the cutoff distances kept as large as possible, up to 0.9 nm, depending on the size of the simulation box.

An MD-equilibrated simulation cell for the A/1250 NC (1.7%vol) is shown in Figure 2.3. Atoms that appear dangling at the cell edges have their valencies satisfied by the PBCs. Symmetric inclusions were oriented with their principal axes along a lattice cell vector. Amorphous clusters were packed with their Cartesian coordinates (as reported in Appendix C) in line with the respective lattice cell vectors. Simulation cell dimensions for all the NCs are also reported in Appendix C.

Table 2.2: Force field parameters

Bond[a]	x_0	$k_s \cdot 10^{-5}$
C-C	1.53	5
C-H	1.09	5
C-F	1.36	5
Angle	θ_0	k_b
C-C-C	118.2	900
C-C-H	109.3	900
C-C-F	107.7	900
H-C-H	109.3	900
F-C-F	105.3	900
F-C-H	108.0	900
Group	q_C	q_H,q_F
CH_2	-0.36	0.18 , -
CF_2	0.46	- , -0.23
Terminal CF_2H	0.46	0.00 , -0.23
Starting CH_3	-0.48	0.16 , -
Atom	$\epsilon \times 10^{-2}$	σ
H	4.40	2.571
C	10.50	3.431
F	5.00	2.997
Ag	3.60	2.805

[a]Equilibrium bond lengths (x_0) are given in Å. Stretching (k_s) and bending (k_b) force constants are given in kJ/(mol·nm). q_X are partial charges (in units of electron charge) on atoms of type X in the group indicated in the left column. ϵ is given in kJ·mol^{-1} and σ in Å.

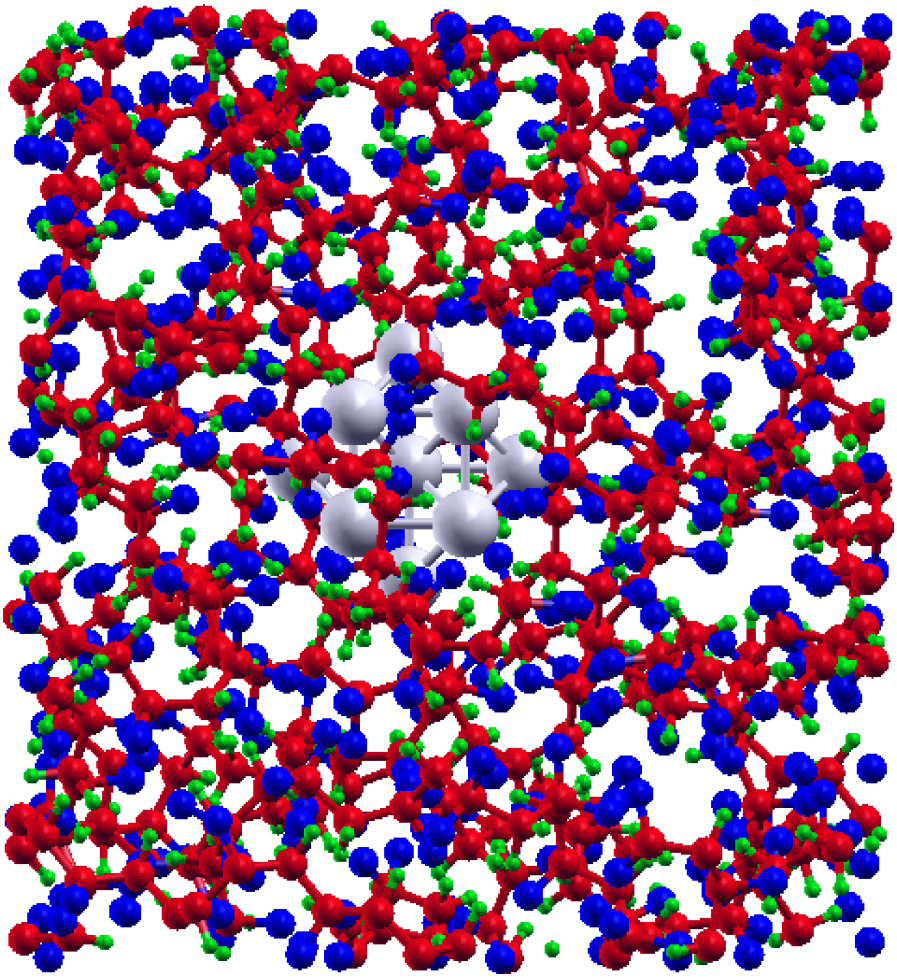

Figure 2.3: Snapshot of a simulation cell with PBC with 1250 PVDF atoms and a 13 atom Ag cuboctahedron (A/1250). For clarity, silver atoms are grey, fluorine is blue, carbon is red, and hydrogen is green. z-axis runs from top to bottom of page and x-axis runs from left to right of page.

2.3 Density Functional Theory Calculations

Density Functional Theory (DFT) was used to calculate optical properties of NPs and NC systems. In addition, the density of states (DOS) and electronic band structure were computed. A brief theoretical overview of DFT and the pertinent optical and electronic properties are given in Subsection 2.3.1. DFT settings and implementation are explained in Subsection 2.3.2.

2.3.1 DFT Theory

Kohn-Sham DFT

The success of DFT is based on solving the Schrodinger equation using electron density ($\rho(\mathbf{r})$), which depends on only 3 spatial coordinates, instead of 3N coordinates for a system of N electrons, as used in other quantum methods. This approach substantially reduces computation time, making quantum calculations feasible for larger molecules. It is an exact method, founded on the Hohenberg and Kohn theorems, [179] which state that the electronic ground state energy can be uniquely determined by the electron density using the variational principle.

In the Kohn-Sham (KS) approach, [180] the electron density (ρ) is written as a sum of N non-interacting orbitals (ϕ_i):

$$\rho = \sum_{i}^{N} |\phi_i(\mathbf{r})|^2, \tag{2.6}$$

which would be exact if the orbitals were exact. The total energy is a sum of electrostatic and kinetic terms, which are functionals of the electron density:

$$E[\rho(\mathbf{r})] = T_e[p(\mathbf{r})] + E_{n-e}[p(\mathbf{r})] + E_{e-e}[p(\mathbf{r})] + E_{n-n}[p(\mathbf{r})], \tag{2.7}$$

where the square brackets indicate a functional, T_e is the kinetic energy of the electrons, E_{n-e} is the nucleus-electron attractive energy, E_{e-e} is the electron-electron repulsive energy and E_{n-n} is the nucleus-nucleus repulsion. These terms have their usual quantum forms, and details can be found in one of many standard texts (e.g. Refs. [132, 166]). The KS wavefunction is constructed from single electron orbitals:

$$\left(\frac{-\hbar^2}{2m_e}\nabla^2 + \nu_{\text{eff}}(\mathbf{r})\right)\phi_i(\boldsymbol{r}) = \epsilon_i\phi_i(\boldsymbol{r}), \tag{2.8}$$

where h is Planck's constant and $\hbar = h/2\pi$, m_e is the mass of the electron and ν_{eff} is

the external effective potential (quantum electrostatic potentials including exchange and correlation).

Optical Method in DFT

Once a self-consistent solution has been obtained, the frequency-dependent Lindhard dielectric function (ϵ) may be calculated through dipolar interband transitions using the random phase approximation, [124, 126, 181] which is available with the SIESTA software package. Electrons respond to an average electric potential, and their excitations are modeled by a Lorentz oscillator: [182]

$$m_e \frac{d^2\boldsymbol{r}}{dt^2} + m_e\Gamma\frac{d\boldsymbol{r}}{dt} + m_e\omega_0^2\boldsymbol{r} = -e\boldsymbol{E_{loc}}(t). \tag{2.9}$$

The dipoles at position ($\boldsymbol{r}$) are driven by the electric field ($\boldsymbol{E_{loc}}$), and return to their ground state based on Hooke's Law with a damping term Γ. ω_0 is the resonant angular frequency and the nuclei are assumed stationary. It can then be shown (see e.g. [182]) that for a system of N electrons:

$$\epsilon_r(\omega) = 1 + \frac{Ne^2}{\epsilon_0 m_e}\sum_{j=1}^{N}\frac{1}{\omega_j^2 - \omega^2 - i\Gamma_j\omega}. \tag{2.10}$$

For quantum mechanical systems, this becomes [124, 126, 181]:

$$\epsilon_r(\omega) = 1 - \frac{e^2\hbar^2}{\epsilon_0 m_e^2 V}\sum_{\boldsymbol{k}}\sum_{i,j}\frac{|\boldsymbol{\mu}_{i,j}(\boldsymbol{k})|^2}{E_{i,j}^2}\frac{f_0(E_j(\boldsymbol{k})) - f_0(E_i(\boldsymbol{k}))}{E_{i,j} - \hbar\omega - ih\Gamma}, \tag{2.11}$$

where V is the volume of the cell. The sum ranges over all $\boldsymbol{k}$-points in reciprocal space with a double sum over all electronic energy (E) values i and j. f_0 is the Fermi distribution function (which equals one if the state is populated and 0 if not) and $E_{ij} = E_i(\boldsymbol{k}) - E_j(\boldsymbol{k})$. The transition state dipole moment ($\boldsymbol{\mu}_{i,j}(\boldsymbol{k})$) represents the probability of a transition, given by:

$$\boldsymbol{\mu}_{i,j} = \langle\phi_i(\boldsymbol{r}) \mid \hat{\mu} \mid \phi_j(\boldsymbol{r})\rangle = \langle\phi_i(\boldsymbol{r}) \mid e\cdot\boldsymbol{r} \mid \phi_j(\boldsymbol{r})\rangle, \tag{2.12}$$

where $\hat{\mu} = e\boldsymbol{r}\cdot$ is the dipole operator. Since an oscillating electric field sets electronic dipoles into oscillatory motion, excitations from occupied to unoccupied states occur only if the polarization of the field is able to produce the required change in dipole moment. The probability of a transition is proportional to $\boldsymbol{\mu}_{i,j}(\boldsymbol{k})$. Thus, not all transitions necessarily occur between ground and excited states for a given polarized

field.

This method of calculating the imaginary relative dielectric constant from direct, dipolar interband transitions from ground to excited states makes a number of approximations. Foremost is the absence of local field effects, in which the external field is assumed equal to the microscopic field acting on individual electrons. Indirect transitions, which occur when the electron wave vector changes through coupling with a phonon, are ignored. Experimentally, they occur much less frequently than direct transitions. The calculated absorption spectrum only includes single particle excitations, and does not model collective oscillations. Variations in the effective mass of electrons (self-energy), and electron-hole interactions are also neglected.

Given these approximations, the Kramers-Kronig relations then convert the imaginary part to the real part: [183]

$$\epsilon_1(\omega) = 1 + \frac{2}{\pi}\mathcal{PV}\int_0^\infty \frac{\omega'\epsilon_2(\omega')}{(\omega')^2 - (\omega)^2}\, d\omega', \tag{2.13}$$

where PV is the Cauchy principal value. Similarly, ϵ_2 can be calculated from ϵ_1, as:

$$\epsilon_2(\omega) = -\frac{2\omega}{\pi}\mathcal{PV}\int_0^\infty \frac{\epsilon_1(\omega')}{(\omega')^2 - (\omega)^2}, d\omega'. \tag{2.14}$$

Optical Properties

The complex dielectric constant ($\epsilon_r = \epsilon_1 + i\epsilon_2$) is a measure of the ability of a material to store electrical energy. A vacuum has by definition $\epsilon_1 = 1$, and increases for materials that are able to hold an electric potential. The imaginary part (ϵ_2) represents energy loss, primarily through heat, as a result of electrical conduction. The complex notation is convenient as it represents phase lag between the applied field and the material response. A number of other optical properties can be easily obtained through simple mathematical transformations. [182]

The electrical conductivity (σ) is given by:

$$\sigma(\omega) = \epsilon_2(\omega)\ \omega. \tag{2.15}$$

The real part of the refractive index (n_1), or ratio of the speed of light through the material (v) to the speed of light in vacuum (c), ($n_1 = v/c$), can be calculated

from the dielectric constant as:

$$n_1(\omega) = \sqrt{\frac{\sqrt{\epsilon_1(\omega)^2 + \epsilon_2(\omega)^2} + \epsilon_1(\omega)}{2}}. \tag{2.16}$$

The imaginary part of the refractive index (extinction or absorption coefficient, κ or n_2) is also a measure of energy loss, as explained for ϵ_2, and given by:

$$n_2(\omega) = \sqrt{\frac{\sqrt{\epsilon_1(\omega)^2 + \epsilon_2(\omega)^2} - \epsilon_1(\omega)}{2}}. \tag{2.17}$$

Solving for the dielectric function reveals a simpler relation:

$$\epsilon_1(\omega) = n_1^2(\omega) - n_2^2(\omega), \tag{2.18}$$

$$\epsilon_2(\omega) = 2n_1(\omega)\ n_2(\omega). \tag{2.19}$$

The absorption coefficient (α) is a measure of the distance a wave travels before its intensity is decreased by $1/e$:

$$\alpha(\omega) = \frac{4\pi\ n_2(\omega)}{\lambda} = \frac{\epsilon_2(\omega)\ \omega}{n_1(\omega)\ c}. \tag{2.20}$$

The reflectance at normal incidence (R) is the fraction of the field that is reflected from the surface:

$$R(\omega) = \frac{(n_1(\omega) - 1)^2 + n_2^2(\omega)}{(n_1(\omega) + 1)^2 + n_2^2(\omega)}. \tag{2.21}$$

Density of States and Band Structure Calculations

The energy of incident radiation required to produce an electronic excitation must be equal to the energy difference between the unoccupied and occupied orbitals. The density of states (DOS) describes the distribution of the number of occupied and unoccupied states per unit of energy. Although these states are discrete, experimental spectra are often broadened due to temperature, which populates higher energy vibrational and rotational states. In computational simulations, spectral broadening is mimicked by applying user-defined Gaussian broadening terms.

The band gap can be visualized through a plot of the DOS, showing the position of the highest occupied molecular orbital (HOMO) and the lowest unoccupied molecular orbital (LUMO). At zero Kelvin, the Fermi energy (E_F) is defined as the energy of the highest occupied orbital. At non-zero temperatures, higher energy states are

probabilistically populated according to the Boltzmann distribution, and for semiconductors and insulators E_F shifts into the band gap. Additional information can be found in Ref. [184]. DFT is well-known to underestimate the band gap in semiconductors and insulators as a result of poor treatment of exchange energy, [185] and this is often corrected by applying a rigid shift (scissor operator) to all states above E_F. [185–187]

Electronic band structure calculations plot the energy eigenvalues as a function of coordinate path in reciprocal space. Crystalline materials exhibit non-linear band lines across the first Brillouin zone (BZ), while amorphous materials have orbital energies that are constant throughout.

2.3.2 DFT Implementation

The software package, SIESTA: Spanish Initiative for Electronic Simulations with Thousands of Atoms [188, 189] version 2.0.2 was used for all DFT calculations. The Generalized Gradient Approximation (GGA) and the ab initio PBE functional [190] were used to calculate the exchange-correlation energy. Pseudopotentials were used of the norm-conserving Troullier-Martins [191] type, taken from the SIESTA website. A DZP basis set was used for valence orbitals: H–$1s^1$, C–$2s^2 2p^2$, F–$2s^2 2p^5$, Ag–$5s^1 4d^{10}$. Calculations in reciprocal space used only the gamma point, justified since the cell size was large and the system was not a conductor. The density matrix was solved by diagonalization with a mesh cutoff of 500 Ry to ensure numerical convergence. Additional information on run settings are provided in Appendix A.

ϵ_2 was calculated with an optical mesh of $1 \times 1 \times 1$, included all bands, and scanned a large frequency range of 0.001–100.000 eV in order to ensure reliable conversion using the Kramers-Kronig relations. Since experimental data was not available to fit calculated results, a minimal peak broadening factor of 0.050 eV was used to ensure minimally smooth curves. Likewise, a scissor operator was not used due to a lack of comparable experimental data. Therefore, excitation energies should be considered relative to one another, rather than as absolute values.

The optical subroutine available in the SIESTA package was used to apply the Kramers-Kronig relations and convert ϵ_2 to ϵ_1, and back again to ϵ_2 to ensure consistency. This program also calculates the complex refractive index, absorption coefficient, conductance and reflectance.

Band structure calculations sampled reciprocal space trajectories between high-symmetry points: L to Γ to X and back to Γ. The amorphous NC simulation cells produced band structures that showed no dependence on position in reciprocal space:

the bands were flat.

The DOS was computed using the eig2dos subroutine available in the SIESTA package. This program takes all the eigenvalues and broadens them into Gaussian functions of user-defined width. Both broad (0.05 eV) and narrow (0.001 eV) broadening factors were used.

The stability of NPs was quantified through binding energy calculations:

$$E_b(Ag_n) = E(Ag) - \frac{E(Ag_n)}{n}, \tag{2.22}$$

where E_b is the binding energy per atom, $E(Ag_n)$ is the energy of Ag_n and n is the number of atoms in the cluster. Larger binding energies correspond to increased particle stability.

Computer Requirements

High performance computing was performed through the Western Canada Research Grid (WestGrid), partner consortia to Compute Canada. Core speed averaged 2.4 GHz each with 1GB RAM and interconnected with Infiniband. The computational demand for MM and MD calculations was minimal: with one core, energy minimizations (MM) took less than 1 minute; annealing or pressure coupling runs (MD) took less than 1 hour. DFT calculations were intensive. While energy minimization was barely feasible with a small system, it was not practical for the numerous systems of increased size. Optical calculations required significant amounts of RAM that was accessed in part by using additional cores. Up to 64 cores were used in parallel, taking up to 7 days to complete a single-point optical calculation.

2.4 Effects of Energy Minimization & Spin Polarization

A number of numerical checks were performed. For the A/416 MD-minimized structures, optical properties were recalculated after the cell was re-optimized using PBE/-DZP, using both wavefunctions that allowed for the possibility that the electron spin might become polarized, and wavefunctions that did not allow for this possibility. (Spin-polarization is the use of different orbitals for different spin states. Non-spin-polarized calculations have degenerate orbitals for both spins. [132]) As shown in Figure 2.4, results from spin-polarized and non-spin-polarized systems were virtually indistinguishable (compare panels (a) and (b), as well as (c) and (d)). As a result, all

additional simulations were performed without allowing for spin-polarization in order to minimize computation time. The calculated optical properties changed modestly as a result of DFT energy minimization (compare panels (a) and (b) with (c) and (d)). MD-minimized structures were used for the other models. PBE/DZP-based minimizations quickly become computationally intractable for the system sizes investigated. Subsequent interpretations must be mindful of the level of uncertainty implied by the results shown in this figure.

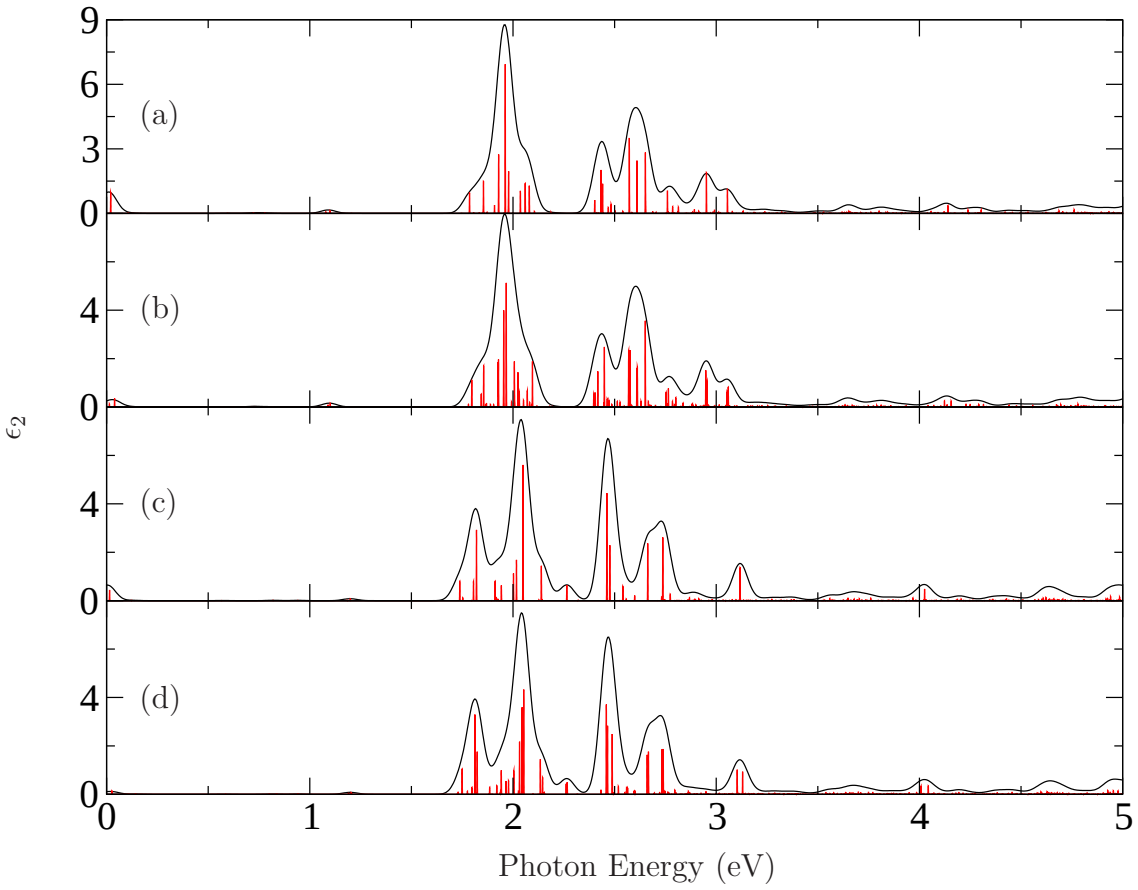

Figure 2.4: Imaginary part of dielectric constant (ϵ_2) from MM- and DFT-minimized A/416 (5.1%vol) systems with and without spin-polarization from x-axis polarized field. Panels show NC from (a) MM-minized, without spin-polarization, (b) MM-minimized, with spin polarization, (c) DFT-minimized without spin-polarization and (d) DFT-minimized with spin polarization. Black lines show a Gaussian energy broadening of 0.05 eV, and the red lines illustrate the energies of specific transitions with a finer broadening of 0.001 eV.

Chapter 3

Results and Discussion: Nanoparticle Volume Fraction Effects

This chapter presents and discusses results pertaining to trends from Ag NP volume fraction effects in PVDF. In Section 3.1, the NC density of states (DOS) is examined, and compared to those of the individual constituents. Section 3.2 discusses all seven frequency-dependent optical parameters for an isotropic NP inclusion and its NC as a function of NP loading. The imaginary dielectric constant is compared from anisotropic NPs and NCs in Section 3.3. Lastly, the influence of polydispersity is examined using two different sized NPs in Section 3.4.

3.1 Density of States

The density of states (DOS) of pure PVDF, NP A in vacuum, A/416 NC (5.1%vol) and A/836 NC (2.6%vol) are shown in Figure 3.1. The zero of energy on the DOS graphs in all panels is the Fermi energy (E_F).

Pure PVDF was found to have a large band gap of almost 7 eV (see Figure 3.1(a)), comparable to the 6.5 eV frequently cited in the experimental literature. [192–194] NP A has a discrete spectrum, and is also an insulator (see Figure 3.1(b)), as are the other NPs studied herein. However, the NP HOMO-LUMO gaps are much smaller than that of PVDF, and they have many states within a few eV of the Fermi level.

When the Ag NPs were incorporated in PVDF, notable differences were seen in the numbers and positions of energetic states (see Figure 3.1(c) and (d)). While the states of the polymer and NP did not strongly interact, the presence of the NP

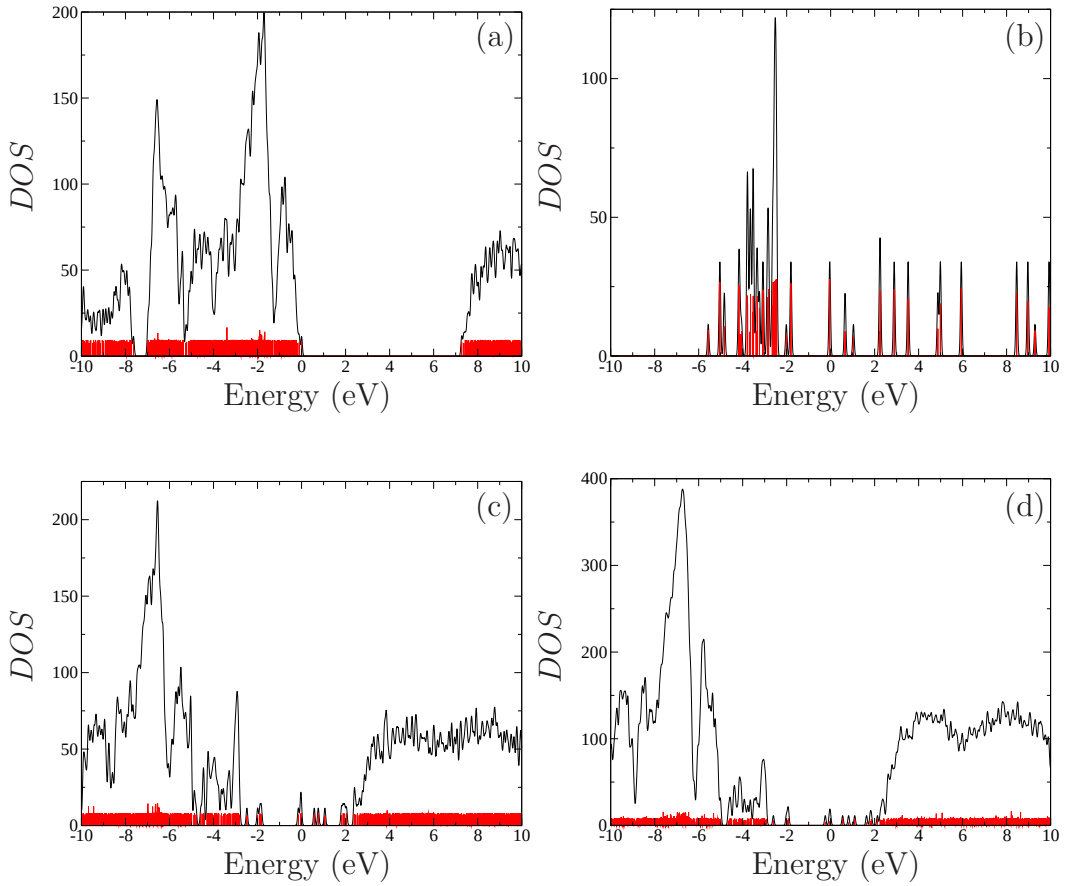

Figure 3.1: Density of states (DOS) of (a) amorphous PVDF, (b) Ag NP A in vacuum, (c) A/416 NC (5.1%vol) and (d) A/836 NC (2.6%vol). The zero on the Energy axis is set at the Fermi energy of that particular material, and its location is thus not consistent across the four graphs. Black lines show a Gaussian energy broadening of 0.05 eV, and the red lines illustrate the location of states with a finer broadening of 0.001 eV.

introduced many states into the polymer band gap. This not only provides additional opportunities for transitions, but the high occupancy of the metallic NP states results in a significant shift of the Fermi energy towards the conduction band of the polymer. Thus, in the 0 to 3 eV region of the NC DOS, there were more states than in either the NP or the polymer. These states contribute significantly to the optical response of the material for the field energies considered here.

3.2 Optical Properties of Isotropic Ag_{13} NCs

The imaginary part of the dielectric constant (ϵ_2) is directly related to the probability of interband transitions, which are associated with the DOS. It, along with the real

part of the dielectric constant (ϵ_1), complex refractive index ($n = n_1 - in_2$), absorption coefficient (α), conductance (σ) and reflectance at normal incidence (R) are presented in Figure 3.2 for PVDF over a large energy range. PVDF, having a large band gap, only shows optical resonances in the UV.

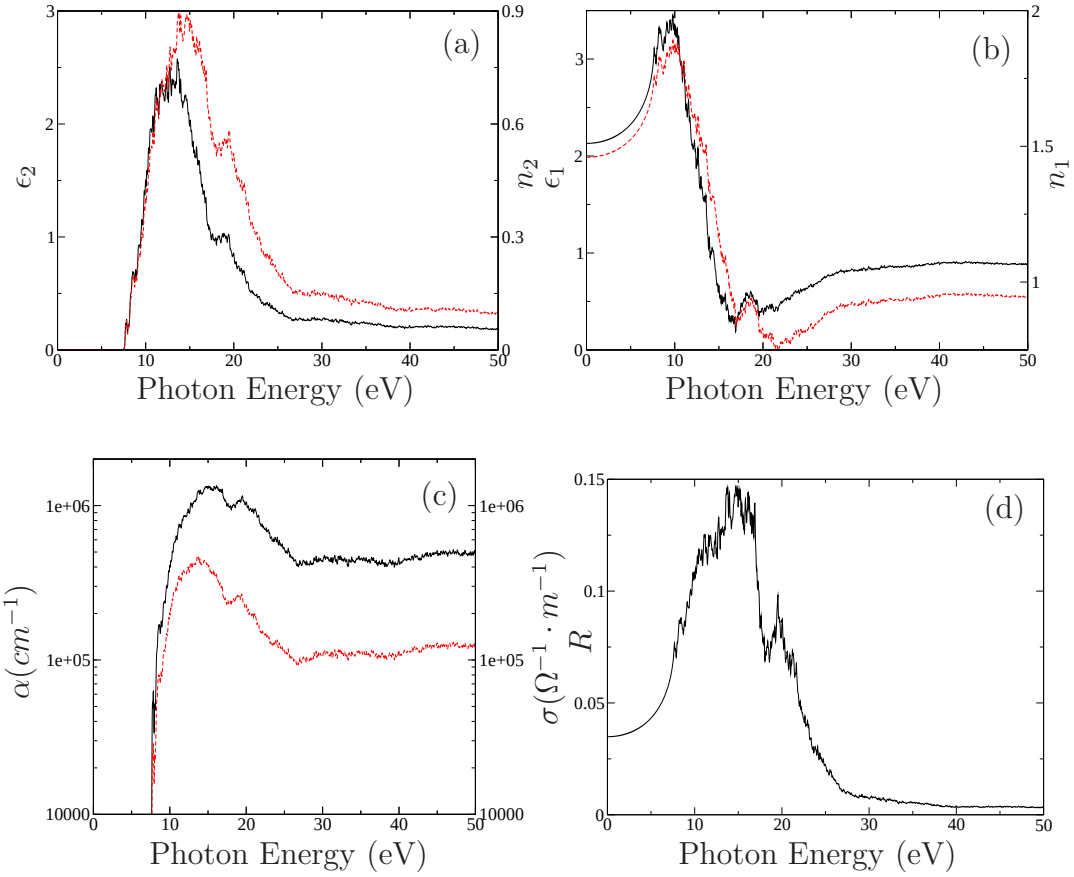

Figure 3.2: Optical properties of amorphous PVDF. Panel (a) shows the imaginary dielectric constant (ϵ_2) and imaginary refractive index (n_2), with ordinate scales along left and right sides, respectively. Panel (b) shows the real dielectric constant (ϵ_2) and real refractive index (n_1), with ordinate scales along left and right sides, respectively. Panel (c) shows the absorption coefficient (α) and conductivity (σ), with ordinate scales along left and right sides, respectively. Panel (d) shows the reflectance at normal incidence (R). Black lines correspond to the optical property labeled on the left ordinate axis, and dashed red lines corespond to that on the right.

Spectra for NP A and its NCs are shown for excitations along the x- and z-axes of the inclusions (as described in Figure 2.1) in Figures 3.3 and 3.4. Comparisons can be made between the NP spectra in vacuum (subpanels (iii)), those of the pure polymer (orange lines) and those of NCs with volume fractions between 1.7 and 5.1%vol.

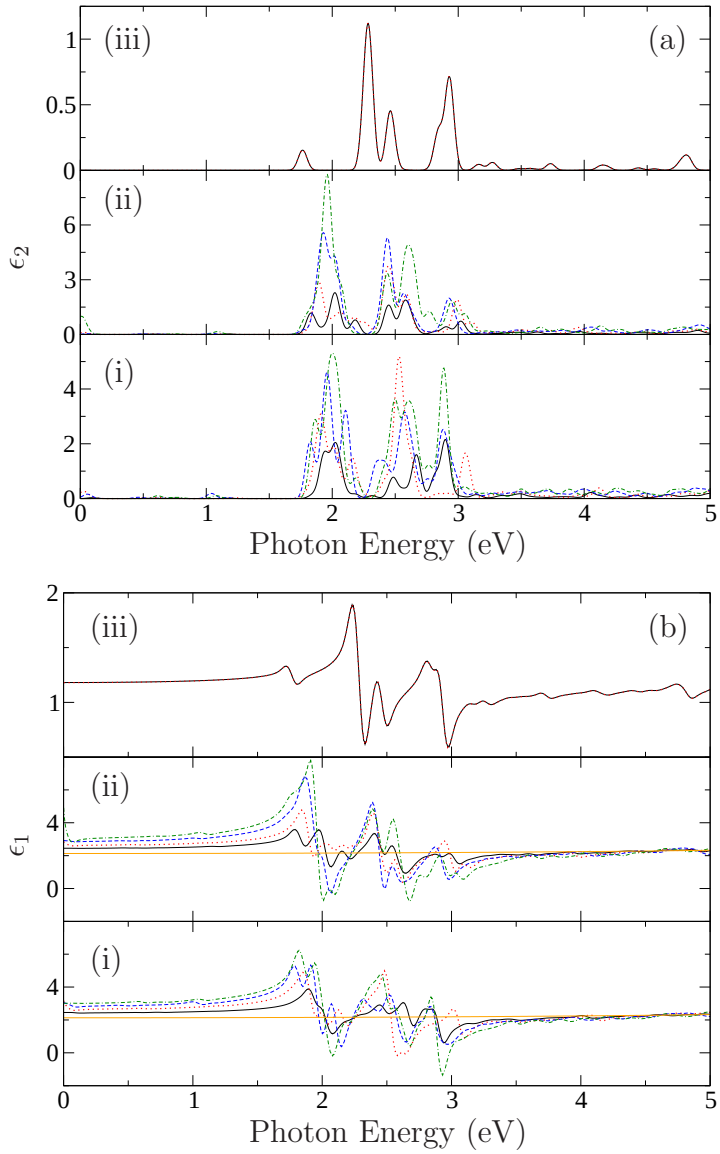

Figure 3.3: Influence of NP volume fraction and incident field polarization on the complex dielectric function ($\epsilon = \epsilon_1 + i\epsilon_2$) of NP A ($Ag_{13}$) and corresponding NC materials. Panels (a) and (b) show the imaginary (ϵ_2) and real parts (ϵ_1) of the dielectric function, respectively. In each graph, subpanels (i) and (ii) report optical properties of NCs with incident field polarized along the z- and x-axes of the NP, respectively. Subpanel (iii) presents the respective optical property of the NP in vacuum, with incident fields along the z-axis (black line) and along the x-axis (dotted red line). For the present plots, the optical properties of the pure NP do not depend on field direction, and the lines in subpanels (iii) are superimposed. In subpanels (i) and (ii), different lines correspond to different NC volume fractions, as follows: solid black – A/1250 (1.7%vol), dotted red – A/740 (2.9%vol), dashed blue – A/536 (4.0%vol) and dot-dashed green – A/416 (5.1%vol). Horizontal solid orange lines represent the pure amorphous PVDF polymer. Where the orange line is not visible, it coincides with the graph's abscissa.

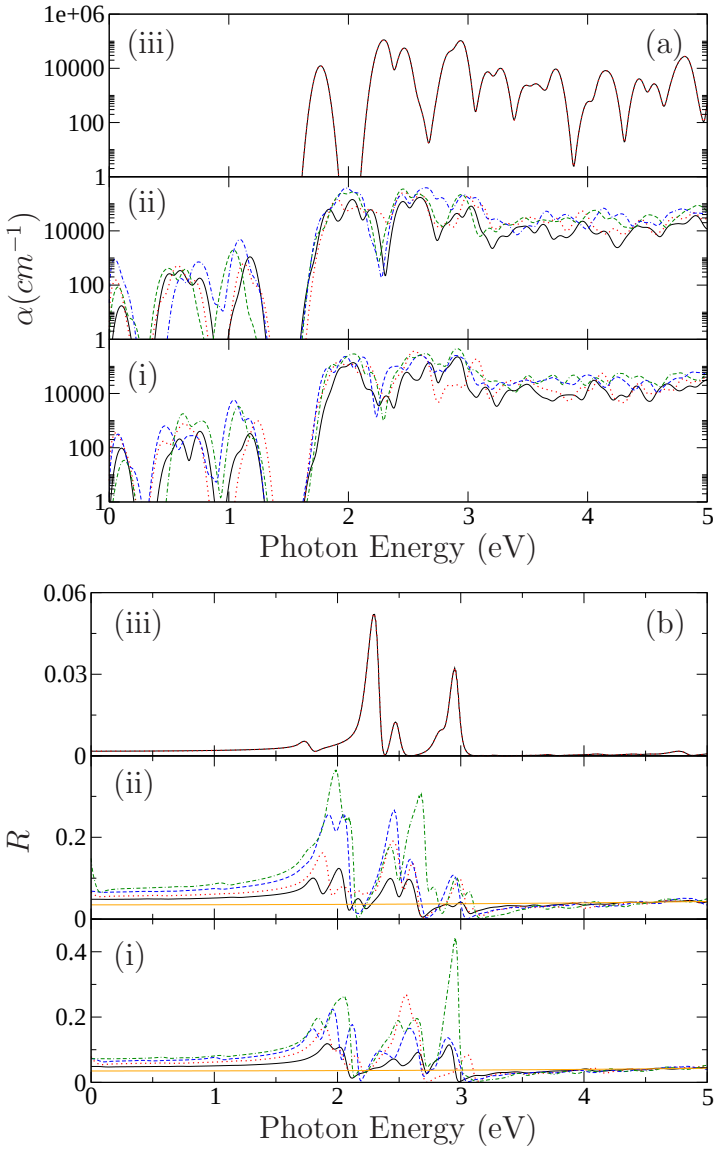

Figure 3.4: Influence of NP volume fraction and incident field polarization on the absorption coefficient (α) and reflectance at normal incidence (R) of NP A (Ag_{13}) and corresponding NC materials. Panels (a) and (b) show the absorption coefficient and reflectance, respectively. In each graph, subpanels (i) and (ii) report optical properties of NCs with incident field polarized along the z- and x-axes of the NP, respectively. Subpanel (iii) presents the respective optical property of the NP in vacuum, with incident fields along the z-axis (black line) and along the x-axis (dotted red line). For the present plots, the optical properties of the pure NP do not depend on field direction, and the lines in subpanels (iii) are superimposed. In subpanels (i) and (ii), different lines correspond to different NC volume fractions, as follows: solid black – A/1250 (1.7%vol), dotted red – A/740 (2.9%vol), dashed blue – A/536 (4.0%vol) and dot-dashed green – A/416 (5.1%vol). Horizontal solid orange lines represent the pure amorphous PVDF polymer. Where the orange line is not visible, it coincides with the graph's abscissa.

The ϵ_2 spectrum of the pure polymer had no intensity within 7 eV of the Fermi energy, because of its large band gap. The spectrum of the pure NP was independent of excitation direction (subpanels (iii) of Figures 3.3–3.4). Although highly symmetrical, the Ag_{13} cuboctahedral NP has an aspect ratio (z/x) of 0.81, so the isotropy of its spectrum is somewhat surprising. Of all the NPs investigated, only A, B and G showed isotropic spectra.

When NP A was incorporated into matrix material, low-energy absorption peaks broadened and slightly blue-shifted, while the high-energy peak remained relatively unchanged (see Figure 3.3(a)). However, the NC spectra showed some dependence on polarization direction. The two polarized fields along the x- and z-axes had changes in peak intensities, both in overall magnitude, and in relative peak heights. These small differences were attributed to a combination of small changes of the lattice constant of the simulation cell in the two dimensions, and variations in polymer packing around the inclusion as hydrogen and fluorine atoms were physisorbed at different sites on the NP. The effect was observed for a second A/416 NC system that was constructed with different polymer packing around the inclusion. Experimental spectra would likely consist of an average over the various packing arrangements in different parts of the bulk NC.

Higher volume fractions of the metallic NP led to stronger absorption peaks, and sometimes to changes in peak positions and structures. Increased absorption strengths with loading have indeed been reported experimentally for Ag/PVDF NCs, [195] and are related to increases in conductivity, as would be expected for metallic inclusions. In terms of excitations, as the volume fraction increased, relatively larger numbers of NP states became available in the band gap, which led to larger absorption probabilities. Changes in absorption energies were due to the slight repositioning of E_F (and thus of the relative location of the polymer conduction levels) when the volume fraction changed (see e.g. Figure 3.1(c) and (d)).

Additional optical constants (ϵ_1, α and R) are shown in Figures 3.3(b) and 3.4. The complex refractive index and conductivity are omitted due to their similarities to the complex dielectric constant and absorption coefficient, respectively, as depicted in Figure 3.2. In general, larger NP volume fractions led to stronger optical response of the material, with the exception of α and σ which were largely independent of volume fraction.

PVDF was found to have a constant ϵ_1 value of about 2.1 over the studied optical range (see Figure 3.3(b)), unchanging as a result of the absence of any interband transitions. Small volume fractions (up to 5%vol) of Ag NPs were seen to increase

the low energy dielectric constant up to about 3, and interband transitions between 2 and 3 eV cause ϵ_1 values to approach 8.

The absorption coefficient (α, see Figure 3.4(a)) and conductivity (not shown) of the polymer were modified significantly by incorporation of the inclusions. The polymer is transparent to light propagation and does not conduct electricity in this range. The spectrum of the NC is very similar to that of the NP for photon energies above 1.6 eV. Below this threshold, however, α_{NC} and σ_{NC} exhibit features specific to the complex material. Very small NP absorption strengths in this excitation energy range are present in Figure 3.3(a). These cause increased electrical conductivity that is somewhat amplified and broadened in the NC, and lead to significant extinction of the incident wave.

As shown in Figure 3.4(d), the NC could be made partially reflective (up to 40%) to normal incident radiation for certain photon energies, whereas the bare polymer was not reflective at all.

3.3 Effect of NP Shape and Size on NC Optical Response

Most of the NPs studied exhibited absorption strengths that changed depending on the incident field direction (NPs C–F, H and I in Figure 2.1). Plots showing the influence of loading on ϵ_2 of the NP and corresponding NCs are presented in Figures 3.5 for NPs C–F and 3.6 for NPs H and I. (Additional optical spectra of these NPs are presented in Appendix B.) Although these plots are difficult to trace back to wavefunction shapes because of the complex DOS in these systems, the directionality dependence likely arises via distinct geometrical shapes of the molecular orbitals involved in the relevant electronic transitions. Overall, absorption peaks were blue-shifted in the direction in which the NP size was smaller, as expected from basic quantum confinement models such as particle in a box.

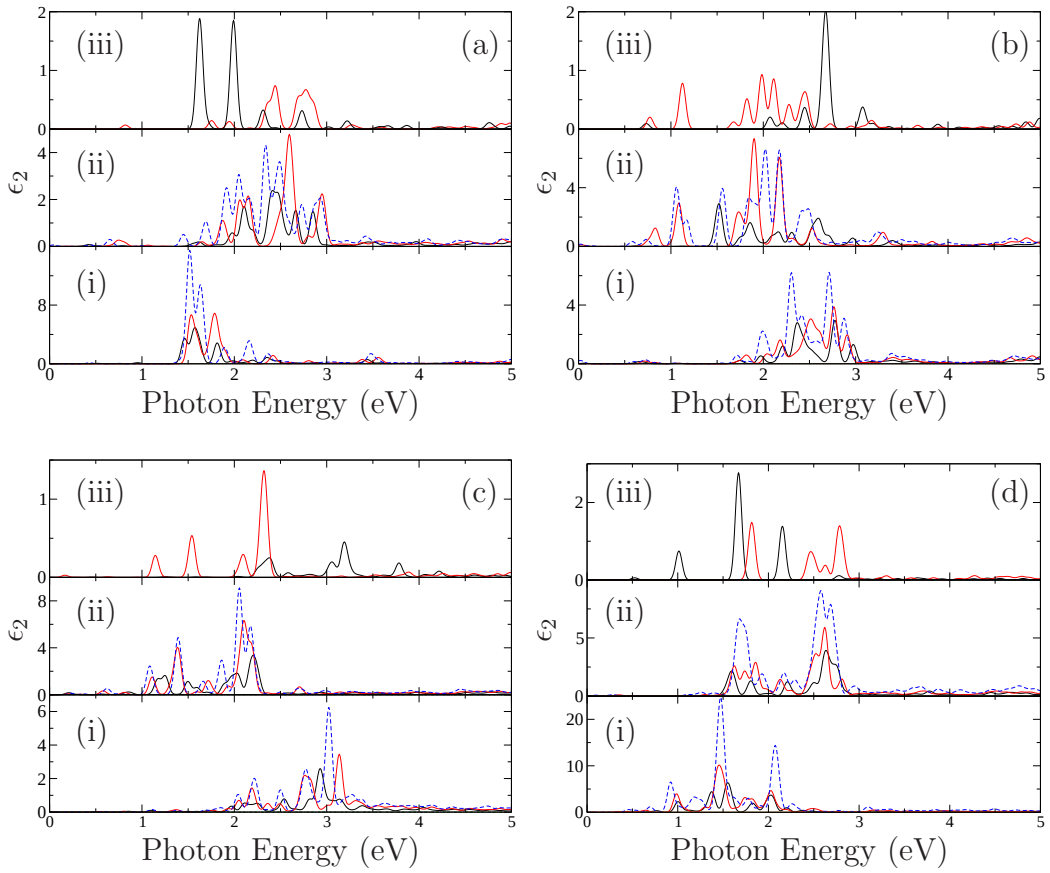

Figure 3.5: Influence of volume fraction and crystalline NP size and shape on the imaginary dielectric constant (ϵ_2) of Ag/PVDF NCs. NCs with NPs C–F (Fig. 2.1) are represented in panels (a)–(d), respectively. In each graph, subpanels (i) and (ii) report optical properties of NCs with incident fields polarized along the z- and x-axes of the NP, respectively. Subpanel (iii) presents ϵ_2 of the NP in vacuum, with incident fields along the z-axis (black line) and along x (solid red line). In subpanels (i) and (ii), different lines correspond to different NC volume fractions. Loading increases from: solid black, solid red to dashed blue. Exact volume fractions for NCs are given in Table 3.1.

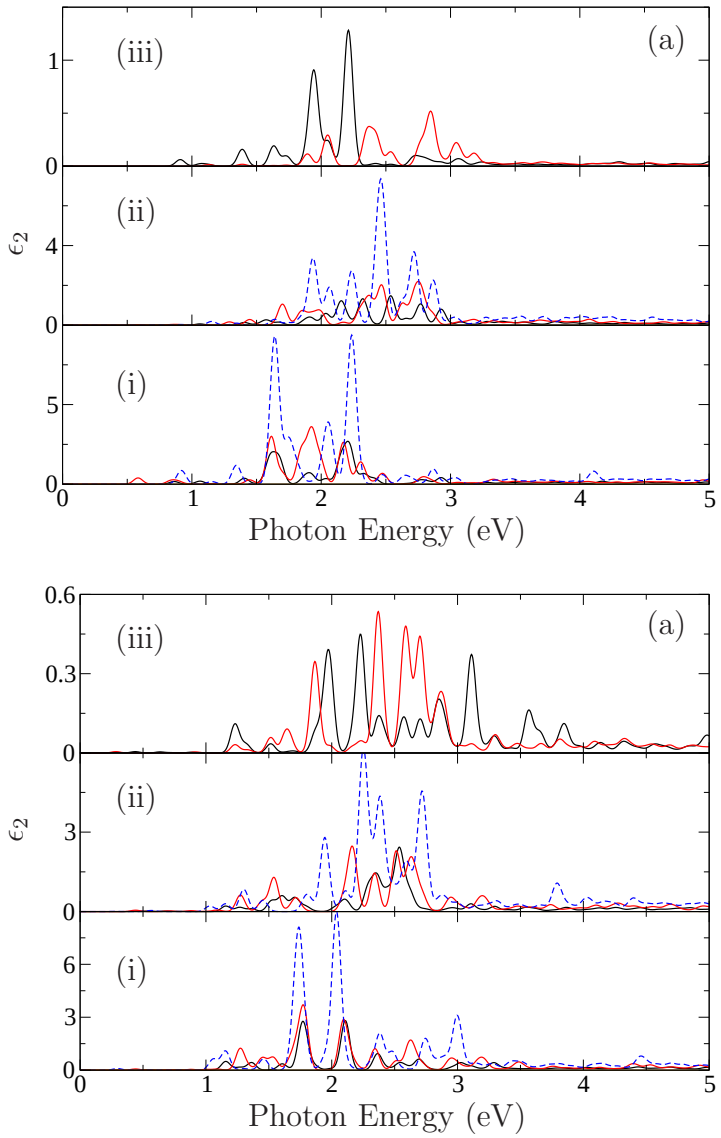

Figure 3.6: Influence of volume fraction and amorphous NP size and shape on the imaginary dielectric constant (ϵ_2) of Ag/PVDF NCs. NCs with NPs H and I (Fig. 2.1) are represented in panels (a) and (b), respectively. In each graph, subpanels (i) and (ii) report ϵ_2 of NCs with incident fields polarized along the z- and x-axes of the NP, respectively. Subpanel (iii) presents ϵ_2 of the NP in vacuum, with incident fields along the z-axis (black line) and along x (solid red line). In subpanels (i) and (ii), different lines correspond to different NC volume fractions. Loading increases from: solid black, solid red to dashed blue. Exact volume fractions for NCs are given in Table 3.1.

Table 3.1: Legend for Figures 3.5 and 3.6, listing polymer chain lengths and %vol of NC systems with their respective line colours.

Figure	System	Line Colour/Type
3.5	C/1250 (2.0%vol)	solid black
3.5	C/836 (3.0%vol)	solid red
3.5	C/536 (4.6%vol)	dashed blue
3.5	D/1250 (2.3%vol)	solid black
3.5	D/836 (3.4%vol)	solid red
3.5	D/536 (5.1%vol)	dashed blue
3.5	E/1250 (2.0%vol)	solid black
3.5	E/836 (3.0%vol)	solid red
3.5	E/590 (4.2%vol)	dashed blue
3.5	F/1250 (2.9%vol)	solid black
3.5	F/836 (4.3%vol)	solid red
3.5	F/416 (8.3%vol)	dashed blue
3.6	H/1250 (1.6%vol)	solid black
3.6	H/836 (2.4%vol)	solid red
3.6	H/416 (4.7%vol)	dashed blue
3.6	I/1250 (1.7%vol)	solid black
3.6	I/836 (2.6%vol)	solid red
3.6	I/416 (5.1%vol)	dashed blue

The polarization-dependent trends were maintained in the NCs. Slight red-shifts and additional structure were observed in the absorption spectra as the NP was placed in the matrix material. Significant enhancement of absorption strengths was achieved with higher NP loading in all systems.

Figure 3.6 presents the absorption spectrum of the amorphous Ag_{12} and Ag_{13}, (NPs H and I), and their NCs. The graphs illustrate the importance of NP crystallinity to localization of excitation peaks: although the polymer itself was amorphous, absorption peaks of the NCs were localized roughly as much as those of the respective NPs. In the case illustrated in Figure 3.6, the NP itself was amorphous, absorption bands became broad, and the specificity of absorption was lost.

Clearly, for the ideal monodisperse systems discussed here, changing the particle size and shape allowed tuning of optical properties, while significant dependence on applied field directions indicates applicability for optical switches. Real experimental systems, however, are often not monodisperse, and bulk optical properties become averages over the various NP shapes and orientations. A simple polydispersity model and its impact on theoretical optical response in these systems is discussed below.

3.4 Polydispersity

A system was designed with two different NPs within a large unit cell. Inclusions A and C were placed roughly along a [111] diagonal of the unit cell, with a 1094-atom long PVDF segment. Inclusion orientations were kept as in Figure 2.1. The optical response of the AC/1094 composite is compared in Figure 3.7 with those of NCs based on the constituent inclusions, as well as with the properties of a NC based on a single 28-atom inclusion (NP G in Figure 2.1). The dependence of the absorption spectrum on the polarization direction is also shown in the figure.

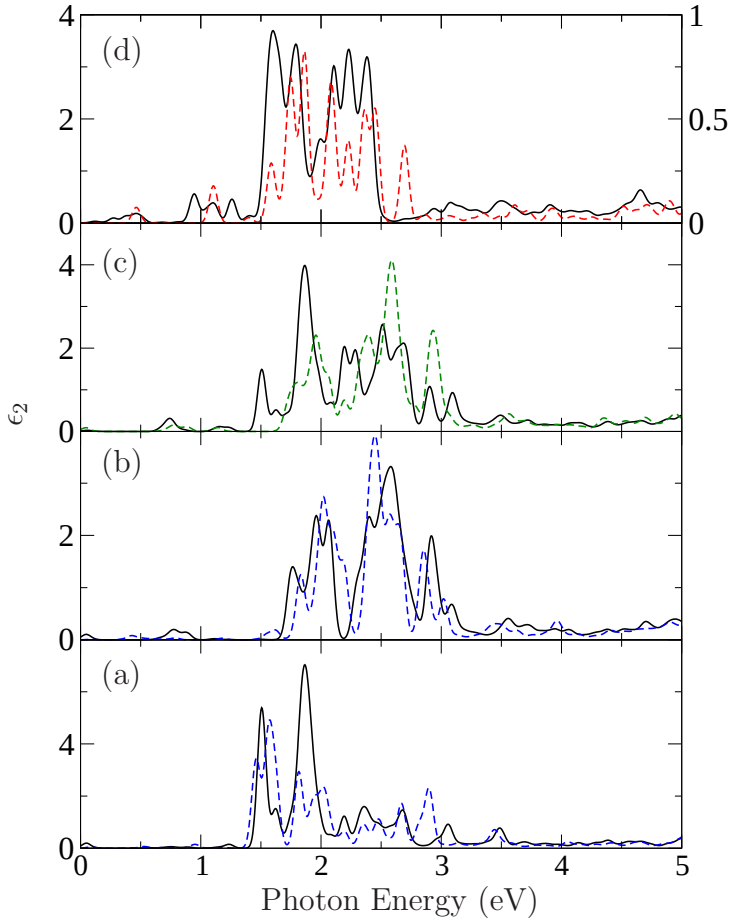

Figure 3.7: Influence of polydispersity and incident field polarization on the imaginary dielectric constant (ϵ_2) of Ag/PVDF NCs. Panels (a) and (b) compare ϵ_2 of AC/1094 (4.2%vol) NC (solid black line) with the sum of ϵ_2 from the monodisperse systems A/1250 (1.7%vol) and C/1250 (2.0%vol) (dashed red lines) with incident fields polarized along the (a) z-axis and (b) x-axis. Panel (c) shows ϵ_2 from incident fields polarized along [111], in line with both inclusions (solid black line), and $[1\bar{1}0]$, a perpendicular direction (dashed green line). Panel (d) shows ϵ_2 from incident field polarized along the x-axis for G/1094 (4.2%vol) (solid black line) and G in vacuum (dashed red line), with ordinate scales along left and right sides, respectively.

From the point of view of NP loading, the polydisperse system can be roughly thought of as a mixture of NCs A/547 and C/547. Comparisons of the AC/1094 optical spectrum with the sum of the monodisperse A and C NCs with similar volume fractions showed more intensity in the sum spectrum than in the polydisperse spectrum. Instead, as shown in Figure 3.7(a) and (b) for the z and x polarization directions, the polydisperse spectrum was very similar to the sum spectrum of the A and C NCs at about half loading. Examination of the interparticle spacings in these systems points to the reason behind this somewhat unexpected observation: edge to edge interparticle spacing in AC/1094 was about 16 Å between PBC image NPs, similar to the ≈15 Å PBC interparticle spacing in both the A/1250 and C/1250 NCs. For comparison, the edge-to-edge interparticle spacing in A/536 is about 9 Å. The data therefore suggests that the intensity of the optical response of the material is better correlated with interparticle spacings along the polarization direction, than with loading (although loading itself significantly impacts the absorption intensity). Figure 3.8 presents a snapshot of the polydisperse simulation cell.

To examine the impact of NP dispersion at constant loading, we evaluated the optical properties of high symmetry Ag_{28} NC (G/1094). The absorption spectrum of G/1094 is presented in Figure 3.7(d). The plot shows broad absorption peaks along a relatively narrow excitation energy interval, very different from the more structured peaks, throughout a larger excitation energy range, exhibited by the polydisperse spectrum. This is well correlated to the DOS of the two systems (see Figure 3.9), which shows more band-like structure, with broader peaks at lower energies, for G/1094, than for AC/1094, and consistent with quantum confinement energy shifts. Figure 3.8 presents a snapshot of a polydisperse simulation cell.

A final point examined in relation to polydispersity is the dependence on the polarization (or incident field) direction. Figures 3.7(b) and (c) show the absorption spectrum of AC/1094 along z and x, respectively. The blue shift of the x-polarized spectrum is consistent with quantum confinement for NP C, as discussed in some length in relation to Figure 3.5. The other type of inclusion, NP A, exhibited no polarization dependence in its vacuum spectrum (Figures 3.3 and 3.4). The directional dependence in the polydisperse system, however, is more complex than just along the replication directions of the PBCs: the inclusions are placed along a unit cell diagonal, thus this polarization direction will exhibit distinct periodicity with the two inclusions alternating. Figure 3.7(c) describes these new polarization directions, along the unit cell diagonal that includes the two NPs (direction [111]) and also along a perpendicular direction ($[1\bar{1}0]$). When the two NPs alternate in the polarization

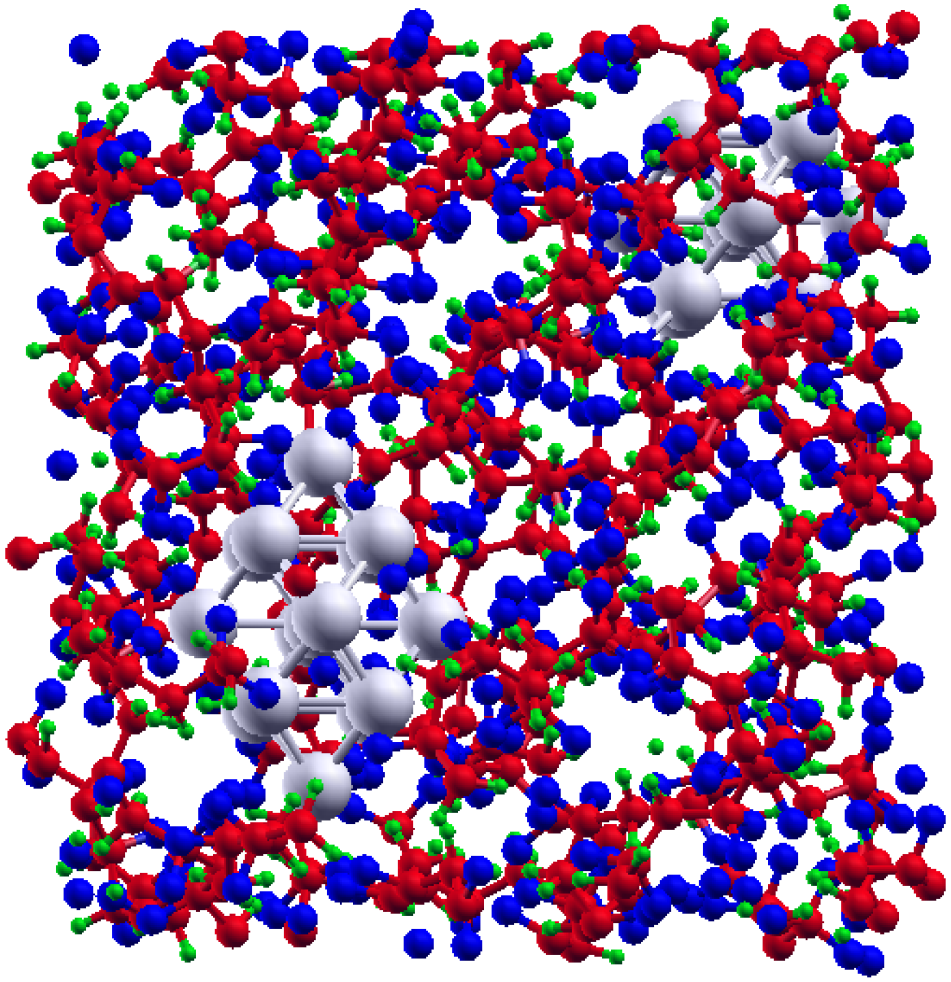

Figure 3.8: Snapshot of a simulation cell with PBC with 1094 PVDF atoms and both 15 and 13 atom Ag NPs (AC/1094). NPs are positioned at opposite vertices of the cell. For clarity, silver atoms are grey, fluorine is blue, carbon is red, and hydrogen is green. z-axis runs approximately from top to bottom of page and x-axis runs from left to right of page. Cell is tilted slightly to show three-dimensionality.

direction, the resulting spectrum is an average of the x and z polarization directions. When the field is applied along the perpendicular direction $[1\bar{1}0]$, the x-polarization spectrum is mostly found. Both results correlate well with the directionality of the fields in relation to the anisotropic inclusion C: field lines along [111] make about a 55° angle with the long axis of the NP, while field lines along $[1\bar{1}0]$ are in the xy plane and thus along the short NP axis.

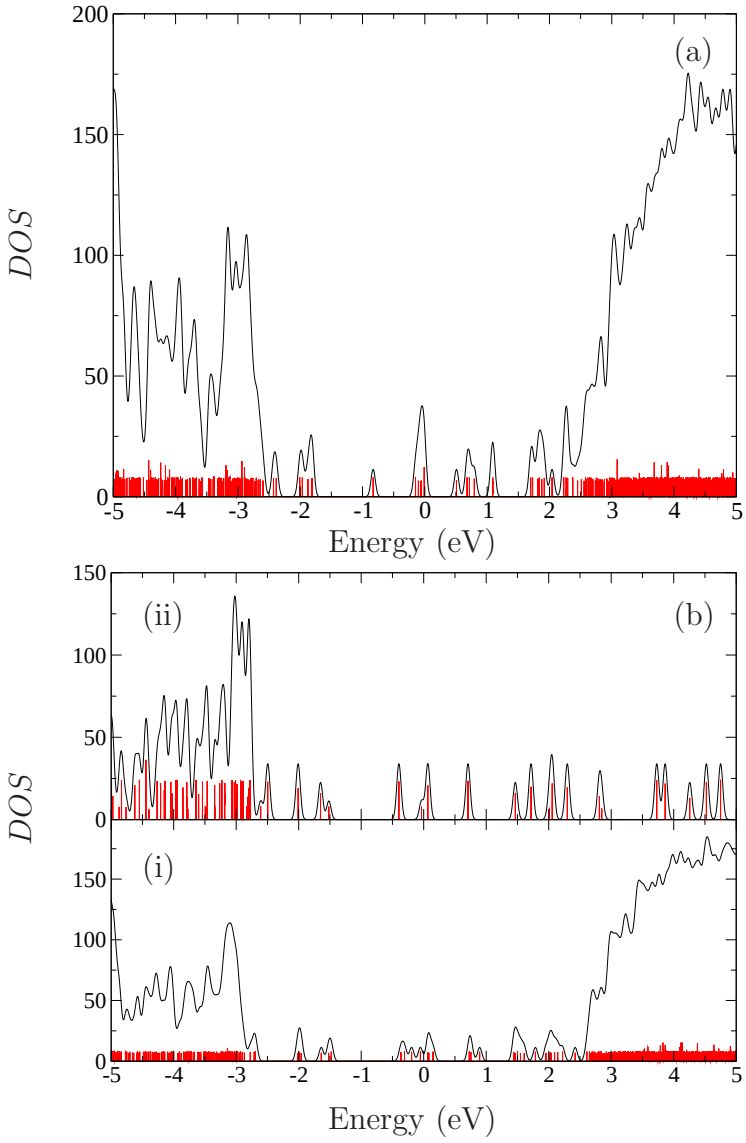

Figure 3.9: Influence of polydispersity on the density of states (DOS) of Ag/PVDF NC. Panel (a) presents the DOS of polydisperse AC/1094. Panel (b) presents the DOS of (i) G/1094 and (ii) NP G. The zero on the Energy axis is set at the Fermi energy. Black lines show a Gaussian energy broadening of 0.05 eV, and the red lines illustrate the location of states with a finer broadening of 0.001 eV.

3.5 Summary

The presence of small volume fractions of Ag NPs in PVDF significantly altered the electronic band structure and density of states. A wide range of optical properties are affected, which can be modified by the volume fraction and NP shape. Monodisperse systems are important in producing unique optical spectra from the NP: polydisperse spectra are superpositions of the monodisperse systems. The following chapter examines the role of Ag nanodisk and nanorod structures in PVDF.

Chapter 4

Results and Discussion: Nanoparticle Morphology and Aspect Ratio Effects

This chapter presents and discusses results from Ag/PVDF NCs with rod and disk-shaped inclusions. The influence of nanodisk and nanorod aspect ratio on ϵ_2 is investigated. Nanodisk inclusions are constructed with either {111} or {100} basal planes, and the effect of crystallographic projections on the optical spectra are examined. Lastly, the influence of structural changes to nanorod termini are discussed.

Electronic structures of NPs are clearly determined by the cluster's stability, even away from the ultra-stable magic number clusters that are due to electronic shell closings within the nanostructure. [120, 154, 162, 196–198] The binding energies of the various NP structures quantify their relative stability (see Equation 2.22 and Figure 4.1), and are used to examine its effect on optical spectra in the following sections. From the figure, and as confirmed by previous theoretical calculations, [197, 199, 200] larger clusters were overall more stable. The presence of {111} basal planes also led to tighter binding in both disk and rod-shaped NPs, in a trend that was expected from crystal plane surface energies. Not unexpectedly, given their small sizes, all of the NPs considered here exhibit strong finite size effects. For comparison, the PBE/DZP binding energy for bulk Ag was 5.03 eV.

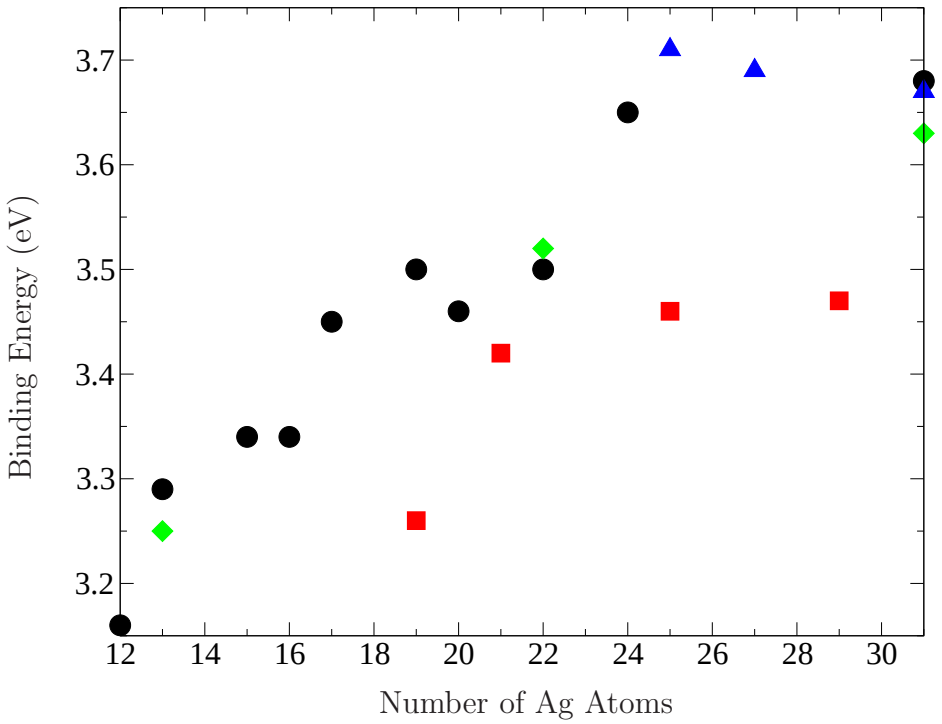

Figure 4.1: Influence of NP aspect ratio, shape and basal plane structure on binding energy. Black circles – {111} disks (NPs E, J–R). Red squares – {100} disks (NPs S–V). Green diamonds – {100} rods (NPs A, F and W). Blue triangles – {111} rods (NPs X–Z).

4.1 Nanodisk Aspect Ratio Effects

Disk-shaped inclusions consisted of two layers of Ag atoms, with surfaces in the {111} or {100} planes. A sample NC simulation cell with NP V is shown in Figure 4.2. Changes in the horizontal size of these atomic layers led simultaneously to changes in cluster size, aspect ratio and horizontal interparticle distance in the corresponding NCs. Spectra for normal and transverse excitations for NCs of three {111} facet disks are presented in Figure 4.3, and their DOS plots for the relevant NPs and NCs in Figure 4.4. (Absorption spectra and DOS plots for additional {111} facet nanodisks and NCs are provided in Appendix B.) As expected from confinement models, absorption for both the NPs and their NCs occurred at higher energies for excitations along the shorter normal direction (Figure 4.3(a)), than along the longer transverse direction (panel (b)).

A pervasive feature in the disk-based NC spectra was that the high-energy absorption peaks of the inclusions were shifted to lower energies and broadened in the NCs. This is due to a combination of two effects: firstly, the conduction bands originating from the pure matrix become involved in electronic transitions at these higher photon

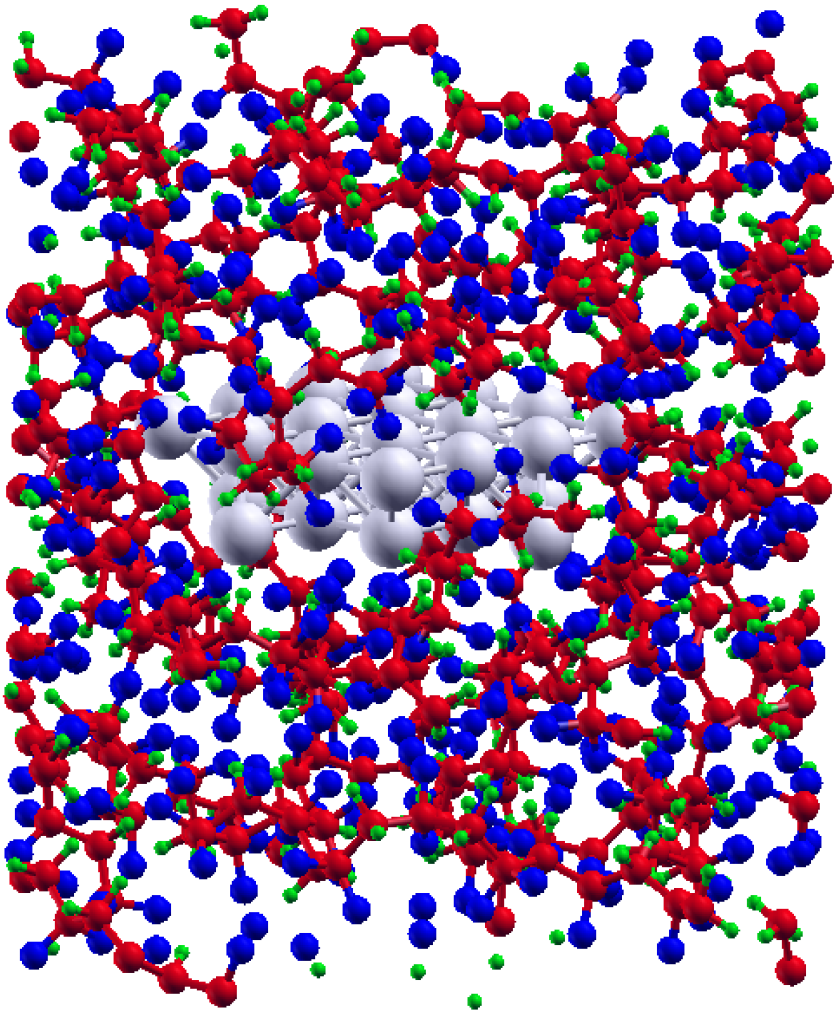

Figure 4.2: Snapshot of a simulation cell with PBC with 1130 PVDF atoms and 29 atom nanodisk (V/1130). For clarity, silver atoms are grey, fluorine is blue, carbon is red, and hydrogen is green. z-axis runs approximately from top to bottom of page and x-axis from left to right of page – cell is tilted slightly to show three-dimensionality.

energies; and secondly, high-energy NP virtual states are broadened in the NC due to interaction with the matrix conduction band. Both effects can be seen, for example, by comparison of the NP and NC DOS plots in Figures 4.4(a) and (b), respectively, in the 2-4 eV range.

Overall, as nanodisk size increased, NP and NC spectra broadened for {111} clusters, regardless of polarization direction. NCs with 12-15 atom inclusions (NPs J,K and E) had few, discrete absorption peaks (see Figure 4.3a(i)). Increasing NP size caused first coalescence of peaks, (as, for example, in N/740 – Figure 4.3a(ii)); then, for the larger inclusions considered here, an overall extension of the absorption energy range (see, for example, the spectrum of O/782 – Figure 4.3a(iii)). These

spectral changes generally arose due to the broadening of wavefunction bands in the DOS plots with increasing particle sizes. A small red-shift of the absorption spectrum with increasing inclusion size was observed for NCs polarized along the x direction (Figure 4.3(b)), in agreement with experiments [201] and discrete dipole approximation simulations. [160] Low energy peaks also appeared in the spectra of some of the larger NPs and their NCs, when a few electronic wavefunctions with similar energies formed small bands in the vicinity of the Fermi energy and upwards of about 1 eV. This was the case for NCs O/782 (subpanels (iii) in Figure 4.3b and Figure 4.4c and d), P/860 and Q/938, and, to a lesser extent, D/626. The spectral location of the absorption of z-polarized light was independent of inclusion sizes (Figure 4.3a).

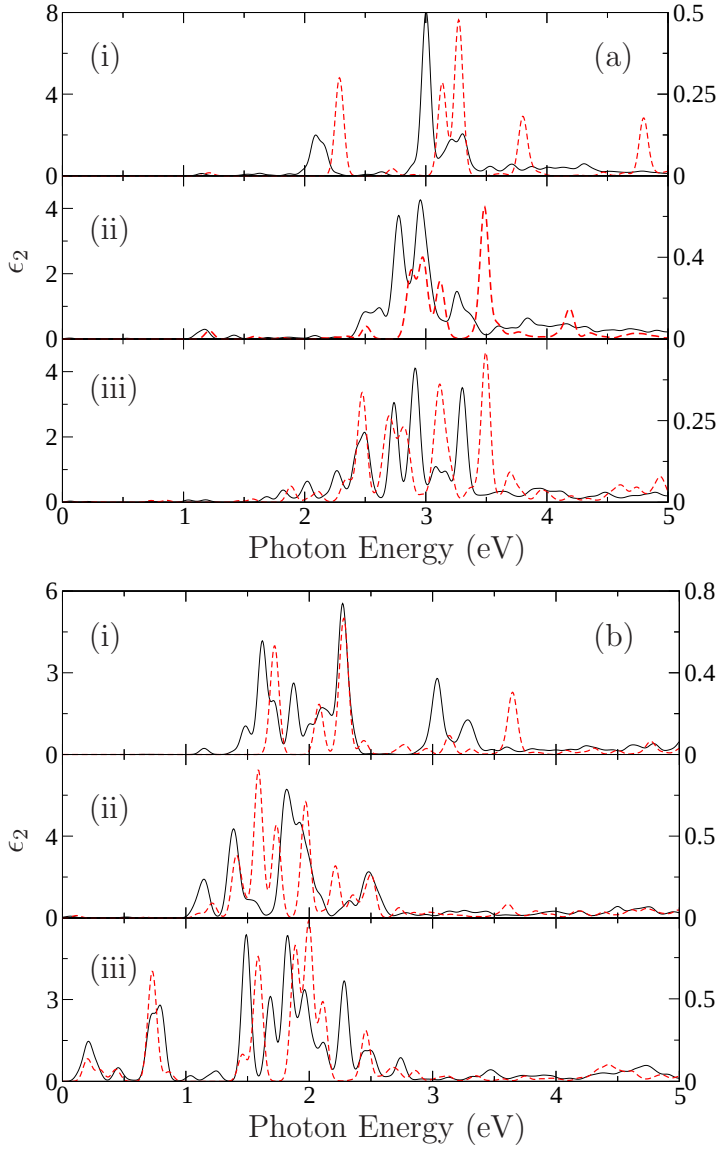

Figure 4.3: Optical response for NCs with disk-shaped inclusions from {111} basal planes. Normal and transverse polarization for the NPs and NCs are shown in panels (a) and (b), respectively. Solid black lines are from NCs and dashed red are from NPs in vacuum, with ordinate scales along left and right sides, respectively. Subpanels (i)–(iii) present NCs J/470, N/740 and O/782, respectively.

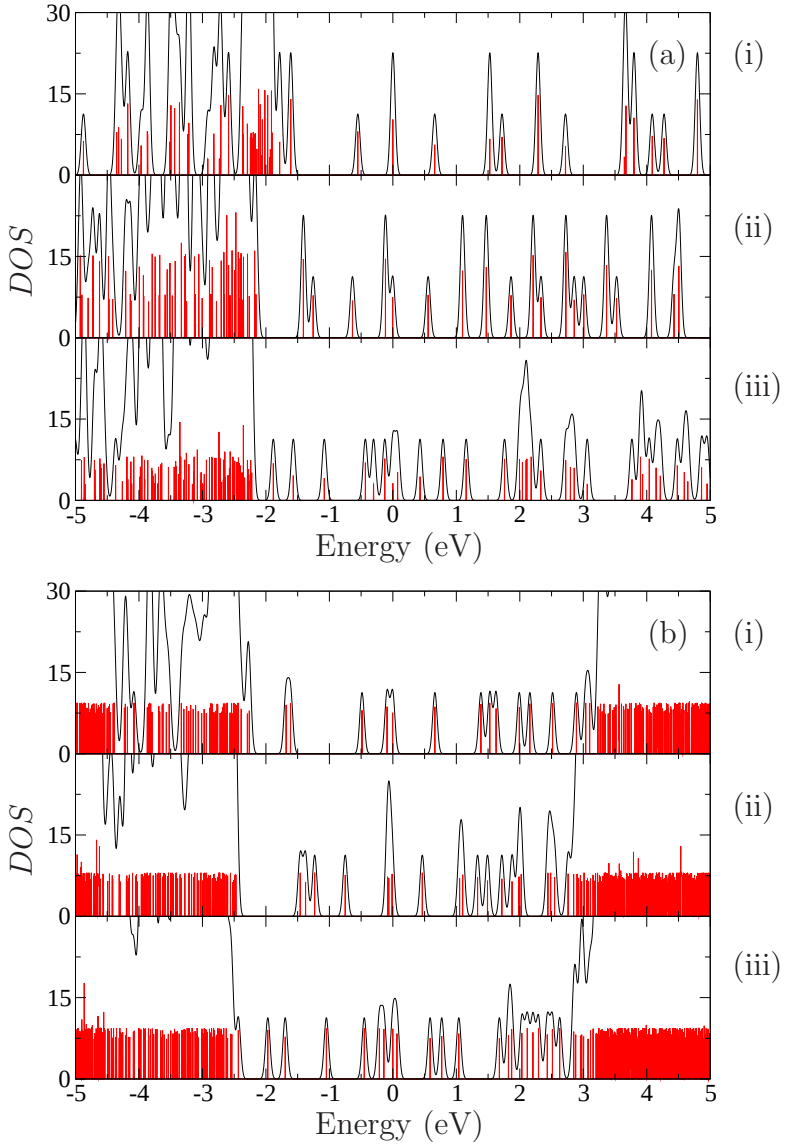

Figure 4.4: Density of states (DOS) plots for NCs with disk-shaped inclusions from {111} basal planes. Panel (a) presents DOS for NPs J, N and O in subpanels (i)–(iii), respectively. Panel (b) presents DOS for NCs J/470, N/740 and O/782, respectively. Curves for Gaussian energy broadening of 0.05 eV (black lines) and 0.001 eV (red lines) are shown.

4.2 Nanodisk Crystal Facet Effects

The crystallographic profile of NP basal planes impacted NC absorption spectra in a number of ways. Figure 4.5 shows ϵ_2 for three {100} nanodisks (NPs S, T and U) and their NCs, from normal and transverse field polarizations (panels (a) and (b), respectively). Figure 4.6 shows DOS plots for the NPs and their NCs (panels (a) and (b), respectively). (Appendix B includes ϵ_2 and DOS plots of NP U and U/980.) First, spectra of these less stable {100} disk NPs and their NCs were broadened relative to their {111} counterparts. {100} disk spectra were also slightly blue-shifted in normal fields, and red-shifted in transverse fields. The former shifts are likely due to the slightly smaller height of these disks (see Table 2.1), while the latter can be attributed to the reduced stability of the {100} disk NPs, and correspondingly lower HOMO-LUMO gap. The gap difference is clearly observed by comparing the NC DOS in Figures 4.4 and 4.6.

The spectral broadening in NCs based on {100} inclusions correlated well with the extent of polymer involvement in the optical response of the material: high-energy NC spectra for normal polarization were broadened as the matrix conduction band participated in these transitions (for example, NCs S/740 and T/818 in Figure 4.5a(i) and (ii)). In fact, examination of the spectral behaviour of NCs based on {111} and {100} facet disks provides the best support to the suggested mechanism for matrix-inclusion interactions in these systems, through a contrasting case: that of U/980. This system exhibits, in normal polarizations, an ϵ_2 spectrum very similar to that of the vacuum inclusion (see Figure 4.5a(iii)). A comparison of DOS plots for the NP and the NC, given in Figure 4.6a(iii) and b(iii), respectively, reveals a peculiarity in the high-energy region. High degeneracy below the Fermi energy in NP U led to a low Fermi energy in the NC, and thus a relatively high location of the matrix-based conduction band. Orbitals involved in transitions up to and over 3.5 eV in this system belong largely to the NP, thus the similarity of the two spectra.

A further example showing the importance of crystallographic projections in NP and NC absorption spectra is provided from NPs N and S. They have the same number of atoms, nearly equal aspect ratios and interparticle distances between PBC images (see Table 2.1), but differ in their surface structure. Prominently, NP N with {111} surfaces exhibits a narrower range of transitions from both x and z polarized fields (subpanels (ii) in Figure 4.3(a) and (b)) than NP S with {100} surfaces (subpanels (i) in Figure 4.5(a) and (b)). The DOS of NP S (Figure 4.6a(i)) shows degenerate states both at the Fermi energy as well as slightly below it. The presence of the matrix acts by splitting these states into a narrow band (Figure 4.6b(i)), which acts

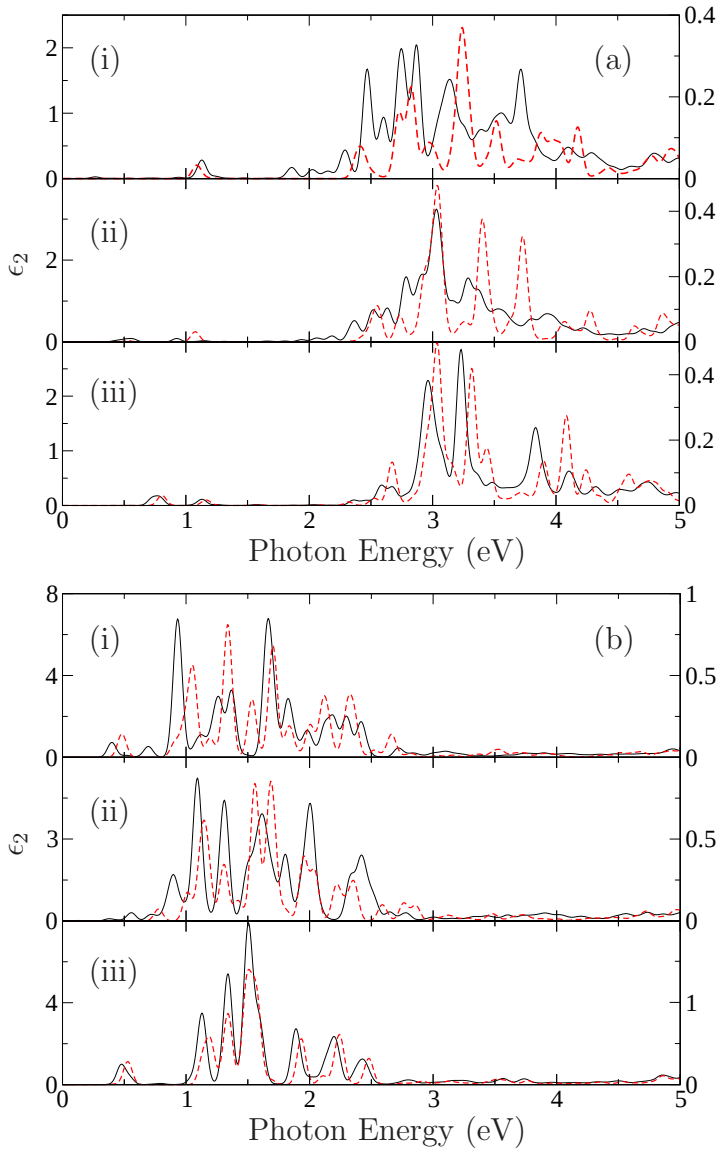

Figure 4.5: Optical response for NCs with disk-shaped inclusions from {100} basal planes. Normal and transverse polarization for the NPs and NCs are shown in panels (a) and (b), respectively. Solid black lines are from NCs and dashed red are from NPs in vacuum, with ordinate scales along left and right sides, respectively. Subpanels (i)–(iii) present NCs S/740, T/818 and U/980, respectively.

by broadening the energetic range of ϵ_2. No such interactions are observed from the DOS of NP N and N/740 (subpanels (ii) in Figure 4.4).

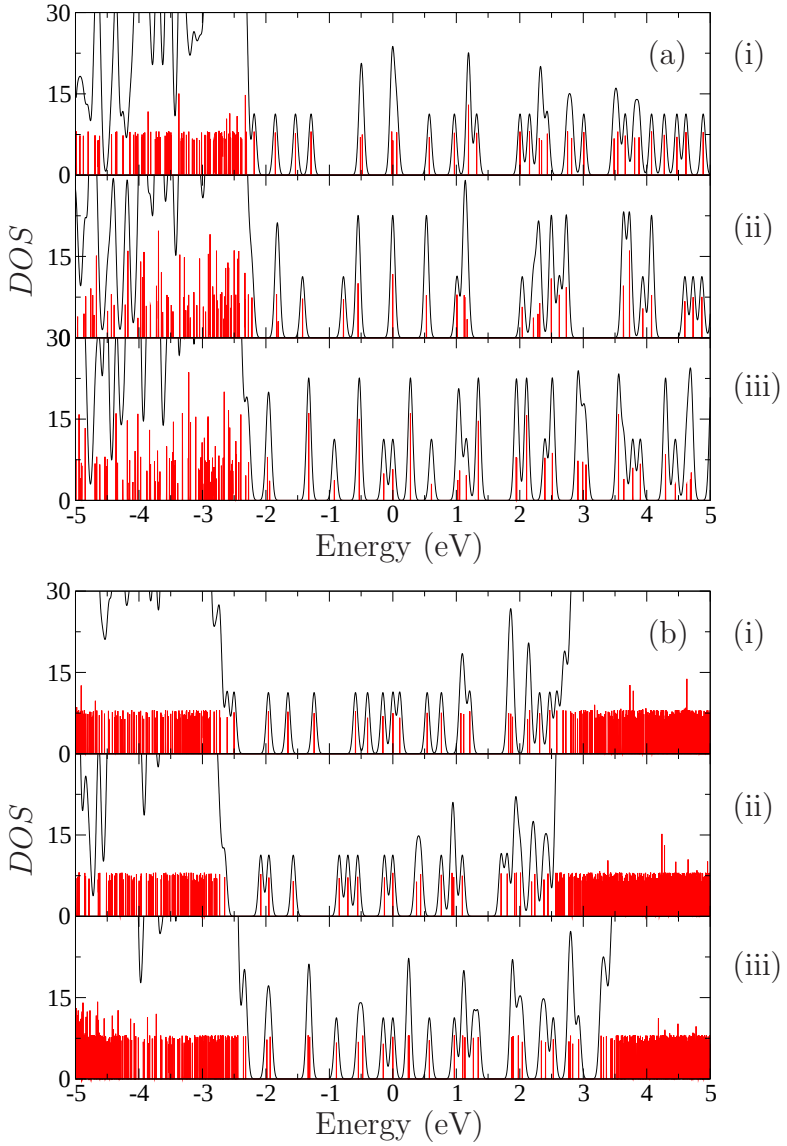

Figure 4.6: Density of states (DOS) plots for NCs with disk-shaped inclusions from {100} basal planes. Panel (a) presents DOS for NPs S, T and U in subpanels (i)–(iii), respectively. Panel (b) presents DOS for NCs S/740, T/818 and U/980, respectively. Curves for Gaussian energy broadening of 0.05 eV (black lines) and 0.001 eV (red lines) are shown.

4.3 Nanorod Aspect Ratio Effects

Nanorod aspect ratio predominantly affects longitudinal polarization response by red-shifting ϵ_2 with increasing nanorod length. The material response from rods (NPs F and W) are compared to that of an almost spherical cluster (NP A) in Figure 4.7. Longitudinal polarization (panel (a)) was found to linearly shift the NP and NC wavelength (or energy) of maximum absorption to lower energy as the nanoparticle increased in length. This quantum confinement effect also agrees with experimental results, [65, 202] and TD-DFT calculations. [203] Moreover, the NP spectral shapes reported here are similar to those reported by others [203], but suggest a scissor operator of $\approx$1.5 eV may be required. These similarities, provided that interband transitions provide a sufficient model of optical absorption, further validate the less computationally intensive time-independent formalism.

Longitudinal excitations in NCs became more intense and more numerous with increasing nanorod length. The integral area under the longitudinal absorption curves between 0–5 eV also increased linearly with both aspect ratio and number of atoms, indicating that more transitions become available with longer nanoparticle length. In contrast, the number of transitions from transverse polarized fields (panel (b)) did not change between the three NCs, because the NP width was constant, in agreement with experimental results. [103]

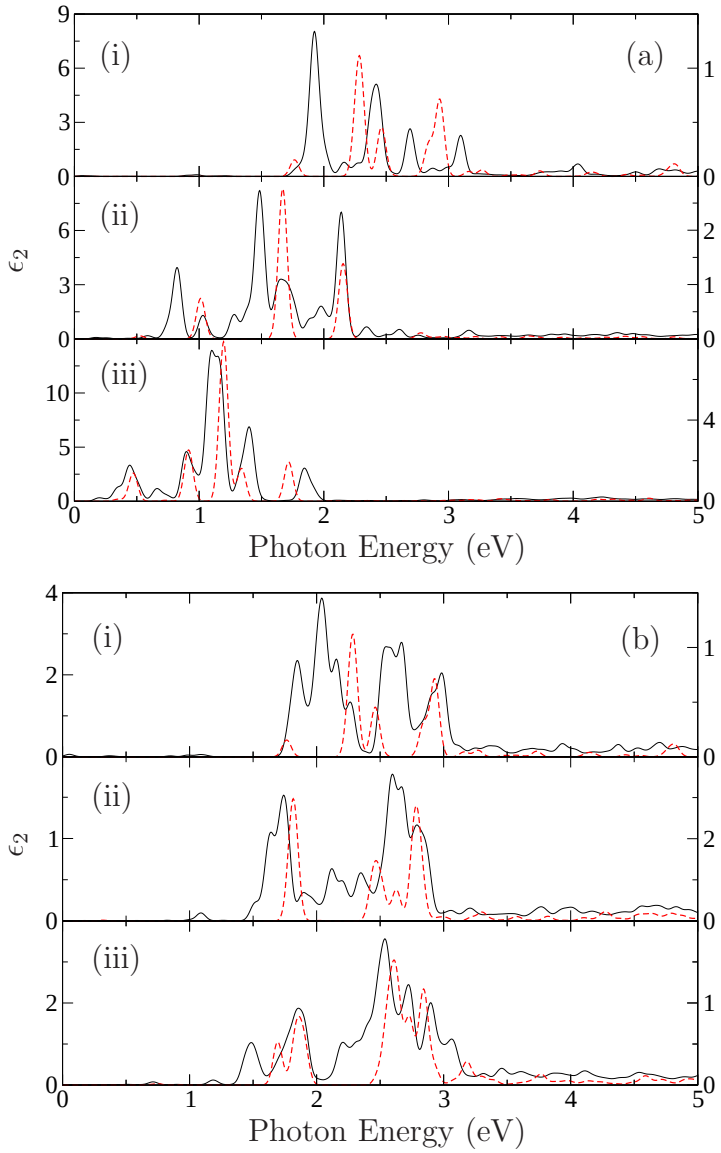

Figure 4.7: Influence of incident field polarization and nanorod aspect ratio on imaginary dielectric constant (ϵ_2) of Ag NPs and NCs. Panels (a) and (b) present optical response from longitudinal and transverse polarization, respectively. Subpanels (i)–(iii) show different NC systems as follows: A/512, F/860 and W/1214, respectively. Solid black is from NC and dashed red is from NP in vacuum, with ordinate scales along left and right sides, respectively.

4.4 Nanorod End-Cap Structural Effects

The end-cap structure of nanorods predominantly affected the range of transitions from the longitudinally polarized absorption spectra. NPs were designed having three different end-caps: trigonal pyramidal with {111} facets (NP X); hemispherical (nanorice structures) (NP Y); and a blunt {111} plane (NP Z). The central region of the rod preserved the same structural features across the three NPs. A simulation cell snapshot of X/1052 is shown in Figure 4.8. Figure 4.9(a) shows the longitudinal absorption spectra, where a narrow transition range from X/1052 (subpanel (i)) is evident. Subpanels (ii) and (iii) show increasingly broader and discrete spectra from Y/980 and Z/1214, respectively. This sequential broadening can be traced back to the DOS of the NPs and NCs (see Figure 4.10). NP X and X/1052 both have a narrow range of occupied states near the Fermi energy (subpanels (i) in panels (a) and (b), respectively). For NPs Y and Z (and NCs Y/980 and Z/1214), states are observed to split off from the Fermi level and move to lower energies (subpanels (ii) and (iii)), thus broadening transition energy ranges.

End-cap structure was also influential on the optical absorption from transverse polarized fields, though to a lesser extent than from longitudinal fields. These transitions occur at higher energies, such that transitions starting near the Fermi energy are placed into states near the polymer conduction band (between 1.5–3.0 eV) shown in the DOS (Figure 4.10). NP states in this range increase in breadth and density from NP Y to X to Z, correlating with the optical absorption ranges exhibited by the NPs and NCs (Figure 4.9(b)). NC spectra follow the same spectral broadening trend as their respective NPs, where a lower energy onset of the polymer conduction band leads to broader spectra.

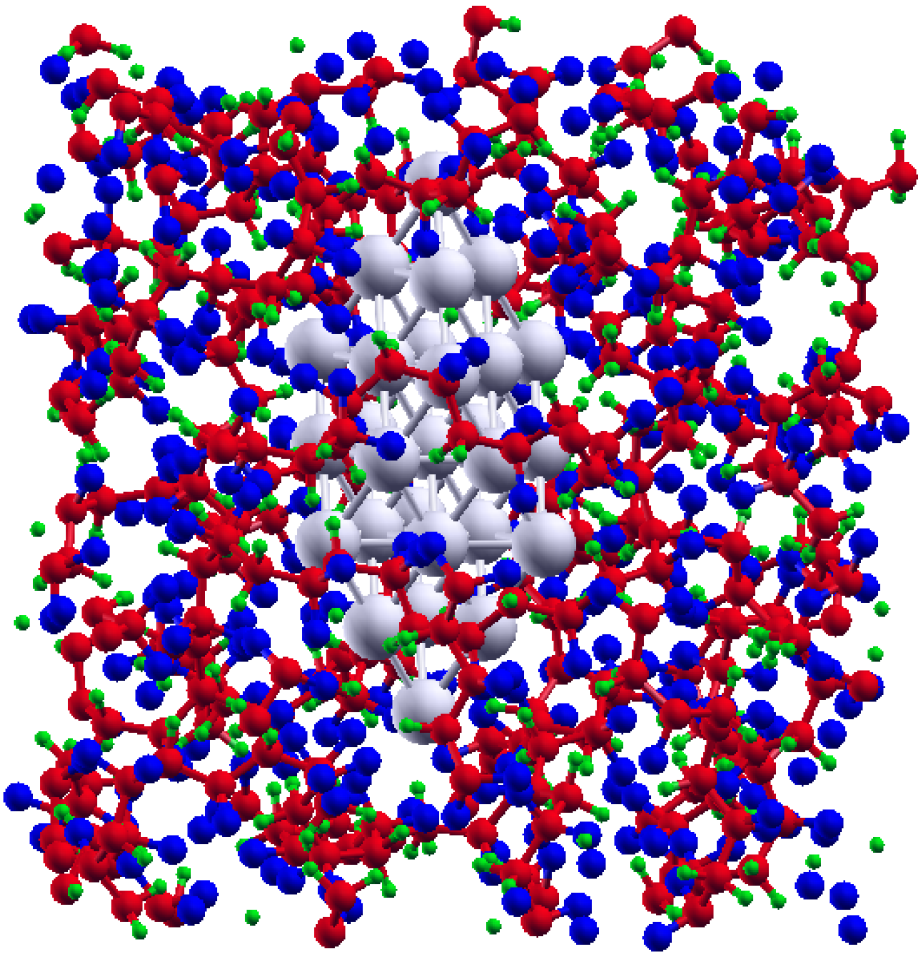

Figure 4.8: Snapshot of a simulation cell with PBC with 1052 PVDF atoms and 27 atom nanorod (X/1052). For clarity, silver atoms are grey, fluorine is blue, carbon is red, and hydrogen is green. x-axis runs approximately from top to bottom of page and x-axis from left to right of page – cell is tilted slightly to show three-dimensionality.

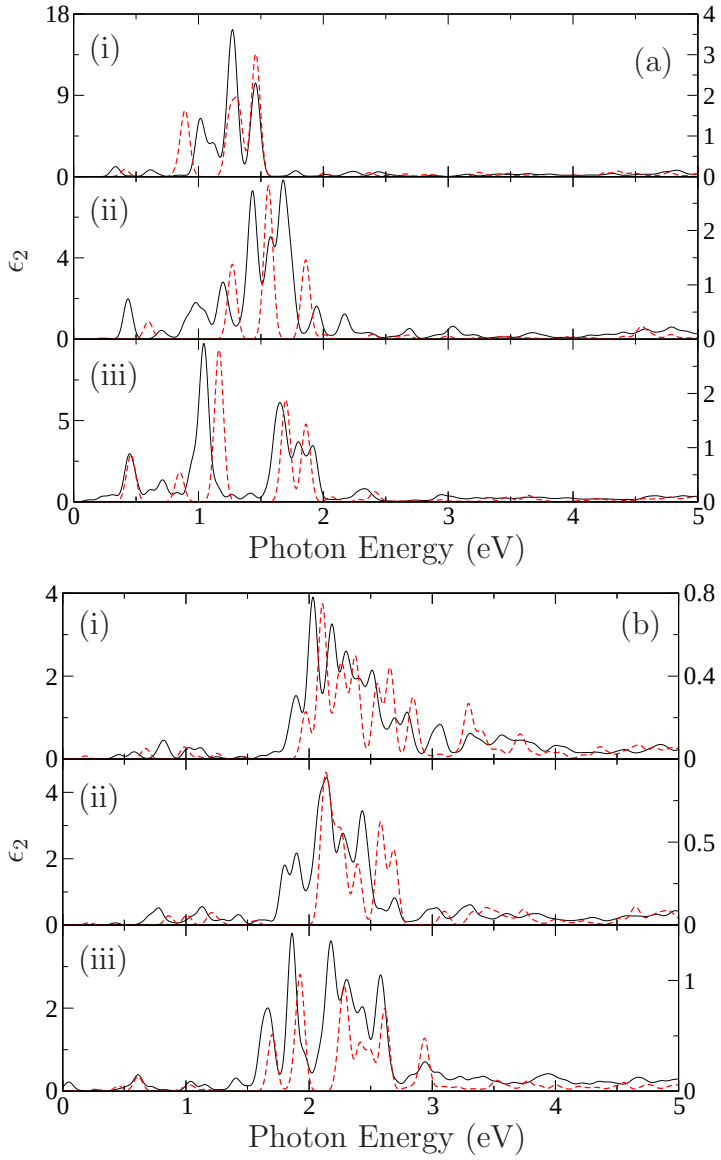

Figure 4.9: Influence of incident field polarization and nanorod end-cap structure on imaginary dielectric constant (ϵ_2) of Ag NPs and NCs. Panels (a) and (b) present optical response from longitudinal and transverse polarization, respectively. Subpanels (i)–(iii) show different NC spectra as follows: X/1052, Y/980 and Z/1214, respectively. Solid black is from NC and dotted red is from NP in vacuum, with ordinate scales along left and right sides, respectively.

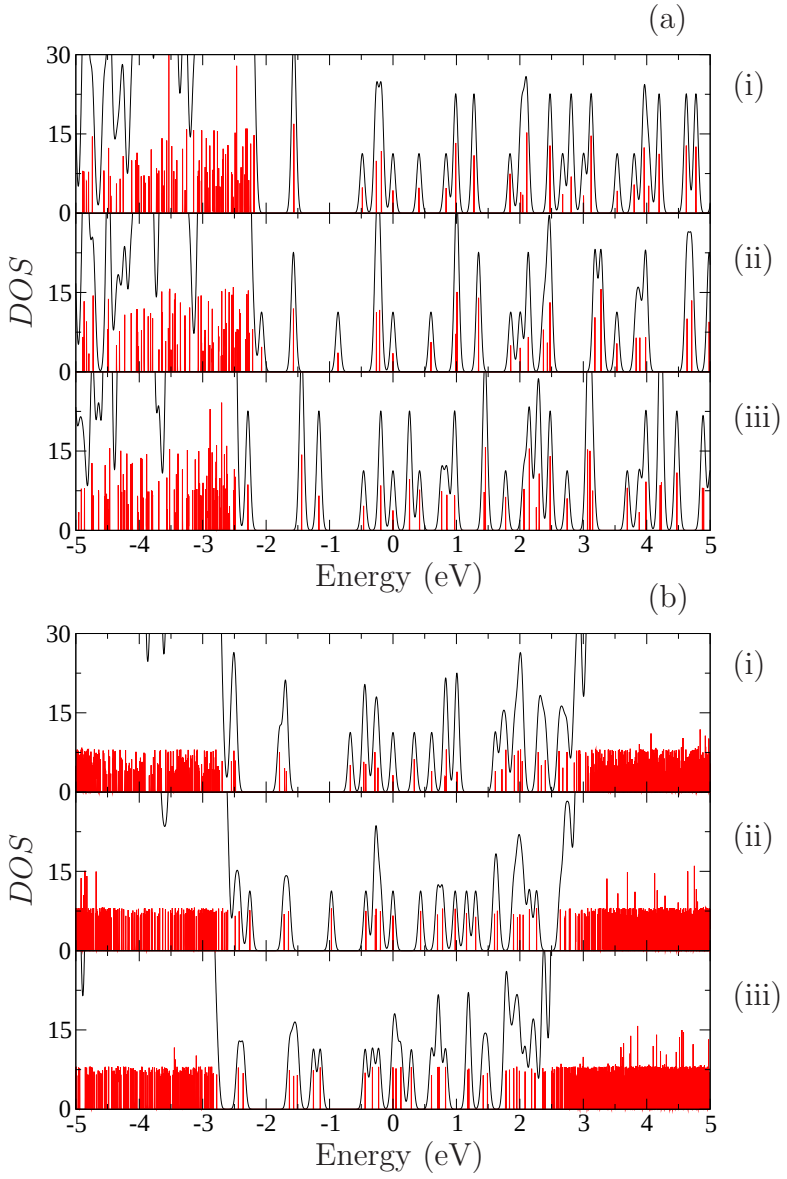

Figure 4.10: Influence of nanorod end-cap morphology on the density of states (DOS) of (a) NPs and (b) their NCs. Subpanels (i)–(iii) present spectra from NPs X, Y and Z, respectively, and their NCs. The zero on the Energy axis is set at the Fermi energy of that particular material. Black lines show a Gaussian energy broadening of 0.05eV, and the red lines illustrate the location of states with a finer broadening of 0.001eV.

4.5 Summary

In summary, NC optical properties can be tuned using nanodisks and nanorods which have different field response properties. Not only does aspect ratio affect the shape and intensity of absorption spectra, but crystallographic planes in nanodisks and the capping morphology in nanorods are also influential.

Chapter 5

Conclusions

Optical properties of model Ag/PVDF nanocomposites were calculated from dipolar interband transitions using the DFT implementation in SIESTA. This is the highest level of theory that is applicable to these types of systems, with simulation cells comprising over a thousand atoms. The resulting properties would be appropriately defined as ideal or theoretical limits, as the methodology assumes monodisperse systems, or systems with limited polydispersity, ignores local field effects and indirect transitions and is only applicable for high-frequency (optical regime) applied fields.

Bulk amorphous PVDF has a large band gap of almost 7 eV. The inclusions placed a large number of levels, and also many electrons, in the band gap. This had the double effect of providing levels for excitations in the optical range where pure PVDF had no response, and of shifting the Fermi energy much closer to the polymer conduction band. In this fashion, although calculations showed very small interactions between the electronic states of the mixed material components, the resulting optical properties were strongly impacted by both.

Photon energy ranges for the NC absorption followed those of the bare NP spectrum. Depending on the relative positions of the conduction band and the Fermi energy in a given NC system, small (about 0.2 eV) red- and blue-shifts were observed for the NC. The presence of the matrix also provided additional structure in the spectrum, while larger volume fractions of the metallic inclusions led to stronger optical response of the bulk material.

For all but three of the NCs studied here, the excitation energies depended on the direction of the applied field. This dependence likely arose from the geometrical features of orbitals involved in transitions, and was particularly significant for crystalline NPs with strong shape anisotropies. This directionality dependence is a feature that is unlikely to be found in experimentally synthesized NCs with strong polydispersities

and uneven NP alignment. However, directionally dependent absorption could have applications in optical switches, similar to those of optical crystals.

A simple polydisperse system with two NPs per unit cell: one a high-symmetry NP and the other an anisotropic NP, provided further insight into the dispersion and directional dependence of NC optical properties. Optical response in the polydisperse NC was significantly different from the monodisperse NC with the same number of Ag atoms per cell. In terms of the effect of polarization direction, optical response correlated well with the interparticle spacing along the applied field, and also with the orientation of the anisotropic inclusion with respect to the field direction.

NC simulations with nanodisks and nanorods were sensitive to the polarization of the incident electric field. Fields directed along the longitudinal axis of nanorod NCs produced absorption spectra (ϵ_2) that red-shifted with increasing aspect ratio. This was also seen in NCs with nanodisks from transverse polarized fields. Although such results from quantum confinement are well-known in the literature, this trend potentially validates the use of interband transition calculations within DFT to model optical properties of certain insulating materials.

Small aspect ratio nanodisks had discrete spectra, while those with larger aspect ratios formed agglomerated energy bands. Such structure could be traced back to the DOS, where larger disks showed increased degeneracy and more states positioned closer together. These energy "bands" broadened for larger NPs as more states became available for population. This is due to a greater number of atoms, resulting in increased atomic coordination. For disks with increasing aspect ratio, absorption peaks were seen to coalesce and subsequently widen from transverse polarized fields. Normal polarized fields were largely unaffected because the thickness did not change across nanodisks with the same crystallographic basal planes. This direction-dependent field response shows a high level of tunability for optical switches.

The importance of NP stability is exemplified in {111} and {100} nanodisk composites. Their spectra are distinct, indicating the importance of atomic packing and coordination. Polarized spectra from normal fields were slightly blue-shifted in {100} basal plane disks compared to {111} disks, due to small differences in disk thickness. The increased stability of {111} surfaces also led to a blue-shifting of transverse fields. Therefore, crystallographic projections are important factors in optical tuning.

In the case of nanorods, increasing aspect ratio linearly red-shifted NC longitudinal absorption spectra, without significantly changing the spectral features. The number of transitions also increased linearly with aspect ratio from longitudinally polarized fields, but was relatively unaffected from transverse polarization. Nanorod

end-cap structure was found to affect the breadth of transitions from both longitudinal and transverse fields. These findings provide further design parameters for optical response features of nanomaterials.

Our findings suggest that DFT is a viable method to model optical property trends in Ag/PVDF NCs. Pervasive throughout this work was the tunability of optical spectra with NP volume fraction, shape, size and polarization of the applied electric field.

Bibliography

[1] Ho, W. K.; Koo, J. H.; Ezekoye, O. A. *J. Nanomaterials* **2010**, *2010*.

[2] Chen, W.; Rajaram, S.; Thomas, S.; Nutt, S. R. *J. Adv. Mater.* **2009**, *41*, 5–17.

[3] Podsiadlo, P.; Liu, Z.; Paterson, D.; Messersmith, P. B.; Kotov, N. A. *Adv. Mater.* **2007**, *19*, 949–955.

[4] Natsuki, T.; Ni, Q.-Q.; Wu, S.-H. *Polym. Eng. Sci.* **2008**, *48*, 1345–1350.

[5] Mohaddespour, A.; Abolghasemi, H.; Ahmadi, S. J. *J. Compos. Mater* **2008**, *42*, 2163–2174.

[6] Sellmyer, D. J.; Luo, C. P.; Yan, M. L.; Liu, Y. *IEEE Trans. Magn.* **2001**, *37*, 1286–1291.

[7] Reyes-Esqueda, J. A.; ans H.-G. Silva-Pereyra, V. R.-I.; Torres-Torres, C.; Santiago-Ramirez, A.-L.; Lopez-Suarez, A.; Oliver, A. *Opt. Express* **2009**, *17*, 12849–12868.

[8] Yiu, H. H. P.; j. Niu, H.; Biermans, E.; van Tendeloo, G.; Rosseinsky, M. J. *Adv. Funct. Mater.* **2010**, *20*, 1599–1609.

[9] Murugan, R.; Ramakrishna, S. *Compos. Sci. Technol.* **2005**, *65*, 2385–2406.

[10] Xu, H. H. K.; Sun, J. L.; Chow, L. C. *J. Dent. Res.* **2010**, *89*, 739–745.

[11] Yebassa, D.; Balakrishnan, S.; Raghavan, D. *Nanotech* **2003**, *3*, 246–249.

[12] Garces, J. M.; Moll, D. J.; Bicerano, J.; Fibiger, R.; McLeod, D. G. *Adv. Mater.* **2000**, *12*, 1835–1839.

[13] Karttunen, M.; Ruuskanen, P.; Pitkanen, V.; Albers, W. M. *J. Elec. Mater.* **1908**, *37*, 951–954.

[14] Tan, M. C.; Patil, S. D.; Riman, R. E. *ACS Appl. Mater. Interfaces* **2010**, *2*, 1884–1891.

[15] Lewis, T. J. *IEEE Trans. Diel. Elec. Insul.* **2004**, *11*, 739–753.

[16] Lewis, T. J. *J. Phys. D: Appl. Phys.* **2005**, *38*, 202–212.

[17] Roy, M.; Nelson, J. K.; MacCrone, R. K.; Schadler, L. S.; Reed, C. W.; Keefe, R.; Zenger, W. *IEEE Trans. Diel. Elec. Insul.* **2005**, *12*, 629–643.

[18] Cheng, L.; Zheng, L.; Li, G.; Zeng, J.; Yin, Q. *Physica B* **2008**, *403*, 2584–2589.

[19] Kickelbick, G., Ed. *Hybrid Materials;* Wiley-VCH: Weinhein, 2007.

[20] Lebedev, S. M.; Gefle, O. S.; Tkachenko, S. N. *J. Electrostat.* **2010**, *68*, 122–127.

[21] Srivastava, S.; Haridas, M.; Basu, J. K. *Bull. Mater. Sci.* **2008**, *31*, 213–217.

[22] Qi, L.; Lee, B. I.; Chen, S.; Samuels, W. D.; Exarhos, G. J. *Adv. Mater.* **2005**, *17*, 1777–1781.

[23] Athawale, A. A.; Bhagwat, S. V.; Katre, P. P. *Sens. Actuators, B* **2006**, *114*, 263–267.

[24] Kobayashi, Y.; Tanase, T.; Tabata, T.; Miwa, T.; Konno, M. *J. Eur. Cer. Soc.* **2008**, *28*, 117–122.

[25] Nam, J.-D.; Hwang, S. D.; Choi, H. R.; Lee, J. H.; Kim, K. J.; Heo, S. *Smart Mater. Struct.* **2005**, *14*, 87–90.

[26] Nohales, A.; Munoz-Espi, R.; Felix, P.; Gomez, C. M. *J. Appl. Polym. Sci* **2011**, *119*, 539–547.

[27] Elashmawi, I. S.; Abdelrazek, E. M.; Ragab, H. M.; Hakeem, N. A. *Physica B* **2010**, *405*, 94–98.

[28] Tang, Q.-Y.; Chan, Y.-C.; Wong, N.-B.; Cheung, R. *Polym. Int.* **2010**, *59*, 1240–1245.

[29] Kuo, D.-H.; Lai, C.-C.; Su, T.-Y. *Ceram. Int.* **2004**, *30*, 2177–2181.

[30] Chandra, A.; Turng, L. S.; Gopalan, P.; Rowell, R. M.; Gong, S. Q. *J. Appl. Pol. Sci.* **2007**, *105*, 2728–2736.

[31] Roy, M.; Nelson, J. K.; MacCrone, R. K.; Schadler, L. S. *J. Mater. Sci.* **2007**, *42*, 3789–3799.

[32] Dey, A.; De, S.; De, A.; De, S. K. *Nanotech.* **2004**, *15*, 1277–1283.

[33] Matteucci, S.; Kusuma, V. A.; Kelman, S. D.; Freeman, B. D. *Polymer* **2008**, *49*, 1659–1675.

[34] Singha, S.; Thomas, M. J. *IEEE Trans. Dielectr. Electr. Insul.* **2008**, *15*, 12–23.

[35] Lu, J.; Wong, C. P. *IEEE Trans. Dielectr. Electr. Insul.* **2008**, *15*, 1322–1328.

[36] Ducharme, S. *ACS Nano* **2009**, *3*, 247–2450.

[37] Tanaka, T.; Montanari, G. C.; Mulhaupt, R. *IEEE Trans. Dielectr. Electr. Insul.* **2004**, *11*, 763–784.

[38] Tanaka, T. *IEEE Trans. Dielectr. Electr. Insul.* **2005**, *12*, 914–928.

[39] Frechette, M.; Reed, C. W. In *Electrical Insulation and Dielectric Phenomena, 2007. CEIDP 2007. Annual Report - Conference on*, pages 279–, 2007.

[40] Taurozzi, J. S.; Tarabara, V. V. *Environ. Eng. Sci.* **2007**, *24*, 122–137.

[41] Hanisch, C.; Kulkarni, A.; Zaporojtchenko, V.; Faupel, F. *J. Phys.: Conf. Series* **2008**, *100*, 052043.

[42] Caseri, W. *J. Mater. Chem.* **2010**, *20*, 5582–5592.

[43] Pei, Y.; Yao, F.; Ni, P.; Sun, X. *J. Mod. Opt.* **2010**, *57*, 872–875.

[44] Biswas, A.; Bayer, I. S. In *Vehicular Technology Conference Fall (VTC 2009-Fall), 2009 IEEE 70th*, pages 1 –5, 2009.

[45] Gupta, K.; Jana, P. C.; Meikap, A. K. *Synth. Met.* **2010**, *160*, 1566–1573.

[46] Xu, Z.-X.; Roy, V. A. L.; Stallinga, P.; Muccini, M.; Toffanin, S.; Xiang, H.-F.; Che, C.-M. *App. Phys. Lett.* **2007**, *90*, 223509.

[47] Avasthi, D. K.; Mishra, Y. K.; Kabiraj, D.; Lalla, N. P.; Pivin, J. C. *Nanotechnology* **2007**, *18*, 125604.

[48] Basak, D.; Karan, S.; Mallik, B. *Chem. Phys. Lett.* **2006**, *420*, 115–119.

[49] Mataki, H.; Tsuchii, K.; Mibuka, N.; Suzuki, A.; Taniguchi, J. S. H.; Yamashita, K.; Oe, K. *J. Photopolym. Sci. Technol.* **2007**, *20*, 67–72.

[50] Smythe, E. J.; Dickey, M. D.; Bao, J.; Whitesides, G. M.; Capasso, F. *Nano Lett.* **2009**, *9*, 1132–1138.

[51] Alda, J.; Rico-Garcia, J. M.; Lopez-Alonso, J. M.; Boreman, G. *Nanotechnology* **2005**, *16*, S230–S234.

[52] Lu, C.; Yang, B. *J. Materials Chem.* **2009**, *19*, 2884–2901.

[53] Caseri, W. *Macromol. Rapid. Commun.* **2000**, *21*, 705–722.

[54] El-Sayed, M. A. *Acc. Chem. Res.* **2001**, *34*, 257–264.

[55] Willets, K. A.; Van Duyne, R. P. *Annu. Rev. Phys. Chem.* **2007**, *58*, 267–297.

[56] Noguez, C. *J. Phys. Chem. C* **2007**, *111*, 3806–3819.

[57] Halperin, W. P. *Rev. Mod. Phys.* **1986**, *58*, 533–606.

[58] Uznanski, P.; Bryszewska, E. *J. Mater. Sci.* **2010**, *45*, 1547–1552.

[59] Tao, A.; Sinsermsuksakul, P.; Yang, P. *Angew. Chem.* **2006**, *118*, 4713–4717.

[60] Sun, Y.; Xia, Y. *Science* **2002**, *298*, 2176–2179.

[61] Liu, X.; Huang, R.; Zhu, J. *Chem. Mater.* **2008**, *20*, 192–197.

[62] Jin, R.; Cao, Y.; Mirkin, C. A.; Kelly, K. L.; Schatz, G. C.; Zheng, J. G. *Science* **2001**, *294*, 1901–1903.

[63] Sun, Y.; Yang, B.; Cai, W.; Guizhe, Z.; Zhang, Q. *Micro & Nano Lett.* **2010**, *5*, 162–164.

[64] Deng, Z.; Mansuipur, M.; Muscat, A. J. *J. Phys. Chem. C.* **2007**, *113*, 867–873.

[65] Murphy, C. J.; Jana, N. R. *Adv. Mater.* **2002**, *14*, 80–82.

[66] Park, J.; Joo, J.; Kwon, S. G.; Jang, Y.; Hyeon, T. *Angew. Chem. Int. Ed.* **2007**, *46*, 4630–4660.

[67] Kim, H.-S.; Lee, K.-H.; Kim, S.-G. *Aerosol Sci. Technol.* **2006**, *40*, 536–544.

[68] Baek, K. H.; Kim, J. H.; Lee, K. B.; Ahnn, H. S.; Yoon, C. S. *J. Nanosci. Nanotechnol.* **2010**, *10*, 3118–3122.

[69] Song, Y.; Elsayed-Ali, H. E. *Appl. Surf. Sci.* **2010**, *256*, 5961–5967.

[70] Zhang, J.; Coombs, N.; Kumacheva, E. *J. Am. Chem. Soc.* **2002**, *124*, 14512–14513.

[71] Xu, J.; Munari, A.; Dalton, E.; Matheson, A.; Razeeb, K. M. *J. App. Phys.* **2009**, *106*, 124310.

[72] Godovsky, D. Y. *Device Applications of Polymer-Metal Nanocomposites*, Vol. 153 of *Advances in Polymer Science;* Springer-Verlag: Berlin, Germany, 2000.

[73] Khlebstov, N. G. *J. Nanophotonics* **2010**, *4*, 041587.

[74] Reyes-Esqueda, J. A.; Torres-Torres, C.; Cheang-Wong, J. C.; Crespo-Sosa, A.; Rodriguez-Fernandez, L.; Noguez, C.; Oliver, A. *Opt. Express* **2008**, *16*, 710–717.

[75] Dirix, Y.; Bastiaansen, C.; Caseri, W. *Adv. Mater.* **1999**, *11*, 223–227.

[76] McFarland, A. D.; Van Duyne, R. P. *Nano Lett.* **2003**, *3*, 1057–1062.

[77] Bloemer, M. J.; Haus, J. W. *J. Lightwave Technol.* **1996**, *14*, 1534–1540.

[78] Felidj, N.; Aubard, J.; Levi, G.; Krenn, J. R.; Salerno, M.; Schider, G.; Lamprecht, B.; Leitner, A.; Aussenegg, F. R. *Phys. Rev. B* **2002**, *65*, 075419.

[79] Yang, Y.; Xiong, L.; Shi, J.; Nogami, M. *Nanotechnology* **2006**, *17*, 2670–2674.

[80] Bernabo, M.; Pucci, A.; Ramanitra, H. H.; Ruggeri, G. *Materials* **2010**, *3*, 1461–1477.

[81] Yu, P.; Huang, J.; Tang, J. *Nanoscale Res. Lett.* **2011**, *6*, 46.

[82] Murphy, C. J. *Science* **2002**, *298*, 2139–2141.

[83] Chen, S.; Fan, Z.; Carroll, D. L. *J. Phys. Chem. B* **2002**, *106*, 10777–10781.

[84] Maillard, M.; Giorgio, S.; Pileni, M.-P. *Adv, Mater.* **2002**, *14*, 1084–1086.

[85] Tang, B.; An, J.; Zheng, X.; Xu, S.; Li, D.; Zhou, J.; Zhao, B.; Xu, W. *J. Phys. Chem. C* **2008**, *112*, 18361–18367.

[86] Zhu, Y. C.; Geng, W. T. *J. Phys. Chem. C* **2008**, *112*, 8545–8547.

[87] Germain, V.; Li, J.; Ingert, D.; Wang, Z. L.; Pileni, M. P. *J. Phys. Chem. B* **2003**, *107*, 8717–8720.

[88] Qin, H.; Gao, Y.; Teng, J.; Xu, H.; Wu, K.; Gao, S. *Nano Lett.* **2010**, *10*, 2961–2964.

[89] Maillard, M.; Giorgio, S.; Pileni, M.-P. *J. Phys. Chem. B* **2003**, *107*, 2466–2470.

[90] Sun, Y.; Xia, Y. In Cao, G., Xia, Y., Braun, P. V., Eds., *Society of Photo-Optical Instrumentation Engineers (SPIE) Conference Series*, Vol. 5224, pages 43–52, 2003.

[91] Kan, C. X.; Zhu, J.-J.; Zhu, X.-G. *J. Phys. D: Appl. Phys.* **2008**, *41*, 155304.

[92] Wiley, B.; Sun, Y.; Mayers, B.; Xia, Y. *Chem. Eur. J.* **2005**, *11*, 454–463.

[93] Tang, X.; Tsuji, M.; Nishio, M.; Jiang, P. *Bull. Chem. Soc. Jpn.* **2009**, *82*, 1304–1312.

[94] Tsuji, M.; Matsumoto, K.; Miyamae, N.; Tsuji, T.; Zhang, X. *Crystal Growth & Design* **2007**, *7*, 311–320.

[95] Sun, Y.; Yin, Y.; Mayers, B. T.; Herricks, T.; Xia, Y. *Chem. Mater.* **2002**, *14*, 4736–4745.

[96] Gao, Y.; Jiang, P.; Liu, D. F.; Yuan, H. J.; Yan, X. Q.; Zhou, Z. P.; Wang, J. X.; Song, L.; Liu, L. F.; Zhou, W. Y.; Wang, G.; Wang, C. Y.; Xie, S. S. *Chem. Phys. Lett.* **2003**, *380*, 146–149.

[97] Gao, Y.; Song, L.; Jiang, P.; Liu, L. F.; Yan, X. Q.; Zhou, Z. P.; Liu, D. F.; Wang, J. X.; Yuan, H. J.; Zhang, Z. X.; Zhao, X. W.; Dou, X. Y.; Zhou, W. Y.; Wang, G.; Xie, S. S.; Chen, H. Y.; Li, J. Q. *J. Cryst. Growth* **2005**, *276*, 606–612.

[98] Gao, Y.; Liu, D. F.; Yuan, H. J.; Yan, X. Q.; Zhou, Z. P.; Wang, J. X.; Song, L.; Liu, L. F.; Zhou, W. Y.; Wang, G.; Wang, C. Y.; Xie, S. S.; Zhang, J. M.; Shen, D. Y. *J. Phys. Chem. B* **2004**, *108*, 12877–12881.

[99] Tao, A.; Kim, F.; Hess, C.; Goldberger, J.; He, R.; Sun, Y.; Xia, Y.; Yang, P. *Nano Lett.* **2003**, *3*, 1229–1233.

[100] Krenn, J. R.; Schider, G.; Rechberger, W.; Lamprecht, B.; Leitner, A.; Weeber, J. C. *App. Phys. Lett.* **2000**, *77*, 3379–3381.

[101] Wilson, O.; Wilson, G. J.; Mulvaney, P. *Adv. Mater.* **2002**, *14*, 1000–1004.

[102] Chaney, S. B.; Shanmukh, S.; Dluhy, R. A.; Zhao, Y.-P. *Appl. Phys. Lett.* **2005**, *87*, 031908.

[103] Evans, P. R.; Hendren, W. R.; Atkinson, R.; Pollard, R. J. *Nanotechnology* **2008**, *19*, 465708.

[104] Zhao, Y.-P.; Chaney, S. B.; Shanmukh, S.; Dluhy, R. A. *J. Phys. Chem. B* **2006**, *110*, 3153–3157.

[105] Li, D.; Komarneni, S. *J. Nanosci. Nanotechnol.* **2010**, *10*, 8035–8042.

[106] Jensen, L. L.; Jensen, L. *J. Phys. Chem. C* **2009**, *113*, 15182–15190.

[107] Cortie, M. B.; Xu, X.; Ford, M. J. *Phys. Chem. Chem. Phys.* **2006**, *8*, 3520–3527.

[108] Johnson, H. E.; Aikens, C. M. *J. Phys. Chem. A* **2009**, *113*, 4445–4450.

[109] Clausius, R. *Die mechanistische Warmelehre II;* Vieweg: Braunschweig, 1879.

[110] Mossotti, O. F. *Mem. dell Soc. Scient. Modena* **1850**, *14*, 49.

[111] Lorenz, L. *Vidensk. Selsk. Skrifter* **1869**, *8*, 205.

[112] Lorentz, H. A. *Wiedem. Ann.* **1880**, *9*, 641.

[113] Lorenz, L. *Wiedem. Ann.* **1881**, *11*, 70.

[114] Garnett, J. C. M. *Phil. Trans. R. Soc. Lond. A* **1906**, *205*, 237–288.

[115] Bruggeman., D. A. G. *Ann. Phys.* **1935**, *24*, 636.

[116] Looyenga, H. *Physica* **1965**, *31*, 401.

[117] Landau, L. D.; Lifschitz, E. M. *Lehrbuch der Theoretischen Physik VIII: Elektrodynamik der Kontinua;* Akademie: Berlin, 1974.

[118] Lichtenecker, K. *Phys. Z.* **1926**, *27*, 115–158.

[119] Dang, Z.-M.; Shen, Y.; Nan, C.-W. *App. Phys. Lett.* **2002**, *81*, 4814–4816.

[120] Kreibig, U.; Vollmer, M. *Optical Properties of Metal Clusters;* Springer: Berlin, 1995.

[121] Sihvola, A. *Electromagnetic Mixing Formulas and Applications;* Institution of Electrical Engineers: London, U.K., 1999.

[122] King-Smith, R. D.; Vanderbilt, D. *Phys. Rev. B* **1993**, *47*, 1651–1654.

[123] Resta, R. *Rev. Mod. Phys.* **1994**, *66*, 899.

[124] Lindhard, J. *Kgl. Danske Videnskab. Selskab: Mat. Fys. Medd.* **1954**, *28*, 1–57.

[125] Nozieres, P.; Pines, D. *Phys. Rev.* **1959**, *113*, 1254–1267.

[126] Ehrenreich, H.; Cohen, M. H. *Phys. Rev.* **1959**, *115*, 786–790.

[127] Zwijnenburg, M. A.; Sousa, C.; Sokol, A. A.; Bromley, S. T. *J. Chem. Phys.* **2008**, *129*, 014706.

[128] Takagi, Y.; Okada, S. *Phys. Rev. B* **2009**, *79*, 233406.

[129] Guo, G. Y.; Chu, K. C.; s. Wang, D.; g. Duang, C. *Phys. Rev. B* **2004**, *69*, 205416.

[130] Borges, P. D.; Scolfaro, L. M. R.; Alves, H. W. L.; da Silva Jr., E. F. *Theor. Chem. Acc.* **2010**, *126*, 39–44.

[131] Guzman, D.; Cruz, M.; Wang, C. *Microelectr. J.* **2008**, *39*, 523–525.

[132] Martin, R. M. *Electronic Structure;* Cambridge University Press: Cambridge, U.K., 2008.

[133] Krawczyk, P. *J. Mol. Model.* **2010**, *16*, 659–668.

[134] Wiley, B. J.; Chen, Y.; McLelland, J. M.; Xiong, Y.; Li, Z.-Y.; Ginger, D.; Xia, Y. *Nano Letters* **2007**, *7*, 1032–1036.

[135] Zheng, W.; Lu, X.; Wang, W.; Wang, Z.; Song, M.; Wang, Y.; Wang, C. *Phys. Status Solidi A* **2010**, pages 1–4.

[136] Miranda, D.; Sencadas, V.; Sanchez-Iglesias, A.; Pastoriza-Santos, I.; Liz-Marzan, L. M.; Ribelles, J. L. G.; Lanceros-Mendez, S. *J. Nanosci. Nanotech.* **2009**, *9*, 2910–2916.

[137] Huang, X.; Jiang, P.; Xie, L. *App. Phys. Lett.* **2009**, *95*, 242901.

[138] Gregario, R.; Borges, D. S. *Polymer* **2008**, *49*, 4009–4016.

[139] Bauer, F. *IEEE Trans. Ultr. Ferr. Freq. Cont.* **2000**, *47*, 1448–1454.

[140] Wegener, M.; Gerhard-Multhaupt, R. *IEEE Trans. Ultr. Ferr. Freq. Cont.* **2003**, *50*, 921–931.

[141] Setiadi, D.; He, Z.; Hajto, J.; Binnie, T. D. *Infr. Phys. Tech.* **1999**, *40*, 267–278.

[142] Rietveld, I. B.; Kobayashi, K.; Honjo, T.; Ishida, K.; Yamada, H.; Matsushige, K. *J. Mat. Chem.* **2010**, *20*, 8272–8278.

[143] Harb, M.; Rabilloud, F.; Simon, D.; Rydlo, A.; Lecoultre, S.; Conus, F.; Rodriguez, V.; Felix, C. *J. Chem. Phys.* **2008**, *129*, 194108.

[144] Conus, F.; Lau, J. T.; Rodriguez, V.; Felix, C. *Rev. Sci. Instrum.* **2006**, *77*, 113103.

[145] Harbich, W.; Fedrigo, S.; Buttet, J. *Chem. Phys. Lett.* **1992**, *195*, 613–616.

[146] Federmann, F.; Hoffmann, K.; Quaas, N.; Toennies, J. P. *Eur. Phys. J. D* **1999**, *9*, 11–14.

[147] Fedrigo, S.; Harbich, W.; Buttet, J. *Phys. Rev. B* **1993**, *47*, 10706–10715.

[148] Fedrigo, S.; Harbich, W.; Belyaev, J.; Buttet, J. *Chem. Phys. Lett.* **1993**, *211*, 166–170.

[149] Zhang, Q.; Li, W.; Moran, C.; Zeng, J.; Chen, J.; Wen, L.-P.; Xia, Y. *J. Am. Chem. Soc.* **2010**, *132*, 11372–11378.

[150] Silverstein, D. W.; Jensen, L. *J. Chem. Phys.* **2010**, *132*, 194302.

[151] Zhao, G. F.; Lei, Y.; Zeng, Z. *Chem. Phys.* **2006**, *327*, 261–268.

[152] Harb, M.; Rabilloud, F.; Simon, D. *Chem. Phys. Lett.* **2009**, *476*, 186–190.

[153] Baishya, K.; Idrobo, J. C.; Ogut, S.; Yang, M.; Jackson, K.; Jellinek, J. *Phys. Rev. B* **2008**, *78*, 075439.

[154] Aikens, C. M.; Li, S.; Schatz, G. C. *J. Phys. Chem. C* **2008**, *112*, 11272–11279.

[155] Encina, E. R.; Coronado, E. A. *J. Phys. Chem. C* **2010**, *114*, 3918–3923.

[156] Hao, E.; Schatz, G. C.; Hupp, J. T. *J. Fluorescence* **2004**, *14*, 331–341.

[157] Jensen, T. R.; Schatz, G. C.; Van Duyne, R. P. *J. Phys. Chem. B* **1999**, *103*, 2394–2401.

[158] Jensen, T. R.; Duval, M. L.; Kelly, K. L.; Lazarides, A. A.; Schatz, G. C.; Duyne, R. P. V. *J. Phys. Chem. B* **1999**, *103*, 9846–9853.

[159] N'Gom, M.; Li, S.; Schatz, G.; Erni, R.; Agarwal, A.; Kotov, N.; Norris, T. B. *Phys. Rev. B* **2009**, *80*, 113411.

[160] Brioude, A.; Pileni, M. P. *J. Chem. Phys. B* **2005**, *109*, 23371–23377.

[161] Tiggesbaumker, J.; Koller, L.; Meiwes-Broer, K.-H. *Chem. Phys. Lett.* **1996**, *260*, 428–432.

[162] Fedrigo, S.; Harbich, W.; Belyaev, J.; Butter, J. *Chem. Phys. Lett.* **1993**, *211*, 166–170.

[163] Tiggesbaumker, J.; Koller, L.; Meiwes-Broer, K.-H. *Phys. Rev. A* **1993**, *48*, R1749–R1752.

[164] Harbich, W.; Fedrigo, S.; Buttet, J. *Z. Phys. D: At. Mol. Clusters* **1993**, *26*, 138–140.

[165] Harbich, W. *Philos. Mag.* **1999**, *79*, 1307–1320.

[166] Jensen, F. *Introduction to Computational Chemistry;* John Wiley & Sons: NY, USA, 2002.

[167] Gromacs user manual version 4.0. van der Spoel, D.; Lindahl, E.; Hess, B.; van Buuren, A. R.; Apol, E.; Meulenhoff, P. J.; Tieleman, D. P.; Sijers, A. L. T. M.; Feenstra, K. A.; van Drunen, R.; Berendsen, H. J. C.; The GROMACS development team, Groningen, Netherlands, **2006**.

[168] Hess, B.; Kutzner, C.; van der Spoel, D.; Lindahl, E. *J. Chem. Theory Comput.* **2008**, *4*, 435–447.

[169] van der Spoel, D.; Lindahl, E.; Hess, B.; Groenhof, G.; Mark, A. E.; Berendsen, H. J. C. *J. Comp. Chem.* **2005**, *26*, 1701–1719.

[170] Lindhal, E.; Hess, B.; van der Spoel, D. *J. Mol. Mod.* **2001**, *7*, 306–317.

[171] Berendsen, H. J. C.; van der Spoel, D.; van Drunen, R. *Comp. Phys. Comm.* **1995**, *91*, 43–56.

[172] Parrinello, M.; Rahman, A. *J. Appl. Phys.* **1981**, *52*, 7182–7190.

[173] Nose, S. *Mol. Phys.* **1984**, *52*, 255–268.

[174] Hoover, W. G. *Phys. Rev. A* **1985**, *31*, 1695–1697.

[175] Byutner, O. G.; Smith, G. D. *Macromolecules* **2000**, *33*, 4264–4270.

[176] Chen, Y.; Shew, C.-Y. *J. Mol. Model.* **2003**, *9*, 379–389.

[177] Rappe, A. K.; Casewit, C. J.; Colwell, K. S.; Goddard, W. A.; Skiff, W. M. *J. Am. Chem. Soc.* **1992**, *114*, 10024–10035.

[178] Essman, U.; Perela, L.; Berkowitz, M. L.; Darden, T.; Lee, H.; Pedersen, L. G. *J. Chem. Phys.* **1995**, *103*, 8577–8592.

[179] Hohenberg, P.; Kohn, W. *Phys. Rev. B* **1964**, *136*, 864–871.

[180] Kohn, W.; Sham, L. J. *Phys. Rev. A* **1965**, *140*, 1133–1138.

[181] Bohm, D.; Pines, D. *Phys. Rev.* **1953**, *92*, 609–625.

[182] Fox, M. *Optical Properties of Solids;* Oxford University Press: Oxford, UK, 2008.

[183] Kittel, C. *Introduction to Solid State Physics;* John Wiley & Sons, Inc: N.Y., 1976.

[184] Hummel, R. E. *Electronic Properties of Materials;* Springer-Verlag: N.Y., 1993.

[185] Martin, T. P. *Solid State Ionics* **2000**, *131*, 3–12.

[186] Gonze, X.; Lee, C. *Phys. Rev. B* **1997**, *55*, 10355.

[187] He, Y.; Zeng, T. *J. Phys. Chem. C* **2010**, *114*, 18023.

[188] Soler, J. M.; Artacho, E.; Gale, J. D.; Garcia, A.; Junquera, J.; Ordejon, P.; Sanchez-Portal, D. *J. Phys.: Condens. Matter* **2002**, *14*, 2745.

[189] Ordejon, P.; Artacho, E.; Soler, J. M. *Phys. Rev. B (Rapid Comm.)* **1996**, *53*, R10441.

[190] Perdew, J. P.; Burke, K.; Ernzerhof, M. *Phys. Rev. Lett.* **1996**, *77*, 3865–3868.

[191] Troullier, N.; Martins, J. L. *Phys. Rev. B* **1991**, *43*, 1993–2006.

[192] Lez-Encarnaci, J. M.; Burton, J. D.; Tsymbal, E. Y.; Velev, J. P. *Nano Lett.* **2010**, *11*, 599–603.

[193] Elba, O.; Angeles, C.; Luis, N.; Carlos, C.-R.; Qing, W. *Quantum Chemical Investigations of Structural Parameters of PVDF-based Organic Ferroelectric Materials;* InTech, 2010.

[194] Choi, J.; Dowben, P. A.; Pebley, S.; Bune, A. V.; Ducharme, S.; Fridkin, V. M.; Palto, S. P.; Petukhova, N. *Phys. Rev. Lett.* **1998**, *80*, 13281331.

[195] Greco, T.; Wang, F.; Wegner, M. *Ferroelectrics* **2010**, *405*, 85–91.

[196] Jackschath, C.; Rabin, I.; Schulze, W. *Z. Phys. D: At. Mol. Clusters* **1992**, *22*, 517–520.

[197] Chiu, Y.-P.; Wei, C.-M.; Chang, C.-S. *Phys. Rev. B* **2008**, *78*, 115402.

[198] Wang, J.; Wang, G.; Zhao, J. *Chem. Phys. Lett.* **2003**, *380*, 716–720.

[199] Chiu, Y.-P.; Huang, B. *Jpn. J. Appl. Phys.* **2009**, *48*, 06FF11.

[200] Yang, M.; Jackson, K. A.; Jellinek, J. *J. Chem. Phys.* **2006**, *125*, 144308.

[201] Germain, V.; Brioude, A.; Ingert, D.; Pileni, M. P. *J. Chem. Phys.* **2005**, *122*, 124707.

[202] Scmucker, A. L.; Harris, N.; Banholzer, M. J.; Blaber, M. G.; Osberg, K. D.; Schatz, G. C.; Mirkin, C. A. *ACS Nano* **2010**, *4*, 5453–5463.

[203] Liao, M.-S.; Bonifassi, P.; Leszczynski, J.; Ray, P. C.; Huang, M.-J.; Watts, J. D. *J. Phys. Chem. A* **2010**, *114*, 12701–12708.

Appendix A

Method development

The design of NC systems and simulation cells was overviewed in Chapter 2. Presented below is a detailed account of the specific methods undertaken to construct simulation cells and run classical and DFT simulations.

A.1 MM/MD Simulations

Ag NP coordinates were obtained from home-built FORTRAN programs that generated atomic coordinates based on the fcc lattice constant of Ag (4.086 Å). Distances between neighboring atoms were calculated from trigonometry. Specific NP shapes were generated by replicating atomic coordinates.

For the two systems designed in GaussView, Ag_{13} (NP A) coordinates were input by hand into GaussView. The polymer chain, built as a fragment molecule in GaussView, was then twisted about the inclusion, forming an almost spherical shape.

Since PVDF was not one of the available parameterized molecules in Gromacs, the topology file describing the atomic connectivity had to be constructed. This consisted of generating three lists. The first provided a numerical listing of atoms that corresponded to the order of atoms given in the coordinate file. The atomic index was also assigned an atom type, elemental symbol, mass, partial charge and charge group. The second list specified the connectivity between atoms, with the equilibrium bond lengths and stretching constants. The third provided bond angles between atoms with equilibrium bond lengths and constants. Since atoms are referred to by number in the topology file, it was important to ensure that the polymer constructed in GaussView had a sequential and patterned assignment of atom ordering in the coordinate file. This organization facilitated writing a FORTRAN program to generate each of the three lists for a given polymer chain length and number of silver atoms.

Coordinate files from GaussView had to be transformed into the protein databank format (.pdb) which Gromacs could interpret. The Gaussian file format (.gjf) from GaussView was converted to .xyz format using vim, the Linux-based text editor. The .xyz format was then converted into protein databank format (.pdb) using a home-built FORTRAN program. The simulation cell lattice constants were specified using the editconf subroutine in Gromacs.

Force field files, with bonding and non-bonding parameters taken from the literature, were formatted to be read by Gromacs. An index file was generated using the make_ndx subroutine in Gromacs, so that relative Ag atom coordinates could be frozen and not scaled by pressure coupling runs. Systems were minimized using the conjugate gradient (CG) algorithm, as it was the only energy minimization algorithm available in Gromacs which respected frozen atoms. Minimization was performed by sequentially decreasing the maximum force tolerance from 100 to 0.1 $\mathrm{kJ \cdot mol^{-1} \cdot nm^{-1}}$. A script file was written to fully automate this procedure. This was necessary because a small maximum force tolerance did not necessarily provide the lowest energy structure. The output files were read to select that with the lowest maximum force.

MD pressure coupling runs were performed incrementally. Compression occurred very slowly, and MD runs would terminate unexpectedly. When this occurred, the time constant was increased, which often resolved the issue. When this failed to provide a stable pressure coupling run that would complete 50,000 steps, a number of options were attempted: a different system geometry and coordinates were taken from a previous MD run; MD runs were performed with no pressure coupling (under constant volume) in effort to obtain a stable starting geometry; geometries were relaxed; or any combination of the above.

After each successful pressure coupling run, the step with the lowest volume was selected for subsequent compression. This was done using the g_energy subroutine in Gromacs, which printed cell volumes at every 100^{th} step. Specific run coordinates were then extracted using the trjconv subroutine.

Although Ag atoms were frozen, pressure coupling did scale NP coordinates. When the final cell volume and density were obtained, NP coordinates were regenerated from the FORTRAN program, and reincorporated into the coordinate file. This system was then annealed from 1000–25K over 780,000 steps with 0.001 ps step sizes, followed by sequential energy minimization using CG.

Additional NC systems were designed from previously compacted structures. Different NP coordinates were placed into the volume of space formed by the previous NP. In extreme cases, where the NP was so large as to overlap with polymer atoms,

selected NP atoms were excluded until additional MD simulations provided sufficient space around the silver cluster.

In the polydisperse system, the second inclusion was grown by first placing a single Ag atom amongst polymer atoms. With subsequent MD runs, more space was formed around the atom, enabling additional atoms to be placed. The two inclusions were then gradually translated to opposite vertices through additional MD runs until the NPs were roughly equidistant from each other, both through the cell and across PBC images. Coordinate files from Gromacs were converted into the coordinate file format of SIESTA using vim.

A.2 DFT Simulations

DFT simulations used input parameters as exemplified in the sample input file in Figure A.2. DM.NumberPulay and DM.MixingWeight values were not optimized for SCF convergence. For spin-polarized calculations, SCF convergence was achieved by setting DM.NumberPulay to zero, and DM.MixingWeight to 0.1. DirectPhi and SaveMemory were set to true to reduce the large memory requirement in optical calculations of large systems. A large MeshCutoff of 500 Ry was used to ensure numerical convergence. A minimal optical.Mesh sampling of 1×1×1 was used, since larger sampling sizes caused the run to crash – likely a result of insufficient memory.

```
SystemName      1250 atom PVDF chain with 19 atom Ag disk
SystemLabel     500mc1250disk19optX05
NumberOfAtoms   1269
NumberOfSpecies 4

MD.TypeOfRun    CG
MD.NumCGsteps   0
MD.ConstantVolume  .true.
SolutionMethod  diagon
XC.functional   GGA
XC.authors      PBE
PAO.BasisSize   DZP
DM.NumberPulay  7
DM.MixingWeight 0.1
DirectPhi       .true.
SaveMemory      .true.
MeshCutoff      500 Ry
MaxSCFiterations 200
UseSaveData     .true.
WriteMullikenPop 1

OpticalCalculation      .true.
%block Optical.Mesh
 1 1 1
%endblock Optical.Mesh
Optical.PolarizationType  polarized
%block Optical.Vector
 1.0 0.0 0.0
%endblock Optical.Vector
Optical.Broaden         0.05 eV
Optical.EnergyMinimum   0.001 eV
Optical.EnergyMaximum   100.0 eV

%block ChemicalSpeciesLabel
 1   1   H
 2   6   C
 3   9   F
 4  47   Ag
%endblock ChemicalSpeciesLabel

LatticeConstant 1.0 Ang

%block LatticeParameters
  22.410   24.338   23.519   90.0 90.0 90.0
%endblock LatticeParameters

AtomicCoordinatesFormat Ang

%block AtomicCoordinatesAndAtomicSpecies < 1250disk19.coor
%endblock AtomicCoordinatesAndAtomicSpecies
~
```

Figure A.2: Sample DFT (SIESTA) input file.

Appendix B

Additional Spectra

Additional optical spectra and densities of states are presented here for NPs and NCs. Figures B.1–8 show the complex dielectric constant ($\epsilon = \epsilon_1 + \epsilon_2$), reflectance at normal incidence (R) and absorption coefficient (α) of NPs B–I along with the NC spectra, showing the influence of NP loading. Densities of states and imaginary dielectric constant are shown in Figures B.9–14 for all NPs and selected NCs, where not present in the discussion.

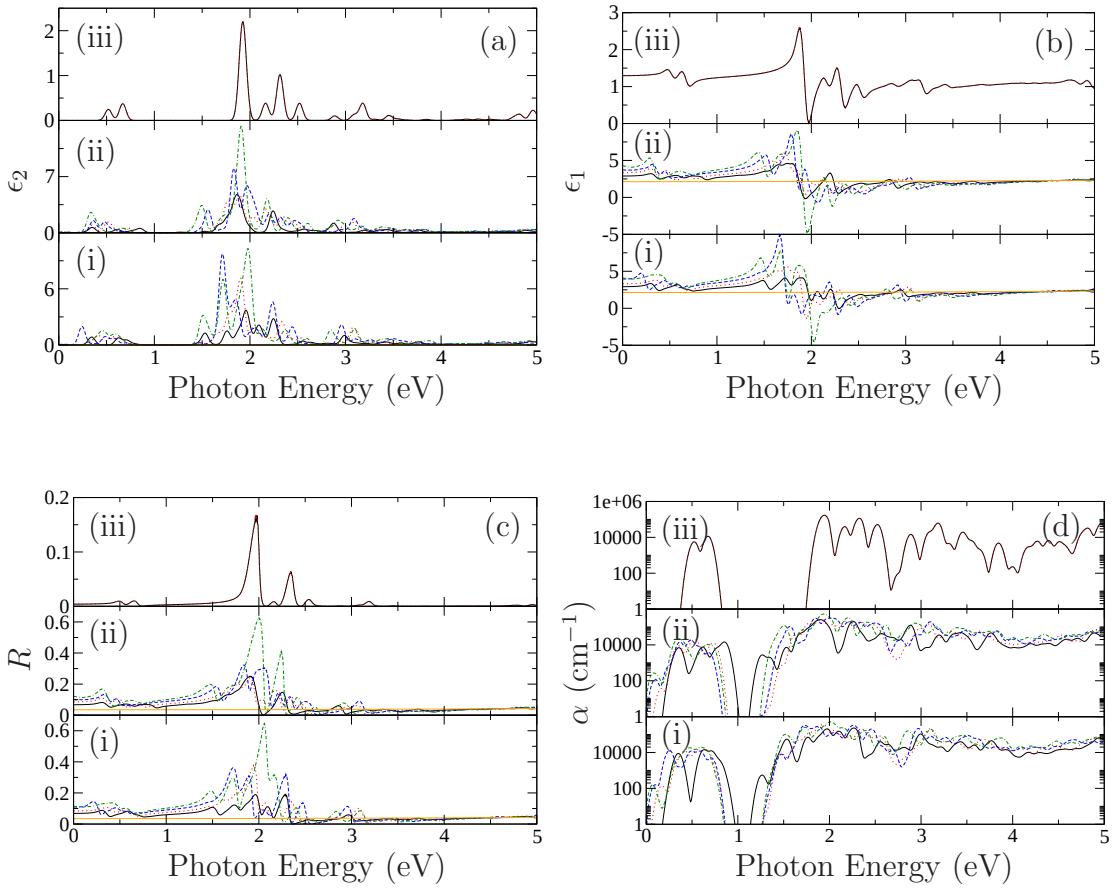

Figure B.1: Influence of NP volume fraction and incident field polarization on the optical properties of NP B and corresponding NC materials. Imaginary permittivity (ϵ_2), real permittivity (ϵ_1), normal reflectance (R) and absorption coefficient (α) are presented in panels (a)-(d), respectively. In each graph, subpanels (i) and (ii) report optical properties of NC with incident light polarized along the z- and x-axes of the NP, respectively. Subpanel (iii) presents the respective optical property of the NP in vacuum, with incident fields along the z-axis (black line) and along x (dotted red line). For the present plot, the optical properties of pure NP do not depend on field direction, and the lines in subpanels (iii) are superimposed. In subpanels (i) and (ii), different lines correspond to different NC volume fractions, as follows: solid black – B/1250 (2.5%vol), dotted red – B/836 (3.7%vol), dashed blue – B/644 (4.8%vol), dot-dashed green – B/536 (5.7%vol). Horizontal solid orange lines represent the pure amorphous PVDF polymer. Where the orange line is not visible, it coincides with the graph's abscissa.

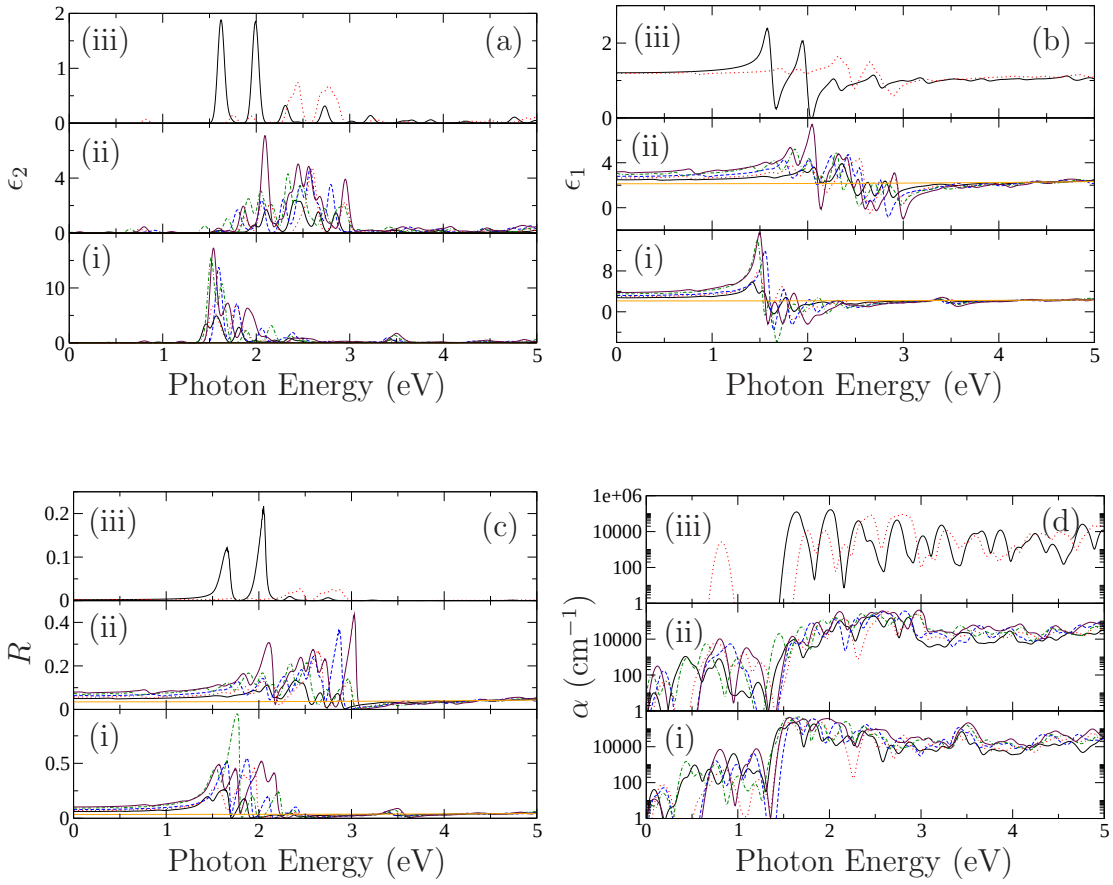

Figure B.2: Influence of NP volume fraction and incident field polarization on the optical properties of NP C and corresponding NC materials. Imaginary permittivity (ϵ_2), real permittivity (ϵ_1), normal reflectance (R) and absorption coefficient (α) are presented in panels (a)-(d), respectively. In each graph, subpanels (i) and (ii) report optical properties of NC with incident light polarized along the z- and x-axes of the NP, respectively. Subpanel (iii) presents the respective optical property of the NP in vacuum, with incident fields along the z-axis (black line) and along x (dotted red line). In subpanels (i) and (ii), different lines correspond to different NC volume fractions, as follows: solid black – C/1250 (2.0%vol), dotted red – C/836 (3.0%vol), dashed blue – C/644 (3.8%vol), dot-dashed green – C/536 (4.6%vol), solid maroon – C/416 (5.8%vol). Horizontal solid orange lines represent the pure amorphous PVDF polymer. Where the orange line is not visible, it coincides with the graph's abscissa.

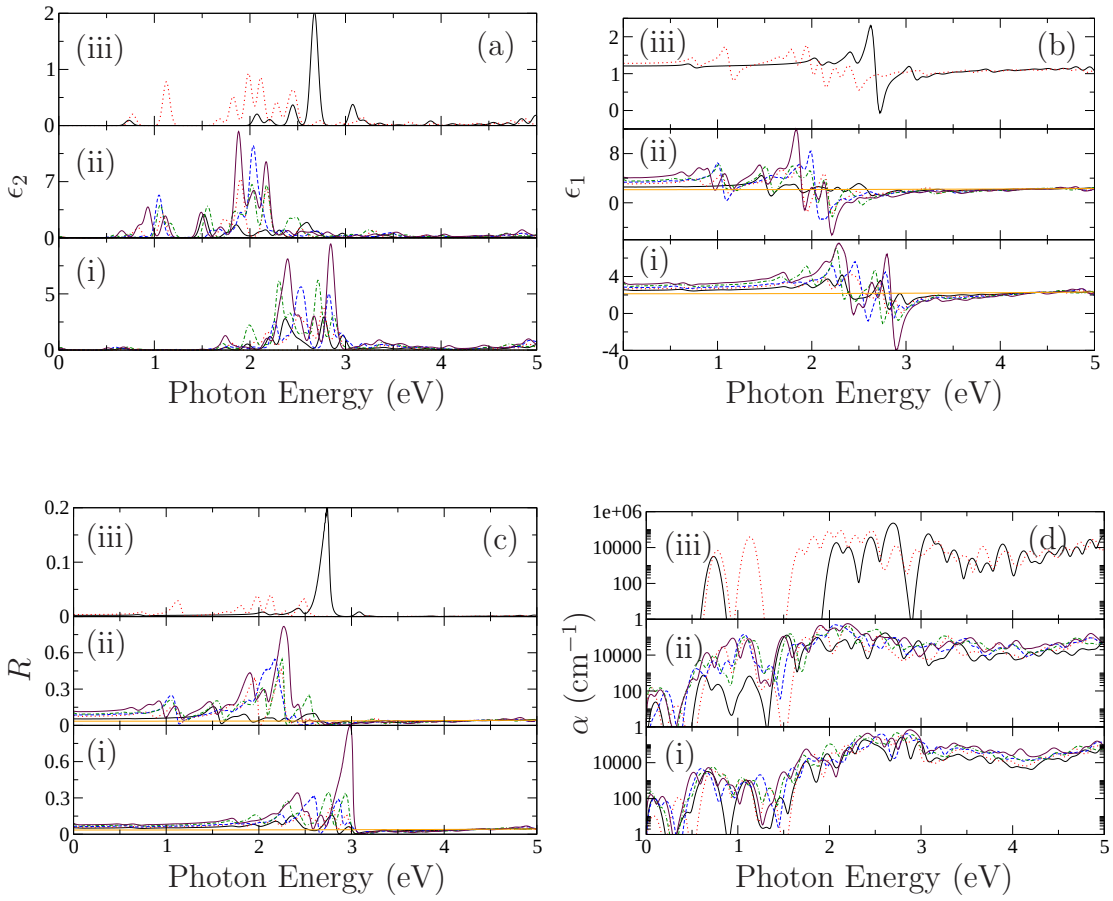

Figure B.3: Influence of NP volume fraction and incident field polarization on the optical properties of NP D and corresponding NC materials. Imaginary permittivity (ϵ_2), real permittivity (ϵ_1), normal reflectance (R) and absorption coefficient (α) are presented in panels (a)-(d), respectively. In each graph, subpanels (i) and (ii) report optical properties of NC with incident light polarized along the z- and x-axes of the NP, respectively. Subpanel (iii) presents the respective optical property of the NP in vacuum, with incident fields along the z-axis (black line) and along x (dotted red line). In subpanels (i) and (ii), different lines correspond to different NC volume fractions, as follows: solid black – D/1250 (2.3%vol), dotted red – D/836 (3.4%vol), dashed blue – D/644 (4.3%vol), dot-dashed green – D/536 (5.1%vol), solid maroon – D/416 (6.5%vol). Horizontal solid orange lines represent the pure amorphous PVDF polymer. Where the orange line is not visible, it coincides with the graph's abscissa.

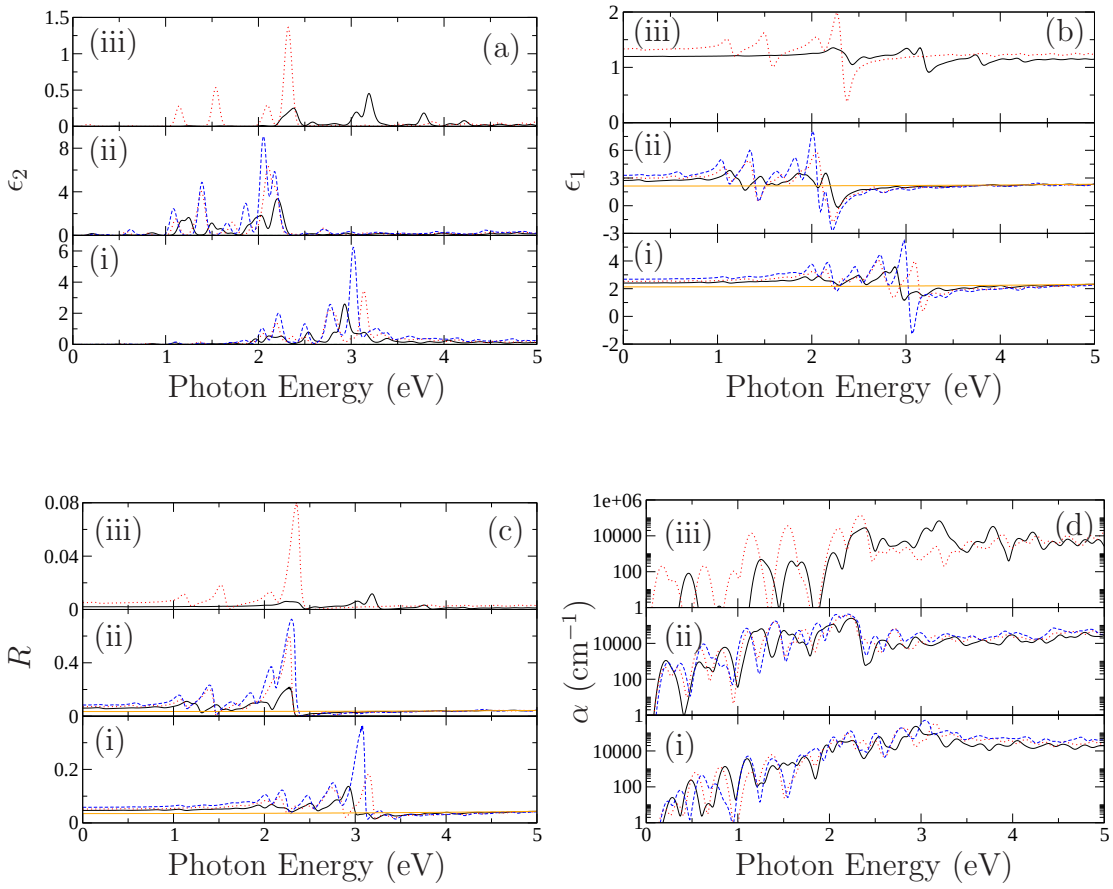

Figure B.4: Influence of NP volume fraction and incident field polarization on the optical properties of NP E and corresponding NC materials. Imaginary permittivity (ϵ_2), real permittivity (ϵ_1), normal reflectance (R) and absorption coefficient (α) are presented in panels (a)-(d), respectively. In each graph, subpanels (i) and (ii) report optical properties of NC with incident light polarized along the z- and x-axes of the NP, respectively. Subpanel (iii) presents the respective optical property of the NP in vacuum, with incident fields along the z-axis (black line) and along x (dotted red line). In subpanels (i) and (ii), different lines correspond to different NC volume fractions, as follows: solid black – E/1250 (2.0%vol), dotted red – E/836 (3.0%vol), dashed blue – E/590 (4.2%vol). Horizontal solid orange lines represent the pure amorphous PVDF polymer. Where the orange line is not visible, it coincides with the graph's abscissa.

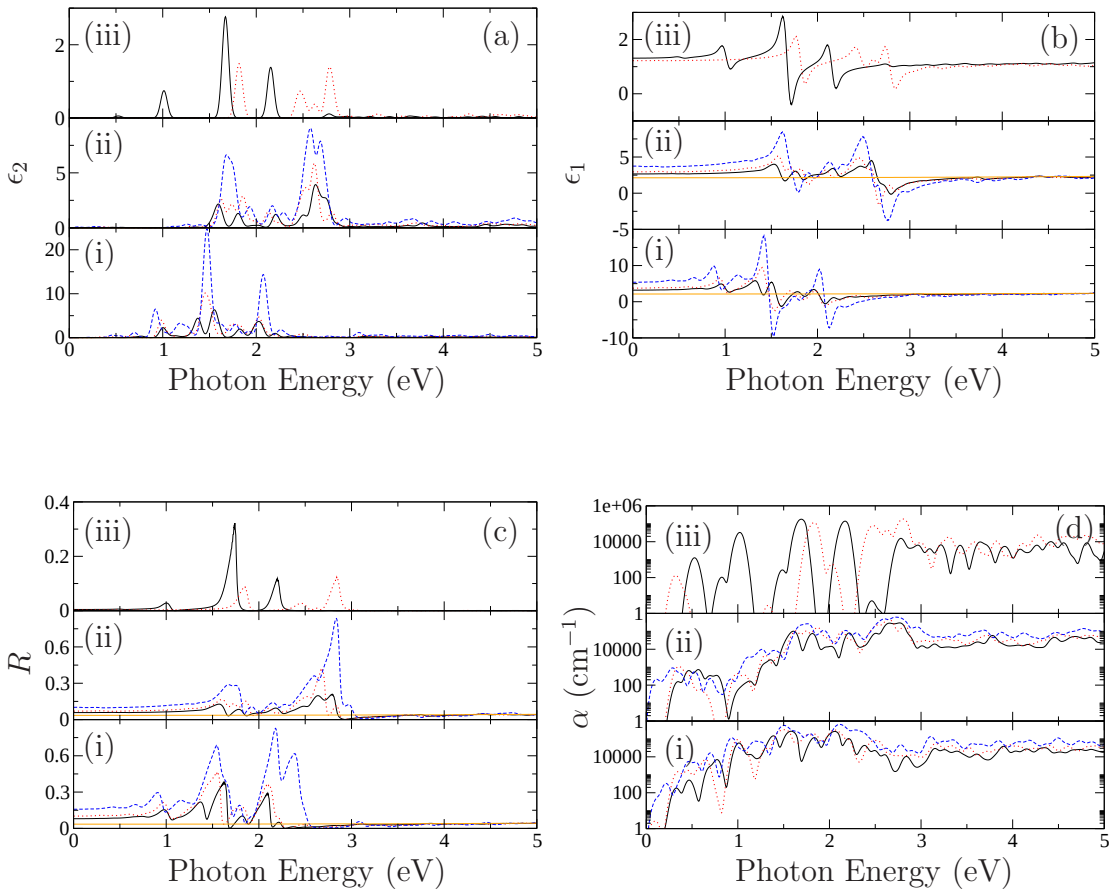

Figure B.5: Influence of NP volume fraction and incident field polarization on the optical properties of NP F and corresponding NC materials. Imaginary permittivity (ϵ_2), real permittivity (ϵ_1), normal reflectance (R) and absorption coefficient (α) are presented in panels (a)-(d), respectively. In each graph, subpanels (i) and (ii) report optical properties of NC with incident light polarized along the z- and x-axes of the NP, respectively. Subpanel (iii) presents the respective optical property of the NP in vacuum, with incident fields along the z-axis (black line) and along x (dotted red line). In subpanels (i) and (ii), different lines correspond to different NC volume fractions, as follows: solid black – F/1250 (2.9%vol), dotted red – F/836 (4.3%vol), dashed blue – F/416 (8.3%vol). Horizontal solid orange lines represent the pure amorphous PVDF polymer. Where the orange line is not visible, it coincides with the graph's abscissa.

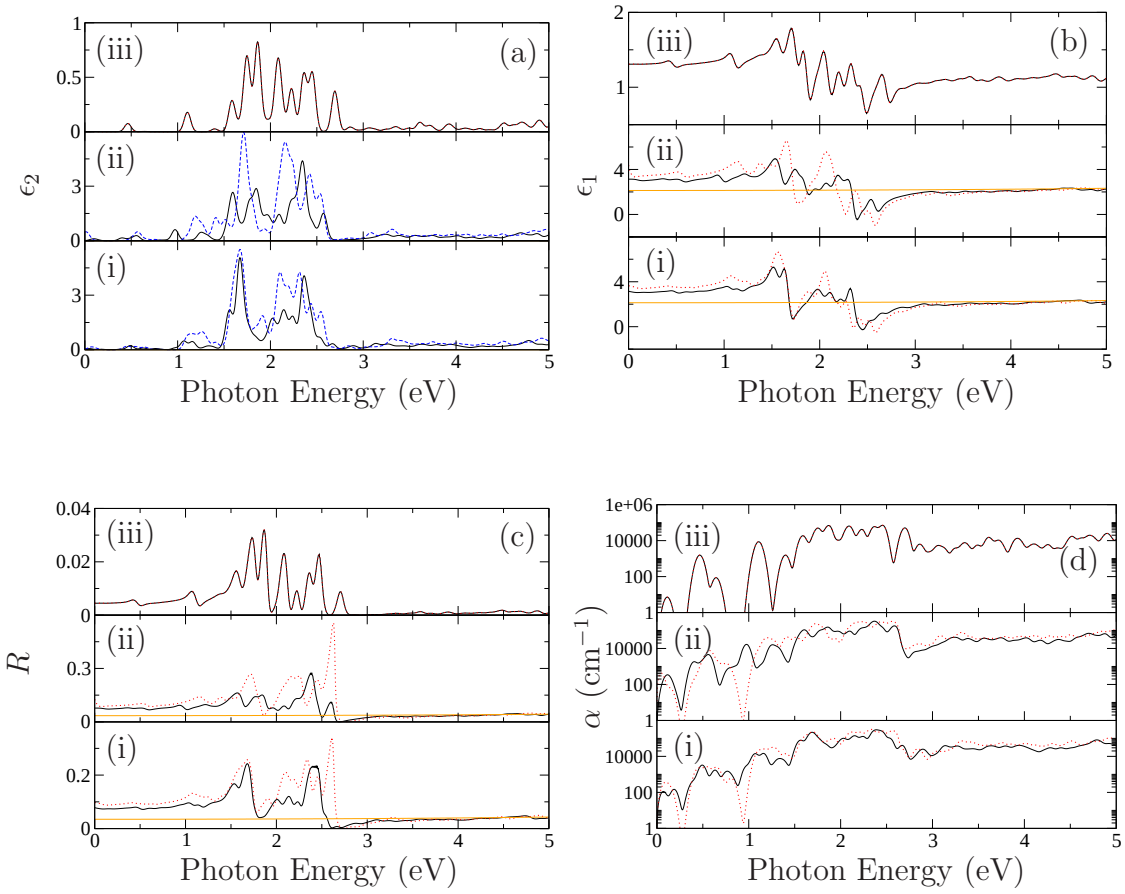

Figure B.6: Influence of NP volume fraction and incident field polarization on the optical properties of NP G and corresponding NC materials. Imaginary permittivity (ϵ_2), real permittivity (ϵ_1), normal reflectance (R) and absorption coefficient (α) are presented in panels (a)-(d), respectively. In each graph, subpanels (i) and (ii) report optical properties of NC with incident light polarized along the z- and x-axes of the NP, respectively. Subpanel (iii) presents the respective optical property of the NP in vacuum, with incident fields along the z-axis (black line) and along x (dotted red line). For the present plot, the optical properties of pure NP do not depend on field direction, and the lines in subpanels (iii) are superimposed. In subpanels (i) and (ii), different lines correspond to different NC volume fractions, as follows: solid black – G/1250 (3.7%vol), dashed blue – G/836 (5.4%vol). Horizontal solid orange lines represent the pure amorphous PVDF polymer. Where the orange line is not visible, it coincides with the graph's abscissa.

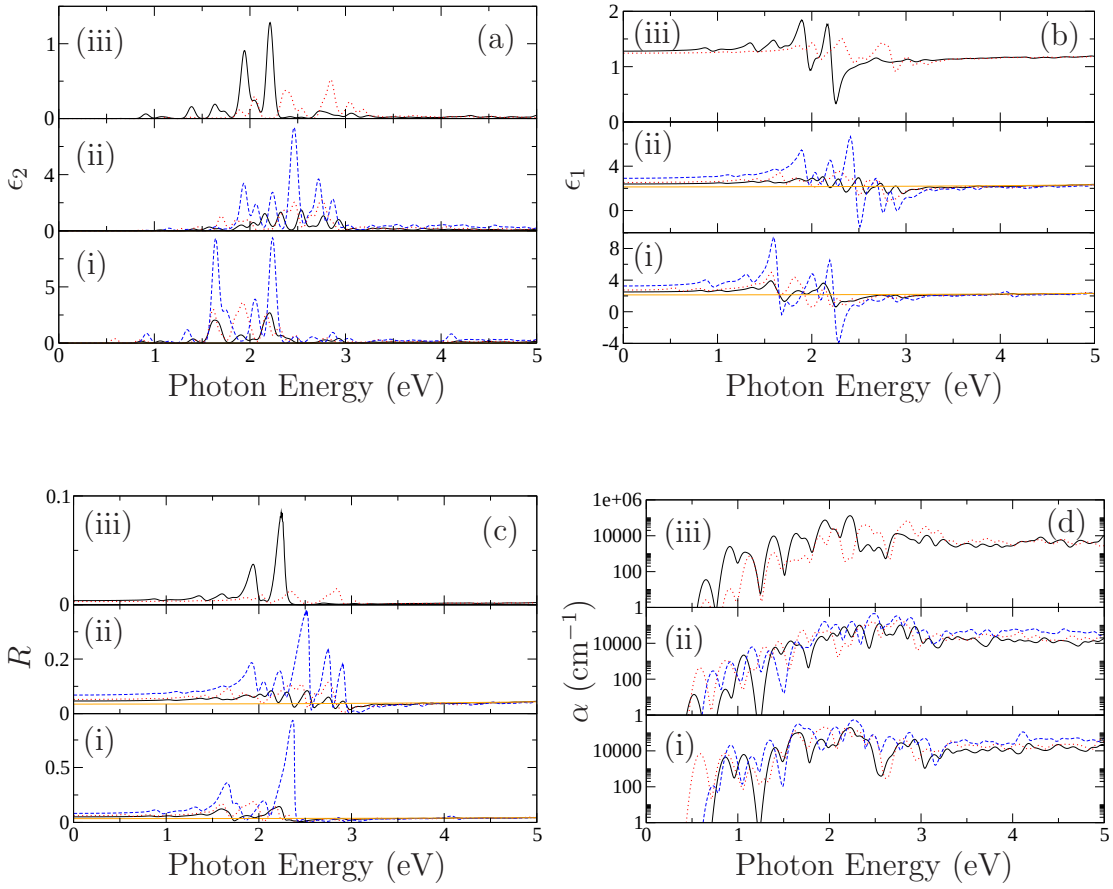

Figure B.7: Influence of NP volume fraction and incident field polarization on the optical properties of NP H and corresponding NC materials. Imaginary permittivity (ϵ_2), real permittivity (ϵ_1), normal reflectance (R) and absorption coefficient (α) are presented in panels (a)-(d), respectively. In each graph, subpanels (i) and (ii) report optical properties of NC with incident light polarized along the z- and x-axes of the NP, respectively. Subpanel (iii) presents the respective optical property of the NP in vacuum, with incident fields along the z-axis (black line) and along x (dotted red line). In subpanels (i) and (ii), different lines correspond to different NC volume fractions, as follows: solid black – H/1250 (1.6%vol), dotted red – H/836 (2.4%vol), dashed blue – H/416 (4.7%vol). Horizontal solid orange lines represent the pure amorphous PVDF polymer. Where the orange line is not visible, it coincides with the graph's abscissa.

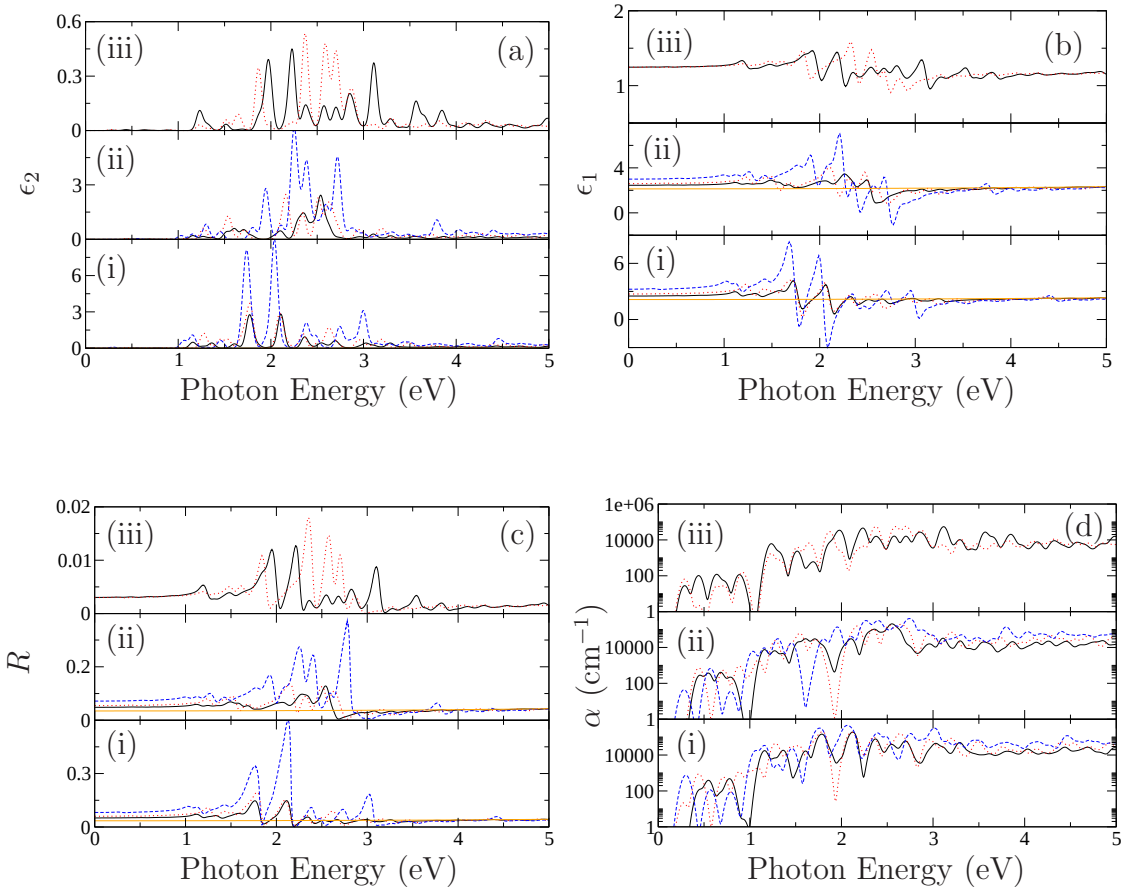

Figure B.8: Influence of NP volume fraction and incident field polarization on the optical properties of NP I and corresponding NC materials. Imaginary permittivity (ϵ_2), real permittivity (ϵ_1), normal reflectance (R) and absorption coefficient (α) are presented in panels (a)-(d), respectively. In each graph, subpanels (i) and (ii) report optical properties of NC with incident light polarized along the z- and x-axes of the NP, respectively. Subpanel (iii) presents the respective optical property of the NP in vacuum, with incident fields along the z-axis (black line) and along x (dotted red line). In subpanels (i) and (ii), different lines correspond to different NC volume fractions, as follows: solid black – I/1250 (1.7%vol), dotted red – I/836 (2.6%vol), dashed blue – I/416 (5.1%vol). Horizontal solid orange lines represent the pure amorphous PVDF polymer. Where the orange line is not visible, it coincides with the graph's abscissa.

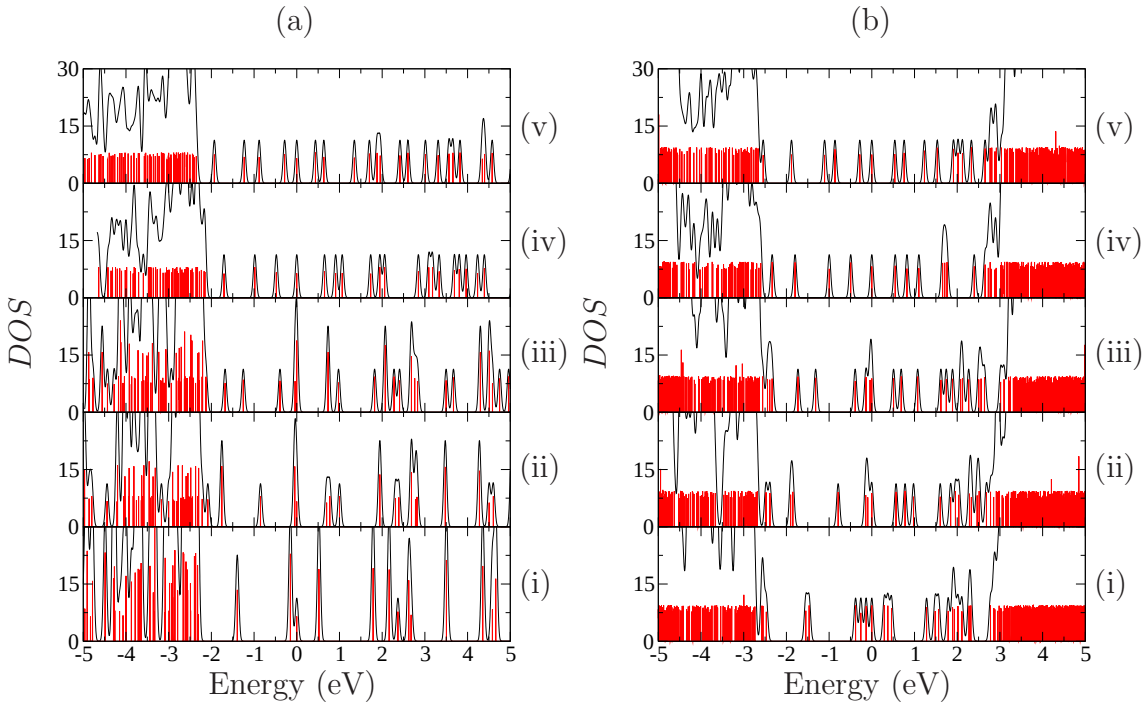

Figure B.9: Influence of NP shape on the density of states (DOS) of (a) NPs and (b) their NCs. Subpanels (i)–(v) present spectra from NPs B, C, D, H and I, respectively, and their NCs with 4.2%vol loading (B/740, C/590, D/668, H/470, and I/512). The zero on the Energy axis is set at the Fermi energy of that particular material. Black lines show a Gaussian energy broadening of 0.05eV, and the red lines illustrate the location of states with a finer broadening of 0.001eV.

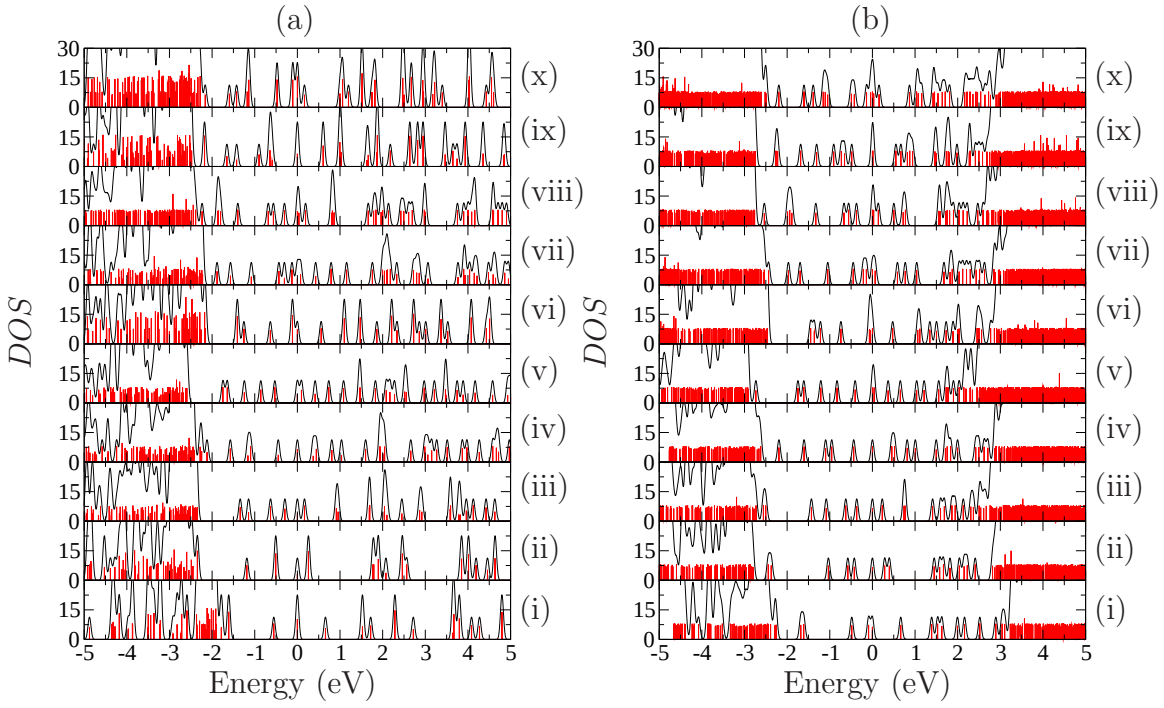

Figure B.10: Influence of {111} basal plane nanodisk aspect ratio on the density of states of (a) NPs and (b) their NCs with 4.2%vol loading. Subpanels (i)–(x) present spectra from NPs J, K, E, L–R, respectively, and their NCs. The zero on the Energy axis is set at the Fermi energy of that particular material. Black lines show a Gaussian energy broadening of 0.05eV, and the red lines illustrate the location of states with a finer broadening of 0.001eV.

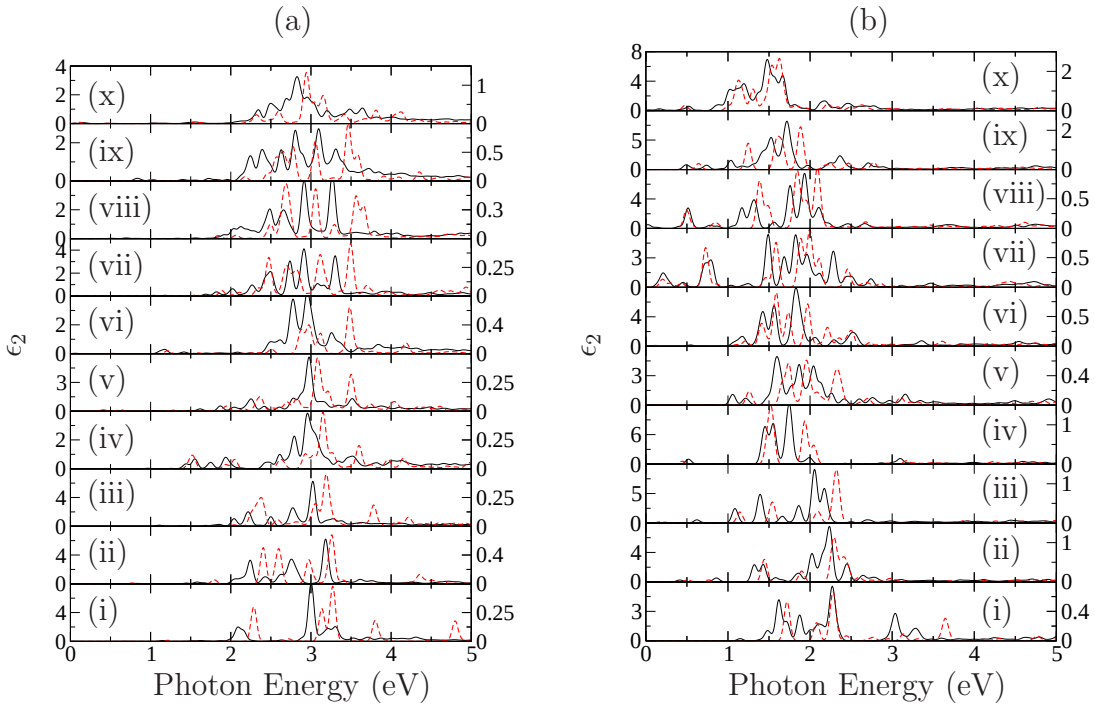

Figure B.11: Influence of {111} basal plane nanodisk aspect ratio on the imaginary dielectric constant (ϵ_2) of (a) NPs and (b) their NCs. Subpanels (i)–(x) present spectra from NPs J, K, E, L–R, respectively, and their NCs at 4.2%vol. Solid black is from NC and dashed red is from NP in vacuum, with ordinate scales along left and right sides, respectively.

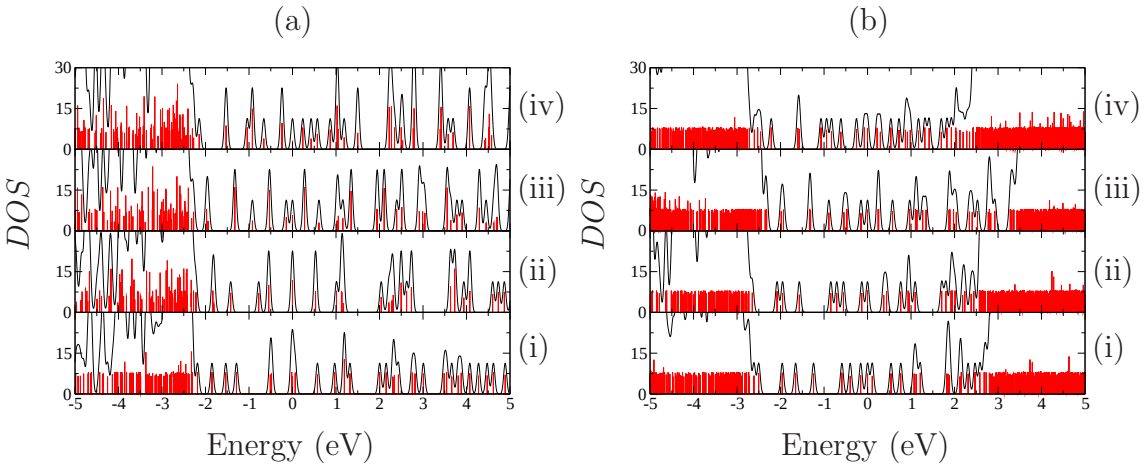

Figure B.12: Influence of {100} basal plane nanodisk aspect ratio on the density of states (DOS) of (a) NPs and (b) their NCs. Subpanels (i)–(iv) present spectra from NPs S–V, respectively, and their NCs. The zero on the Energy axis is set at the Fermi energy of that particular material. Black lines show a Gaussian energy broadening of 0.05eV, and the red lines illustrate the location of states with a finer broadening of 0.001eV.

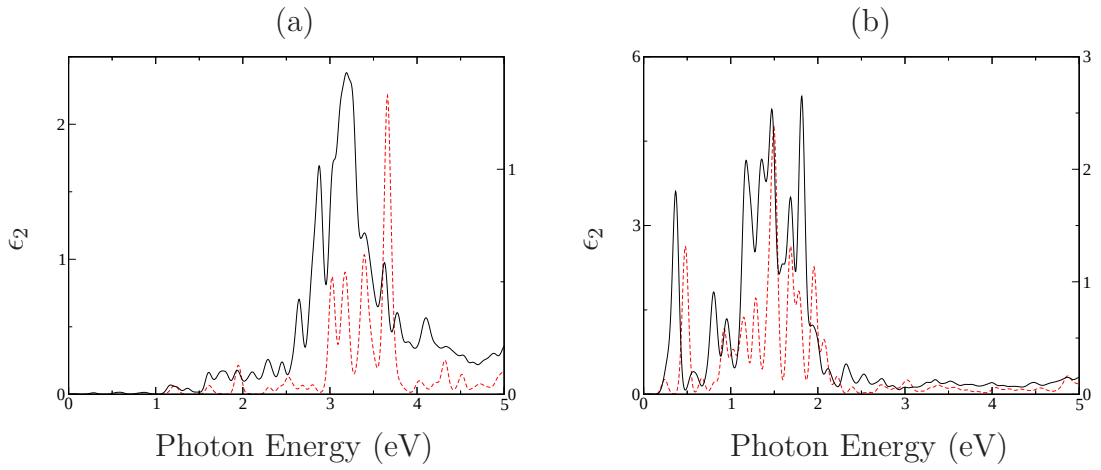

Figure B.13: Imaginary dielectric constant of {100} basal plane disk (NP V) and NC (V/1130). Panels (a) and (b) show polarization along z- and x-axes, respectively. Solid black is from NC and dashed red is from NP in vacuum, with ordinate scales along left and right sides, respectively.

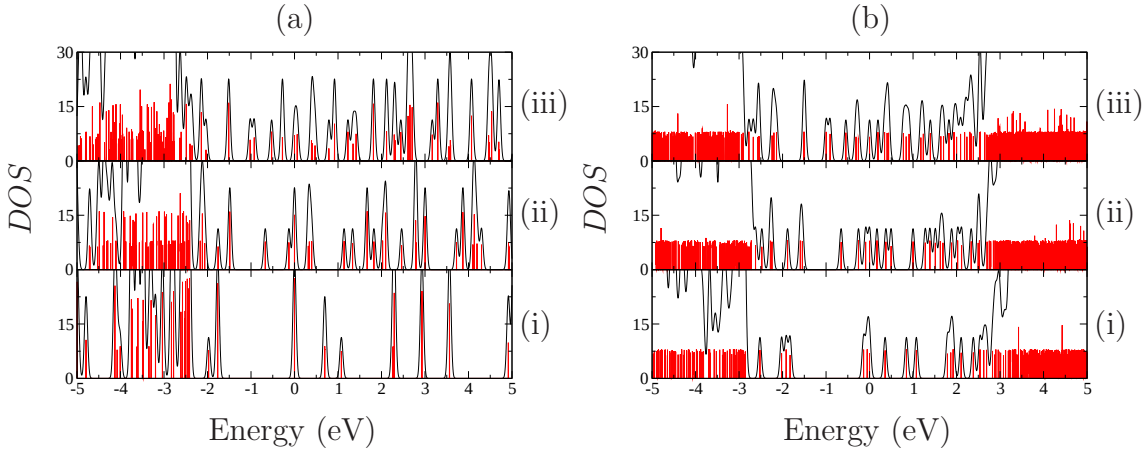

Figure B.14: Influence of nanorod aspect ratio on the density of states (DOS) of (a) NPs and (b) their NCs. Subpanels (i)–(iii) present spectra from NPs A, F and W, respectively, and their nanocomposites. The zero on the Energy axis is set at the Fermi energy of that particular material. Black lines show a Gaussian energy broadening of 0.05eV, and the red lines illustrate the location of states with a finer broadening of 0.001eV.

Appendix C

Simulation Cells and NPs

In what follows, data tables are provided with information about simulation cells and NPs. Table C.1 lists all NC systems that were designed and studied: providing the NP and number of polymer atoms, the calculated volume fraction, dimensions of the simulation cells and distances between inclusions across PBC images. Tables C.2–C.27 give the nuclear Cartesian coordinates of the NPs.

Table C.1: NC interparticle distances across PBC images and simulation cell lattice constants (Å). Inclusion sizes have an additional Lennard-Jones diameter of 2.889 Å added to the largest internuclear distances. For polydisperse AC/1094, interparticle separation is given along [111]

	Particle Separation			Cell Dimensions		
NC System	X	Y	Z	X	Y	Z
A/1250 (1.7%vol)	13.674	15.596	16.470	22.344	24.266	23.450
A/740 (2.9%vol)	8.712	11.632	14.594	17.382	20.302	21.574
A/536 (4.0%vol)	6.993	9.625	12.460	15.663	18.295	19.440
A/512 (4.2%vol)	6.766	9.360	12.179	15.436	18.030	19.159
A/416 (5.1%vol)	6.479	7.920	10.405	15.149	16.590	17.385
B/1250 (2.5%vol)	13.740	15.658	12.449	22.410	24.338	23.519
B/836 (3.7%vol)	9.486	12.526	11.465	18.156	21.206	22.535
B/740 (4.2%vol)	8.789	11.710	10.598	17.459	20.390	21.668
B/644 (4.8%vol)	8.034	10.828	9.661	16.704	19.508	20.731
B/536 (5.7%vol)	7.091	9.725	8.490	15.761	18.405	19.560
C/1250 (2.0%vol)	13.698	15.622	12.405	22.368	24.292	23.475
C/836 (3.0%vol)	9.462	12.482	11.374	18.132	21.152	22.444

Table C.1: *continued...*

	Particle Separation			Cell Dimensions		
NC System	X	Y	Z	X	Y	Z
C/644 (3.8%vol)	7.976	10.772	9.589	16.646	19.442	20.659
C/590 (4.2%vol)	7.512	10.230	9.014	16.182	18.900	20.084
C/536 (4.6%vol)	7.025	9.663	8.410	15.695	18.333	19.480
C/416 (5.8%vol)	6.518	7.963	6.360	15.188	16.633	17.430
D/1250 (2.3%vol)	13.717	15.653	16.525	22.387	24.313	23.495
D/836 (3.4%vol)	9.463	12.519	15.536	18.133	21.179	22.506
D/668 (4.2%vol)	8.201	11.044	13.969	16.871	19.704	20.939
D/644 (4.3%vol)	8.004	10.813	13.724	16.674	19.473	20.694
D/536 (5.1%vol)	7.057	9.706	12.548	15.727	18.366	19.518
D/416 (6.5%vol)	5.855	8.303	11.056	14.525	16.963	18.026
E/1250 (2.0%vol)	13.657	15.518	18.181	22.327	24.248	23.431
E/836 (3.0%vol)	9.437	12.419	17.225	18.107	21.149	22.475
E/590 (4.2%vol)	7.514	10.173	14.838	16.184	18.903	20.088
F/1250 (2.9%vol)	13.761	15.691	12.481	22.431	24.361	23.541
F/860 (4.2%vol)	11.223	12.935	9.818	19.893	21.605	20.878
F/836 (4.3%vol)	9.522	12.578	11.520	18.192	21.248	22.580
F/416 (8.3%vol)	5.945	8.398	7.077	14.615	17.068	18.137
G/1250 (3.7%vol)	22.499	24.435	23.613	13.479	15.415	14.593
G/1094 (4.2%vol)	12.531	14.385	13.598	21.551	23.405	22.618
G/836 (5.4%vol)	18.263	21.330	22.667	9.243	12.310	13.647
H/1250 (1.6%vol)	14.870	16.982	13.610	22.340	24.262	23.445
H/836 (2.4%vol)	10.602	13.828	12.596	18.072	21.108	22.431
H/470 (4.2%vol)	7.531	10.241	8.784	15.001	17.521	18.619
H/416 (4.7%vol)	6.958	9.570	8.071	14.428	16.850	17.906
I/1250 (1.7%vol)	14.139	16.012	14.245	22.349	24.272	23.455
I/836 (2.6%vol)	9.875	12.863	13.236	18.085	21.123	22.446
I/512 (4.2%vol)	7.226	9.769	9.949	15.436	18.029	19.159
I/416 (5.1%vol)	6.235	8.611	8.717	14.445	16.871	17.927
J/470 (4.2%vol)	6.332	7.952	13.370	15.002	17.521	18.620
K/512 (4.2%vol)	6.780	9.293	13.875	15.450	18.023	19.125
L/626 (4.2%vol)	5.280	10.614	15.243	16.510	19.284	20.493
M/668 (4.2%vol)	8.153	8.157	15.692	16.873	19.707	20.942
N/740 (4.2%vol)	8.830	7.069	16.418	20.390	17.459	21.668

Table C.1: *continued...*

	Particle Separation			Cell Dimensions		
NC System	X	Y	Z	X	Y	Z
O/782 (4.2%vol)	6.734	12.232	16.874	17.784	20.772	22.074
P/860 (4.2%vol)	8.662	10.053	15.626	19.892	21.603	20.876
Q/938 (4.2%vol)	9.980	11.451	16.445	20.474	22.236	21.487
R/1214 (4.2%vol)	7.865	11.345	18.169	22.315	24.235	23.419
S/740 (4.2%vol)	6.399	9.330	16.738	17.459	20.390	21.668
T/818 (4.2%vol)	7.024	10.067	17.489	18.054	21.087	22.409
U/980 (4.2%vol)	6.547	8.337	17.035	20.784	22.574	21.813
V/1130 (4.2%vol)	6.614	8.515	17.938	21.791	23.665	22.868
W/1214 (4.2%v)	13.652	15.572	8.276	22.322	24.242	23.426
X/1052 (4.2%vol)	12.604	13.533	5.286	21.274	23.103	22.326
Y/980 (4.2%vol)	12.105	12.992	9.473	20.775	22.562	21.803
Z/1214 (4.2%vol)	13.647	14.666	11.091	22.317	24.236	23.421
AC/1094 (4.2%vol)		11.410		21.555	23.410	22.623

Table C.2: Coordinates of NP A, Ag_{13} (Å)

X	Y	Z
0.000	0.000	0.000
2.889	0.000	0.000
-2.889	0.000	0.000
0.000	2.889	0.000
0.000	-2.889	0.000
1.445	1.445	2.043
1.445	-1.445	2.043
-1.445	1.445	2.043
-1.445	-1.445	2.043
1.445	1.445	-2.043
-1.445	1.445	-2.043
1.445	-1.445	-2.043
-1.445	-1.445	-2.043

Table C.3: Coordinates of NP B, Ag_{19} (Å)

X	Y	Z
0.000	0.000	0.000
2.889	0.000	0.000
-2.889	0.000	0.000
0.000	2.889	0.000
0.000	-2.889	0.000
1.445	1.445	2.043
1.445	-1.445	2.043
-1.445	1.445	2.043
-1.445	-1.445	2.043
1.445	1.445	-2.043
-1.445	1.445	-2.043
1.445	-1.445	-2.043
-1.445	-1.445	-2.043
2.889	2.889	0.000
-2.889	-2.889	0.000
-2.889	2.889	0.000
2.889	-2.889	0.000
0.000	0.000	-4.086
0.000	0.000	4.086

Table C.4: Coordinates of NP C, Ag_{15} (Å)

X	Y	Z
0.000	0.000	0.000
2.889	0.000	0.000
-2.889	0.000	0.000
0.000	2.889	0.000
0.000	-2.889	0.000
1.445	1.445	2.043
1.445	-1.445	2.043
-1.445	-1.445	2.043
-1.445	1.445	2.043
1.445	1.445	-2.043
1.445	-1.445	-2.043
-1.445	1.445	-2.043
-1.445	-1.445	-2.043
0.000	0.000	4.086
0.000	0.000	-4.086

Table C.5: Coordinates of NP D, Ag_{17} (Å)

X	Y	Z
0.000	0.000	0.000
2.889	0.000	0.000
-2.889	0.000	0.000
0.000	2.889	0.000
0.000	-2.889	0.000
1.445	1.445	2.043
1.445	-1.445	2.043
-1.445	1.445	2.043
-1.445	-1.445	2.043
1.445	1.445	-2.043
-1.445	1.445	-2.043
1.445	-1.445	-2.043
-1.445	-1.445	-2.043
2.889	2.889	0.000
-2.889	-2.889	0.000
-2.889	2.889	0.000
2.889	-2.889	0.000

Table C.6: Coordinates of NP E, Ag_{15} disk (111) (Å)

X	Y	Z
0.000	0.000	0.000
2.889	0.000	0.000
1.445	2.502	0.000
-1.445	2.502	0.000
-2.889	0.000	0.000
-1.445	-2.502	0.000
1.445	-2.502	0.000
2.889	1.668	2.359
0.000	1.668	2.359
-2.889	1.668	2.359
-1.445	-0.834	2.359
-2.889	-3.336	2.359
0.000	-3.336	2.359
2.889	-3.336	2.359
1.445	-0.834	2.359

Table C.7: Coordinates of NP F, Ag_{22} rod (100) (Å)

X	Y	Z
0.000	0.000	0.000
2.889	0.000	0.000
-2.889	0.000	0.000
0.000	2.889	0.000
0.000	-2.889	0.000
1.445	1.445	2.043
1.445	-1.445	2.043
-1.445	1.445	2.043
-1.445	-1.445	2.043
1.445	1.445	-2.043
-1.445	1.445	-2.043
1.445	-1.445	-2.043
-1.445	-1.445	-2.043
2.889	0.000	4.086
-2.889	0.000	4.086
0.000	2.889	4.086
0.000	-2.889	4.086
0.000	0.000	4.086
1.445	1.445	6.129
1.445	-1.445	6.129
-1.445	1.445	6.129
-1.445	-1.445	6.129

Table C.8: Coordinates of NP G, Ag_{28} sphere (Å)

X	Y	Z
2.043	0.000	0.000
0.000	2.043	0.000
2.043	4.086	0.000
6.129	4.086	0.000
4.086	2.043	0.000
4.086	6.129	0.000
0.000	0.000	2.043
4.086	0.000	2.043
4.086	0.000	6.129
2.043	0.000	4.086
6.129	0.000	4.086
0.000	4.086	2.043
0.000	4.086	6.129
0.000	2.043	4.086
0.000	6.129	4.086
2.043	2.043	2.043
2.043	2.043	6.129
2.043	6.129	2.043
2.043	6.129	6.129
6.129	2.043	2.043
6.129	2.043	6.129
6.129	6.129	2.043
4.086	4.086	2.043
4.086	4.086	6.129
2.043	4.086	4.086
6.129	4.086	4.086
4.086	2.043	4.086
4.086	6.129	4.086

Table C.9: Coordinates of NP H, amorphous Ag_{12} (Å)

X	Y	Z
1.256	-0.096	3.559
-0.346	-1.570	1.894
-1.542	0.075	3.847
-0.235	1.427	1.703
-0.377	0.979	-3.098
1.865	-0.393	-2.052
-1.851	1.772	-0.840
1.987	-0.073	0.844
1.249	-2.493	-0.217
-0.619	-0.587	-0.747
-2.593	0.081	1.297
0.957	1.897	-0.817

Table C.10: Coordinates of NP I, amorphous Ag_{13} (Å)

X	Y	Z
1.249	-0.552	2.646
-0.209	-2.905	2.376
-1.557	-0.377	2.800
-0.069	1.247	0.942
-0.822	-0.218	-1.515
1.864	-0.368	-2.226
-1.399	2.469	-1.362
2.602	0.393	0.373
0.931	-1.782	0.087
-1.855	-1.884	0.496
-2.724	0.711	0.495
1.399	2.230	-1.230
0.208	1.425	-3.521

Table C.11: Coordinates of NP J, Ag_{12} disk (111) (Å)

X	Y	Z
0.000	1.668	2.359
0.000	-3.336	2.359
1.445	-0.834	2.359
-1.445	-0.834	2.359
2.889	1.668	2.359
-2.889	1.668	2.359
1.445	0.834	4.718
-1.445	0.834	4.718
0.000	-1.668	4.718
0.000	3.336	4.718
-2.889	-1.668	4.718
2.889	-1.668	4.718

Table C.12: Coordinates of NP K, Ag_{13} disk (111) (Å)

X	Y	Z
0.000	0.000	0.000
2.889	0.000	0.000
-2.889	0.000	0.000
1.445	2.502	0.000
1.445	-2.502	0.000
-1.445	2.502	0.000
-1.445	-2.502	0.000
0.000	1.668	2.359
0.000	-3.336	2.359
1.445	-0.834	2.359
-1.445	-0.834	2.359
2.889	1.668	2.359
-2.889	1.668	2.359

Table C.13: Coordinates of NP L, Ag_{16} disk (111) (Å)

X	Y	Z
0.000	0.000	0.000
2.502	1.445	0.000
0.000	2.889	0.000
-2.502	1.445	0.000
-5.004	0.000	0.000
-2.502	-1.445	0.000
0.000	-2.889	0.000
2.502	-1.445	0.000
1.668	0.000	2.359
-0.834	1.445	2.359
-3.336	2.889	2.359
-5.838	1.445	2.359
-3.336	0.000	2.359
-5.838	-1.445	2.359
-3.336	-2.889	2.359
-0.834	-1.445	2.359

Table C.14: Coordinates of NP M, Ag_{17} disk (111) (Å)

X	Y	Z
0.000	0.000	0.000
0.000	2.889	0.000
-2.502	1.445	0.000
-2.502	4.334	0.000
-5.004	2.889	0.000
-5.004	0.000	0.000
-2.502	-1.445	0.000
-5.004	-2.889	0.000
-2.502	-4.334	0.000
0.000	-2.889	0.000
0.834	1.445	2.359
-1.668	2.889	2.359
-4.170	1.445	2.359
-1.668	0.000	2.359
-4.170	-1.445	2.359
-1.668	-2.889	2.359
0.834	-1.445	2.359

Table C.15: Coordinates of NP N, Ag_{19} disk (111) (Å)

X	Y	Z
0.000	0.000	0.000
1.445	2.502	0.000
2.889	0.000	0.000
1.445	-2.502	0.000
4.334	-2.502	0.000
2.889	-5.004	0.000
0.000	-5.004	0.000
-1.445	-2.502	0.000
-2.889	-5.004	0.000
-4.334	-2.502	0.000
-2.889	0.000	0.000
-1.445	2.502	0.000
1.445	0.834	2.359
2.889	-1.668	2.359
1.445	-4.170	2.359
0.000	-1.668	2.359
-1.445	-4.170	2.359
-2.889	-1.668	2.359
-1.445	0.834	2.359

Table C.16: Coordinates of NP O, Ag_{20} disk (111) (Å)

X	Y	Z
0.000	0.000	0.000
2.502	1.445	0.000
0.000	2.889	0.000
-2.502	1.445	0.000
-5.004	2.889	0.000
-5.004	0.000	0.000
-2.502	-1.445	0.000
-5.004	-2.889	0.000
0.000	-2.889	0.000
2.502	-1.445	0.000
1.668	0.000	2.359
1.668	2.889	2.359
-0.834	1.445	2.359
-3.336	2.889	2.359
-5.838	1.445	2.359
-3.336	0.000	2.359
-5.838	-1.445	2.359
-3.336	-2.889	2.359
-0.834	-1.445	2.359
1.668	-2.889	2.359

Table C.17: Coordinates of NP P, Ag_{22} disk (111) (Å)

X	Y	Z
0.000	0.000	0.000
2.502	1.445	0.000
0.000	2.889	0.000
-2.502	1.445	0.000
-2.502	4.334	0.000
-5.004	2.889	0.000
-5.004	0.000	0.000
-2.502	-1.445	0.000
-5.004	-2.889	0.000
-2.502	-4.334	0.000
0.000	-2.889	0.000
2.502	-1.445	0.000
0.834	1.445	2.359
-1.668	2.889	2.359
-4.170	1.445	2.359
-1.668	0.000	2.359
-4.170	-1.445	2.359
-1.668	-2.889	2.359
0.834	-1.445	2.359
3.336	0.000	2.359
-4.170	3.723	2.359
-4.170	-3.723	2.359

Table C.18: Coordinates of NP Q, Ag_{24} disk (111) (Å)

X	Y	Z
0.000	0.000	0.000
2.502	1.445	0.000
0.000	2.889	0.000
-2.502	1.445	0.000
-2.502	4.334	0.000
-5.004	2.889	0.000
-5.004	0.000	0.000
-2.502	-1.445	0.000
-5.004	-2.889	0.000
-2.502	-4.334	0.000
0.000	-2.889	0.000
2.502	-1.445	0.000
1.668	0.000	2.359
1.668	2.889	2.359
-0.834	1.445	2.359
-0.834	4.334	2.359
-3.336	2.889	2.359
-5.838	1.445	2.359
-3.336	0.000	2.359
-5.838	-1.445	2.359
-3.336	-2.889	2.359
-0.834	-1.445	2.359
-0.834	-4.334	2.359
1.668	-2.889	2.359

Table C.19: Coordinates of NP R, Ag_{31} disk (111) (Å)

X	Y	Z
0.000	0.000	0.000
2.889	0.000	0.000
1.445	2.502	0.000
-1.445	2.502	0.000
-2.889	0.000	0.000
-1.445	-2.502	0.000
1.445	-2.502	0.000
5.778	0.000	0.000
4.334	2.502	0.000
2.889	5.004	0.000
0.000	5.004	0.000
-2.889	5.004	0.000
-4.334	2.502	0.000
-5.778	0.000	0.000
-4.334	-2.502	0.000
-2.889	-5.004	0.000
0.000	-5.004	0.000
2.889	-5.004	0.000
4.334	-2.502	0.000
2.889	1.668	2.359
0.000	1.668	2.359
-2.889	1.668	2.359
-1.445	-0.834	2.359
-2.889	-3.336	2.359
0.000	-3.336	2.359
2.889	-3.336	2.359
1.445	-0.834	2.359
1.445	4.170	2.359
-1.445	4.170	2.359
4.334	-0.834	2.359
-4.334	-0.834	2.359

Table C.20: Coordinates of NP S, Ag_{19} disk (100) (Å)

X	Y	Z
0.000	0.000	0.000
4.086	0.000	0.000
2.043	2.043	0.000
-2.043	2.043	0.000
-4.086	0.000	0.000
-2.043	-2.043	0.000
2.043	-2.043	0.000
2.043	0.000	2.043
4.086	2.043	2.043
2.043	4.086	2.043
0.000	2.043	2.043
-2.043	4.086	2.043
-4.086	2.043	2.043
-2.043	0.000	2.043
-4.086	-2.043	2.043
-2.043	-4.086	2.043
0.000	-2.043	2.043
2.043	-4.086	2.043
4.086	-2.043	2.043

Table C.21: Coordinates of NP T, Ag_{21} disk (100) (Å)

X	Y	Z
0.000	0.000	0.000
4.086	0.000	0.000
2.043	2.043	0.000
-2.043	2.043	0.000
-4.086	0.000	0.000
-2.043	-2.043	0.000
2.043	-2.043	0.000
0.000	4.086	0.000
0.000	-4.086	0.000
2.043	0.000	2.043
4.086	2.043	2.043
2.043	4.086	2.043
0.000	2.043	2.043
-2.043	4.086	2.043
-4.086	2.043	2.043
-2.043	0.000	2.043
-4.086	-2.043	2.043
-2.043	-4.086	2.043
0.000	-2.043	2.043
2.043	-4.086	2.043
4.086	-2.043	2.043

Table C.22: Coordinates of NP U, Ag_{25} disk (100) (Å)

X	Y	Z
0.000	0.000	0.000
4.086	0.000	0.000
2.043	2.043	0.000
-2.043	2.043	0.000
-4.086	0.000	0.000
-2.043	-2.043	0.000
2.043	-2.043	0.000
0.000	4.086	0.000
0.000	-4.086	0.000
2.043	0.000	2.043
-2.043	0.000	2.043
0.000	2.043	2.043
0.000	-2.043	2.043
6.129	0.000	2.043
-6.129	0.000	2.043
0.000	6.129	2.043
0.000	-6.129	2.043
4.086	2.043	2.043
2.043	4.086	2.043
-4.086	-2.043	2.043
-2.043	-4.086	2.043
-2.043	4.086	2.043
-4.086	2.043	2.043
4.086	-2.043	2.043
2.043	-4.086	2.043

Table C.23: Coordinates of NP V, Ag_{29} disk (100) (Å)

X	Y	Z
0.000	0.000	0.000
4.086	0.000	0.000
2.043	2.043	0.000
-2.043	2.043	0.000
-4.086	0.000	0.000
-2.043	-2.043	0.000
2.043	-2.043	0.000
0.000	4.086	0.000
0.000	-4.086	0.000
4.086	4.086	0.000
4.086	-4.086	0.000
-4.086	-4.086	0.000
-4.086	4.086	0.000
2.043	0.000	2.043
-2.043	0.000	2.043
0.000	2.043	2.043
0.000	-2.043	2.043
6.129	0.000	2.043
-6.129	0.000	2.043
0.000	6.129	2.043
0.000	-6.129	2.043
4.086	2.043	2.043
2.043	4.086	2.043
-4.086	-2.043	2.043
-2.043	-4.086	2.043
-2.043	4.086	2.043
-4.086	2.043	2.043
4.086	-2.043	2.043
2.043	-4.086	2.043

Table C.24: Coordinates of NP W, Ag_{31} rod (100) (Å)

X	Y	Z
2.043	0.000	0 .000
0.000	2.043	0 .000
-2.043	0.000	0 .000
0.000	-2.043	0 .000
2.043	2.043	2 .043
2.043	-2.043	2 .043
-2.043	2.043	2 .043
-2.043	-2.043	2 .043
0.000	0.000	2 .043
2.043	0.000	4 .086
0.000	2.043	4 .086
0.000	-2.043	4 .086
-2.043	0.000	4 .086
2.043	2.043	6 .129
-2.043	-2.043	6 .129
-2.043	2.043	6 .129
2.043	-2.043	6 .129
0.000	0.000	6 .129
2.043	0.000	8 .172
0.000	2.043	8 .172
-2.043	0.000	8 .172
0.000	-2.043	8 .172
2.043	2.043	10.215
-2.043	-2.043	10.215
2.043	-2.043	10.215
-2.043	2.043	10.215
0.000	0.000	10.215
2.043	0.000	12.258
0.000	2.043	12.258
-2.043	0.000	12.258
0.000	-2.043	12.258

Table C.25: Coordinates of NP X, Ag_{27} rod (111) (Å)

X	Y	Z
0.000	0.000	0.000
2.889	0.000	0.000
-2.889	0.000	0.000
1.445	2.502	0.000
1.445	-2.502	0.000
-1.445	2.502	0.000
-1.445	-2.502	0.000
0.000	1.668	2.359
0.000	-3.336	2.359
1.445	-0.834	2.359
-1.445	-0.834	2.359
2.889	1.668	2.359
-2.889	1.668	2.359
1.445	0.834	-2.359
-1.445	0.834	-2.359
0.000	-1.668	-2.359
0.000	3.336	-2.359
-2.889	-1.668	-2.359
2.889	-1.668	-2.359
0.000	1.668	-4.718
1.445	-0.834	-4.718
-1.445	-0.834	-4.718
1.445	0.834	4.718
-1.445	0.834	4.718
0.000	-1.668	4.718
0.000	0.000	-7.077
0.000	0.000	7.077

Table C.26: Coordinates of NP Y, Ag_{25} rod (111) (Å)

X	Y	Z
0.000	0.000	0.000
2.889	0.000	0.000
-2.889	0.000	0.000
1.445	2.502	0.000
1.445	-2.502	0.000
-1.445	2.502	0.000
-1.445	-2.502	0.000
0.000	1.668	2.359
0.000	-3.336	2.359
1.445	-0.834	2.359
-1.445	-0.834	2.359
2.889	1.668	2.359
-2.889	1.668	2.359
1.445	0.834	-2.359
-1.445	0.834	-2.359
0.000	-1.668	-2.359
0.000	3.336	-2.359
-2.889	-1.668	-2.359
2.889	-1.668	-2.359
0.000	1.668	-4.718
1.445	-0.834	-4.718
-1.445	-0.834	-4.718
1.445	0.834	4.718
-1.445	0.834	4.718
0.000	-1.668	4.718

Table C.27: Coordinates of NP Z, Ag_{31} rod (111) (Å)

X	Y	Z
0.000	0.000	0.000
2.889	0.000	0.000
-2.889	0.000	0.000
1.445	2.502	0.000
1.445	-2.502	0.000
-1.445	2.502	0.000
-1.445	-2.502	0.000
0.000	1.668	2.359
0.000	-3.336	2.359
1.445	-0.834	2.359
-1.445	-0.834	2.359
2.889	1.668	2.359
-2.889	1.668	2.359
1.445	0.834	4.718
-1.445	0.834	4.718
0.000	-1.668	4.718
0.000	3.336	4.718
-2.889	-1.668	4.718
2.889	-1.668	4.718
1.445	0.834	-2.359
-1.445	0.834	-2.359
0.000	-1.668	-2.359
0.000	3.336	-2.359
-2.889	-1.668	-2.359
2.889	-1.668	-2.359
0.000	1.668	-4.718
0.000	-3.336	-4.718
1.445	-0.834	-4.718
-1.445	-0.834	-4.718
2.889	1.668	-4.718
-2.889	1.668	-4.718